Technical note: Surface fields for global environmental modelling

Margarita Choulga[1], Francesca Moschini[1], Cinzia Mazzetti[1], Stefania Grimaldi[2], Juliana Disperati[3], Hylke Beck[4], Peter Salamon[2], Christel Prudhomme[1]

[1]European Centre for Medium-Range Weather Forecasts (ECMWF), Reading, RG2 9AX, United Kingdom
[2]Joint Research Centre (JRC), European Commission, Ispra, 21027, Italy
[3]Fincons Group, Vimercate, 20871, Italy
[4]King Abdullah University of Science and Technology (KAUST), Thuwal, Saudi Arabia

Correspondence to: Margarita Choulga (margarita.choulga@ecmwf.int) and Christel Prudhomme (christel.prudhomme@ecmwf.int)

Abstract. Climate change has resulted in more frequent occurrences of extreme events, such as flooding and heavy snowfall, which can have a significant impact on densely populated or industrialised areas. Numerical models are used to simulate and predict these extreme events, enabling informed decision-making and planning to minimise human casualties and to protect costly infrastructure. LISFLOOD is an integrated hydrological model underpinning the European and Global Flood Awareness Systems (EFAS and GloFAS, respectively) developed by the Copernicus Emergency Management Service (CEMS). The CEMS_SurfaceFields_2022 dataset is a new set of high-resolution surface fields at 1 and 3 ~~arc min~~ arcminute resolution (approximately 2 and 6 km at the equator respectively) ~~covering Europe and the global land surface (excluding Antarctica) respectively,~~ based on a wide variety of high-resolution and up-to-date data sources. The 1 arcminute fields cover Europe while the surface fields at 3 arcminute cover the global land surface (excluding Antarctica). The dataset encompasses (i) catchment morphology and river ~~network~~networks, (ii) land use, (iii) vegetation cover type and properties, (iv) soil properties, (v) lake information, and (vi) water demand. This manuscript details the complete workflow used to generate the CEMS_SurfaceFields_2022 fields, including the data sources and methodology. Whilst created together with upgrades to the open source LISFLOOD code, the CEMS_ SurfaceFields_2022 fields can be used independently for a wide range of applications, including as input ~~of~~to hydrological, Earth System or environmental ~~modelling~~models, or for carrying out general analyses across spatial scales, ranging from global and regional to local levels (especially useful for regions outside Europe), expected to improve accuracy, detail, and realism of applications.

1 Introduction

Current numerical Earth system models are highly complex. Thanks to the availability of High Performance Computers, cloud computing, and a wide range of high-resolution environmental data derived from the use of ground, unconventional and satellite measurement sensors, numerical global models are even able to reach kilometre-scale horizontal resolution. But increase in spatial resolution also means that the Earth system and environmental models have to represent more surface and atmospheric processes and their interactions, which can become challenging, for example in complex orographic areas. Model accuracy heavily depends on the quality of the input surface fields (i.e. how realistic and up-to-date they are), and it is essential to minimise errors in surface fields. New high-resolution (i.e. 10-100 m) surface datasets based on daily satellite observations are now frequently released and continuously supported by e.g. the Copernicus program (e.g. Global Land Cover: Buchhorn et al., 2021; GHSL-BUILT-S: Pesaresi and Politis, 2022; Schiavina et al., 2022), which helps in achieving the goal of minimising surface field errors. It was shown, e.g. in Kimpson et al. (2023), that the use of accurate and up-to-date underlying information to generate model's input surface fields can substantially reduce skin temperature errors even at 30 km horizontal resolution (Kimpson et al., 2023).

Following the digital revolution of cloud archiving and computing, where data, software and information technology (IT) infrastructure can be accessed by anyone from everywhere, the Earth systems and environmental modelling community has also moved from codes developed by a single organisation and few contributors, to so-called 'community models'~~where a~~. Community model's reference code is open for free use and/ or development according to sharing principles. Such models include Joint UK Environmental Simulator JULES~~, a land surface model whose development is coordinated by the UK Met Office and UKCEH[1]~~ (Best et al., 2011; Clark et al., 2011; Marthews et al., 2022), OpenIFS~~, a Numerical Weather Forecast model available to external users for research and training[2]~~ (Sparrow et al., 2021; Carver, 2022; Huijnen et al., 2022; Köhler et al., 2023), the Community Land Model CLM~~, an Earth System Model with strong climate component maintained by the National~~

---

[1] JULES is a land surface model whose development is coordinated by the UK Met Office and UKCEH.
[2] OpenIFS is a Numerical Weather Forecast model available to external users for research and training.

51 ~~Centre for Atmospheric Research but available for use by the wider research community (Lawrence et al., 2019),~~
52 ~~or LISFLOOD-OS, a spatially distributed water resources model developed by the Joint Research Centre (JRC;~~
53 ~~Van Der Knijff and De Roo, 2008) and available for use and development through a share code repository~~
54 ~~(available online: https://ec-jrc.github.io/lisflood/#lisflood; https://ec-jrc.github.io/lisflood-code/, last accessed:~~
55 ~~21.01.2024~~[3] (Lawrence et al., 2019), and LISFLOOD-OS[4] (Van Der Knijff and De Roo, 2008).
56 To promote the seamless development of science, and facilitate research community efforts in working with the
57 same code and input data, providing feedback, and improving the code and the data itself, powerful web-based
58 platforms can be used. One of them is the Google Earth Engine (GEE; Gorelick et al., 2017), a free-of-charge
59 platform that provides easy, web-based access to an extensive catalogue of satellite imagery and other geospatial
60 data in an analysis-ready format. The data catalogue is embedded into Google computing platform that lets you
61 easily implement all personal workflows, which facilitates global-scale analysis and visualization (GEE: FAQ,
62 2023). GEE was chosen for the generation of a new vast surface field set due to its high resolution data catalogue
63 and powerful computation capabilities.
64 This manuscript presents the methodology used to prepare the CEMS_SurfaceFields_2022 dataset containing all
65 surface fields necessary to run the LISFLOOD-OS model at resolutions ~2 km at the equator or 1 ~~are min~~arcminute
66 (over Europe; 1 arcminute resolution at mid-latitude of the domain (47.50 N) is ~1.25 km) and ~6 km at the
67 equator or 3 ~~are min~~arcminute (globally). CEMS_SurfaceFields_2022 were used in the set-up of the Early
68 Warning Systems of the Copernicus Emergency Management Service of the European Union for the European
69 ~~(European Flood Awareness System EFAS version 5; Smith et al., 2016; information available online:~~
70 ~~https://www.efas.eu/, last accessed: 21.01.2024) and global (Global Flood Awareness System GloFAS version 4;~~
71 ~~Hirpa et al., 2018; Alfieri et al., 2020; Harrigan et al., 2023; information available online:~~
72 ~~https://www.globalfloods.eu/, last accessed: 21.01.2024)~~[5] and global[6] domains operational in December 2023
73 (EFASv5 and GloFASv4). Details on raw data collection, scientific protocol, and technical methods aim to allow
74 the adequate understanding and interpretation of the surface field datasets~~, and for~~. For any interested user it is
75 possible to generate their own datasets by replicating or adapting the workflow to different fields, geographical
76 domain, spatial resolution, or content as relevant for downstream application. The manuscript is structured as
77 follows: Section 2 provides an overview of the surface fields, explains the criteria to select reference data, where
78 and how they were processed, and outlines the general methodology to produce the surface fields; Section 3 to
79 Section 8 details the reference data and specific methodology applied to each surface ~~filed~~field category, including
80 examples of application; Section 9 provides all the relevant information for data access; Section 10 discusses the
81 challenges of creating a consistent high resolution continental and global scale set of ~~consistent~~ surface fields and
82 the opportunities disclosed by their availability.

83 **2 Surface fields for distributed environmental modelling**

84 **2.1 General information**

85 Environmental models, especially land surface and hydrological models, simulate how water moves across
86 canopy, surface, subsurface, ground and eventually river channels using mechanistic equations that describe the
87 physics of these processes. Each model represents processes with more or less complexity, depending on the
88 model purpose and expected output (Rosbjerg and Madsen, 2006). With most represented terrestrial processes
89 depending on the landscape, information describing the spatial variation in the geophysical and vegetation
90 characteristics is needed. Such characteristics include morphological features (e.g. channel geometry, orography
91 or slope), soil hydraulic property, land and vegetation features (e.g. ecosystem cover type, leaf area index (LAI),
92 evaporation rates, crop type, planting and harvesting dates), and if relevant, human intervention information such
93 as population density or type of water usage.
94 LISFLOOD is a semi-distributed, physically based hydrological model which has been designed for the modelling
95 of rainfall-runoff processes in large and transnational catchments (Bates and De Roo, 2000; De Roo et al., 2000;
96 De Roo et al., 2001; Van Der Knijff and De Roo, 2008; Van Der Knijff et al., 2010; Burek et al., 2013). In its
97 most prominent application, LISFLOOD is used by the Copernicus Emergency Management Services' EFAS and

---

[3] CLM is an Earth System Model with strong climate component maintained by the National Centre for Atmospheric Research but available for use by the wider research community.

[4] LISFLOOD-OS is a spatially distributed water resources model developed by the Joint Research Centre and available for use and development through a share code repository (available online: https://ec-jrc.github.io/lisflood/#lisflood; https://ec-jrc.github.io/lisflood-code/, last accessed: 21.01.2024).

[5] European Flood Awareness System EFAS version 5 (Smith et al., 2016; information available online: https://www.efas.eu/, last accessed: 21.01.2024).

[6] Global Flood Awareness System GloFAS version 4 (Hirpa et al., 2018; Alfieri et al., 2020; Harrigan et al., 2023; information available online: https://www.globalfloods.eu/, last accessed: 21.01.2024).

98 GloFAS to provide medium range and seasonal riverine flow forecasts (Alfieri et al., 2020). LISFLOOD is also
99 widely used for a variety of applications, including water resources assessment (drought forecast); analysis of the
100 impacts of land use changes, river regulation measures, water management plans; climate change analysis (e.g.
101 Vanham et al., 2021).
102 To facilitate users' uptake and enable the seamless development of science, LISFLOOD has been released as open
103 source in 2019, i.e. LISFLOOD-OS. The open-source suite includes the LISFLOOD hydrological model and a set
104 of auxiliary tools for model setup, calibration, and post-processing of the results. For instance, the pre-processor
105 LISFLOOD-LISVAP can be used to compute evapotranspiration, which ~~is one of the three meteorological~~
106 ~~variables, along~~together with total precipitation and average temperature, are the three meteorological variables
107 strictly required as input to the hydrological model.
108 The modelling of runoff processes in different climates and socio-economic contexts then requires a set of raster
109 fields (i.e. set of surface fields presented in this manuscript) to provide information of terrain morphology, surface
110 water bodies, soil properties, land cover and land use features, water demand. The total number of fields range
111 between 66, when only the essential rainfall-runoff processes are modelled, to a total 108 for a more
112 comprehensive model set-up in which, for instance, lakes, reservoirs, water demand for anthropogenic use are
113 included (available online: https://ec-jrc.github.io/lisflood-model/, last accessed: 21.01.2024).
114 The main model's field (i.e. in technical for model operation/ running sense) is a 'mask' – a Boolean field that
115 defines model boundaries, i.e. grid cells over which the model performs calculations and grid cells which are
116 skipped (e.g. ocean grid cells). Whilst the surface fields described in this manuscript follow specific requirements
117 of the LISFLOOD-OS model, ~~they are~~it is a source of versatile information that can be used for any environmental
118 modelling application, either directly, or following a transformation, as relevant, as a full set or as a few consistent
119 fields.

2.2 Reference data and methodology

121 To produce CEMS_SurfaceFields_2022 surface fields only open source, freely available, updated as recently as
122 possible, with recognised reference on their quality data sources were used (see Appendix 1 for all relevant
123 reference data details). Note that whilst the majority of surface fields contain no time element, vegetation and
124 water demand fields explicitly describe the annual cycle (vegetation, rice) or annual time evolution (water
125 demand) and therefore have more stringent requirements regarding the data source. Global single-source datasets
126 (e.g. Te Chow, 1959; Supit et al., 1994; Allen et al., 1998; Buchhorn et al., 2021) were favoured to regional and/
127 or multiple data sources that needed to be combined in order to produce the required data unless sub-set
128 information was of much better quality (e.g. Moiret-Guigand, 2021). CEMS_SurfaceFields_2022 surface fields
129 are based on 25 different data sources and consist of 140 gridded fields grouped into six following groups: (i)
130 catchment morphology and river network, (ii) land use, (iii) vegetation cover type and properties, (iv) soil
131 properties, (v) lake information, and (vi) water demand.
132 Considering the high resolution (i.e. hundreds of meters) and volume of data (i.e. GB) of most input datasets used
133 to generate the surface fields, a high performing data manipulation platform was needed. GEE (Gorelick et al.,
134 2017) was selected as it provides (embedded) a vast high resolution data catalogue (e.g. ready available MERIT
135 DEM elevation dataset, CGLS-LC100 and CLC2018 land cover datasets) and powerful computation capabilities.
136 It also allows to upload any raster and vector data (e.g. GeoTiff or shapefiles) and to conduct each surface field
137 tailored computations. All GEE scripts were written in JavaScript to produce GeoTiff files, which were converted
138 to the final file format (NetCDF) locally after transfer from GEE platform.
139 To ensure a consistent representation of physical processes at all scales, surface fields should be as coherent as
140 possible among each other – between variables and across scales. Coherency can be achieved by using, where
141 possible, the same input datasets to derive different field types (e.g. unique forest information input to create all
142 forest-related surface fields), and making sure spatial aggregation or disaggregation across scales results in
143 expected values. Figure 1 shows a simplified scheme that relates input datasets (e.g. CGLS-LC100) with the
144 resulting surface fields (e.g. surface cover fractions – forest, inland water, and sealed surface fraction fields), also
145 highlighting fields requiring intermediary and sequential steps (e.g. forest fraction is needed to create soil
146 parameter fields over forested and non-forested areas).
147 For processes with horizontal dependency such as river routing, the relationship between grid cells (e.g. how the
148 grid cells are connected) must be defined first so that all dependent fields can be generated on the same grid
149 coordinates, spatial resolution and using consistent input data. For example, local drainage direction (LDD)
150 defines how water moves across the model grid cells as a river drainage network (see Figure 2) and strongly
151 depends on elevation data (see Section 3 for more details). Because of the complex spatial dependency of a river
152 drainage network, LDD must be created directly from elevation data at the required grid and resolution and cannot
153 be resampled from a previous LDD field of a different grid and/ or resolution. It is then used to define information
154 on the river network, including upstream drainage area and gradient. Note, that Figure 1 misses an arrow from

155 MERIT DEM to LDD only because this step was mainly done by CaMa-Flood developers (see Section 3.2 for
156 more details).
157 Four steps are involved in generating a particular surface field (see Table 1), with step 3 being the most complex
158 and varied (see Figure 2 for an example), and step 4 being necessary only for some model specifications (here as
159 required by LISFLOOD, see Table 2).
160 All techniques applied (see Table 1) to generate CEMS_SurfaceFields_2022 are reproduceable to different input
161 data and/ or for different output data specifications. Further details on specific manipulations associated with each
162 field category are given in sections below as relevant, where each. Each section has a table with exact data source
163 used per surface field, and step-by-step description of transformations applied to the data to compute the final
164 fields included in CEMS_SurfaceFields_2022 (full technical descriptions for all fields are explained in the
165 LISFLOOD user guide, available online: https://ec-jrc.github.io/lisflood-code/4_Static-Maps-introduction/, last
166 accessed: 21.01.2024). Although the specific requirements for the dataset were defined by LISFLOOD for EFAS
167 (European domain, 1 arc min resolution at mid-latitude of the domain (47.50 N) is ~1.25 km) and GloFAS (Global
168 domain)and GloFAS implementation, summarised in Table 2, they are consistent with requirements of any other
169 environmental models. Regional examples of a sub-set of CEMS_SurfaceFields_2022 are provided to show the
170 level of detail available at each resolution and field, and to emphasise the consistency through all the fields, a
171 critical requirement for environment modelling and analysis,. Examples are focusing on three regions of the world:
172 the Po River (Europe), the Amazon River (South America) and the Brahmaputra River (Asia), with additional
173 examples provided in Appendix 4).
174
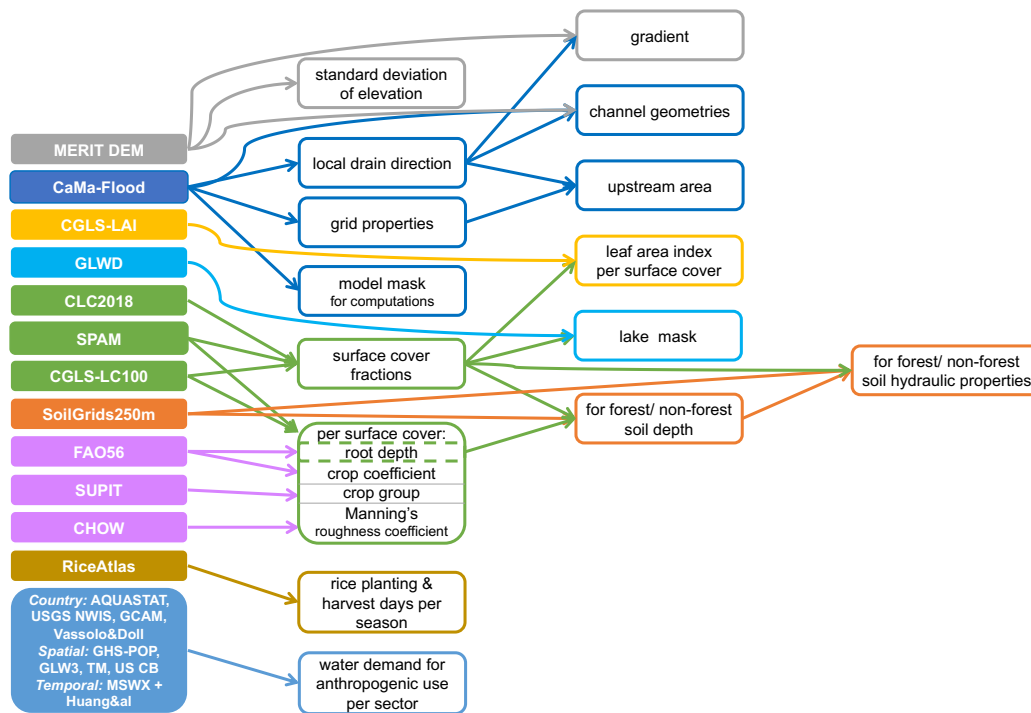
176 **Figure 1. Flow chart connecting input datasets and surface fields created. Dashed border denotes intermediate fields,**
177 **that are not part of the final dataset catalogue.**
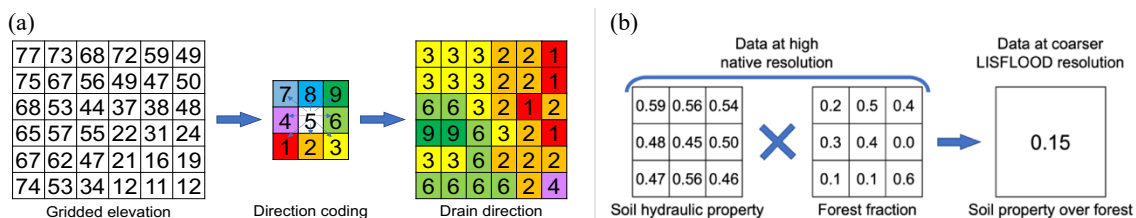
178 **Figure 2. Examples of data manipulation for (left column, plot a) transformation of elevation data into LDD (done**
179 **within CaMa-Flood), and (right column, plot b) upscaling with weighted average for one final grid cell of soil hydraulic**
180 **property over forested area.**

181 **Table 1. The four steps of a particular surface field generation and associated data manipulations.**

Order	Description	Purpose	Function
1	Raw file preparation	Vector gridding, region merging	
		Upscaling (spatial/ temporal aggregation)	Arithmetic mean, mode, sum, standard deviation (weighted) resampling from auxiliary data
2	Unit conversion	Converting values from native to fraction per grid cell	Surface area, percentage or categorical to fractions per grid cell (see Appendix 2 for more details)
3	Value computation	Transforming	Mathematical equation/ function needed to generate the output variable
		Reprojecting	Interpolation (changing grid, preserving resolution in meters)
		Upscaling (spatial [default]/ temporal aggregation)	Arithmetic mean, mode, sum, standard deviation (weighted) resampling from auxiliary data (changing resolution, preserving grid)
		Downscaling (spatial [default]/ temporal disaggregation)	Nearest neighbour (changing resolution, preserving grid)
		Limiting	Force a minimum/ maximum value to satisfy e.g. calculation precision, physical meaning and/ or model requirement
4	Zero/ NoData filling	Replace zero/ NoData by the most appropriate values	LIGHT. Constant value, unweighted global mean, unweighted global mode
			DEEP. Values from next coarser resolution (up to an agreed maximum resolution); if still missing, method LIGHT

182

183 **Table 2. Dataset files technical specifications.**

Type	Specification
Format	NetCDF
Projection	EPSG:4326 - WGS84: World Geodetic System
Horizontal resolution	Europe: 1 ~~arc min~~arcminute (~1.86 km at the equator) [file size 4530x2970 grid cells]
	Globe: 3 ~~arc min~~arcminute (~5.57 km at the equator) [file size 7200x3600 grid cells]
Domain bound	Europe: [North = 72.25 N; South = 22.75 N; West = 25.25 W; East = 50.25 E]
	Globe: [North = 90.00 N; South = 90.00 S; West = 180.00 W; East = 180.00 E]
Missing value (i.e. NoData) location	Over land: none
	Over ocean: all ocean grid cells have missing value (i.e. ocean is masked based on 'mask' field)
Missing value (i.e. NoData) number	For Integer variable type: 0
	For Real variable type: -999999.0
Variable type	Integer: Int8
	Real: Float32

3 Catchment morphology and river network

184

3.1 General information

185

186 Morphology and channel shape information are essential for the computation of snow melting, temperature
187 scaling, and river routing. ~~Statistics such as~~Alternatively, standard deviation of elevation and other orographic
188 sub-grid parameters are critical for radiation parametrization, especially for shadowing effect~~, whilst channel~~.
189 Channel geometry fields are needed to describe overbank inundation and infer inundated areas in wetland methane
190 and soil carbon modelling~~, for example.~~. Land morphology is derived from elevation and its variability within a
191 single cell can be represented through slope, standard deviation, aspect, etc. River drainage information, derived
192 from elevation, is used to connect the model cells according to the direction of the surface runoff, with channel
193 geometry information used for routing processes.
194 The dataset contains 14 morphology and river network variables (~~name~~names in brackets in italics correspond to
195 the ~~field's name~~field names in the data repository):

- 196 • Morphologic information: local drainage direction (i.e. flow direction from one cell to another; *LDD*,
- 197 dimensionless), upstream drainage area (*upArea*, m²), grid cell area (*pixarea*, m²), grid cell length
- 198 (*pixleng*, m), standard deviation of elevation (*elvstd*, m), gradient (i.e. elevation gradient; *gradient*, m/m);
- 199 • Kinematic wave equation for routing: channel bottom width (*chanbw*, m), channel length (*chanlenght*,
- 200 m), channel gradient (*changrad*, m/m), Manning's roughness coefficient for channels (*chanman*, s/m$^{1/3}$);
- 201 • River network information: channel mask (i.e. presence of river channel; *chan*, dimensionless), channel
- 202 side slope (i.e. channel's horizontal distance divided by vertical distance; *chans*, m/m);

203   •   Open water evaporation: bankfull channel depth (*chanbnkf*, m), channel flood plain (i.e. width of the area
204   where the surplus of water is distributed when the water level in the channel exceed the channel depth;
205   *chanflpn*, m).

206   **3.2 Reference data and methodology**

207   Environmental models require an accurate description of terrain and hydro-morphology to represent the
208   hydrodynamics at the spatial resolution of the model. Here all catchment morphology and river network fields are
209   derived from (i) The Catchment-based Macro-scale Floodplain (CaMa-Flood) Global River Hydrodynamics
210   Model v4.0 maps (further referred as CaMa-Flood)— that include information on channel length, river topography
211   parameters, floodplain elevation profile, channel width and channel depth at 3 and 1 arc min resolutions covering
212   land area from 90 N to 60 S, representative of the year 2017,), and (ii) The MERIT DEM: Multi-Error-Removed
213   Improved-Terrain Digital Elevation Model v.1.0.3 (further referred as MERIT DEM)— a high-accuracy global
214   DEM at 3 arc second resolution (~ 90 m at the equator) covering land area from 90 N to 60 S, representative of
215   the year 2018 (for). For reference data details see Appendix 1)-. All fields follow a complex sequential workflow
216   (see Figure 3 and Table 1). Note that whilst some river network fields were already directly available from the
217   CaMa-Flood catalogue (e.g. LDD, channel length), they had to be adapted to the specific requirements of
218   LISFLOOD-. Fields also had to be specifically consistent with an interconnected river network described by the
219   D8 algorithm (O'Callaghan and Mark, 1984; Figure 2a) different to that used by the CaMa-Flood algorithm.
220
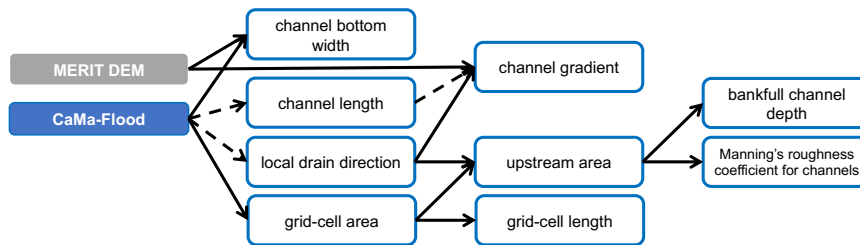
221
222   **Figure 3. Workflow of complex manipulations to create some of the morphology and river network fields; solid arrows**
223   **indicate a function transformation, dashed – modification of existing input data to LISFLOOD specifications.**

224   **Table 1. Morphology and river network fields, their description, data source and applied transformation; * denotes**
225   **transformation following Burek et al. (2014); name in brackets in italics next to each field correspondcorresponds to**
226   **the name in the data repository.**

Field type	Description	Data source (variable)	Transformation
Local drainage direction (*LDD*)	Connects every grid cell forming a river network from springs to mouth	CaMa-Flood (flwd)	Direction coding, ensuring grid cell connectivity
Grid cell area (*pixarea*)	Area of every grid cell	CaMa-Flood (flwd)	Grid cell area based on a given coordinate reference system and resolution
Grid cell length (*pixlength*)	Length of every grid cell	*pixarea*	$pixlength = \frac{pixarea}{resolution}$, where *resolution* – 1.86 km and 5.57 km for 1 and 3 arc minarcminute respectively
Upstream drainage area (*upArea*)	Accumulated area of all connected grid cells of the LDD from springs (start; lowest values) to mouth (end; highest values)	*LDD*; *pixarea*	PCRaster Accuflux function (Karssenberg et al., 2010)
Standard deviation of elevation (*elvstd*)	Amount of elevation variation within a grid cell	MERIT DEM	Upscaling (spatial) with standard deviation
Gradient (*gradient*)	Elevation gradient between two connected grid cells	MERIT DEM; *LDD*	$gradient = \frac{abs(elv_{uc} - elv_{dc})}{D_{uc,dc}}$, where *elv* – elevation, *uc* and *dc* – upstream and downstream cell, $D_{uc,dc}$ – distance between upstream and downstream cells
Channel bottom width (*chanbw*)	Width of the bottom of the channel	CaMa-Flood (width); *upArea*	Recomputing zero and negative values based on equation* $chanbw = upArea \cdot 0.0032$
Channel length (*chanlength*)	Length of river channel in each grid cell (can exceed	CaMa-Flood (rivlen)	No transformation was carried out

	grid-size to account for meandering river)		
Channel gradient (*changrad*)	Gradient (slope) of river channel inside a grid cell	MERIT DEM; *LDD*; *chanlength*	$changrad = \frac{abs(elv_{uc} - elv_{dc})}{chanlength_{uc}}$, where elv – elevation, uc and dc – upstream and downstream cell; Note: LDD is used to define uc and dc
Manning's roughness coefficient for channels (*chanman*)	Manning's roughness coefficient of river channel for each grid cell	MERIT DEM; *upArea*	Transformation based on equation* $chanman = 0.25 + 0.015 \cdot \min\left(\frac{50}{upArea_{km^2}}, 1\right) + 0.030 \cdot \min\left(\frac{elv_m}{2000}, 1\right)$, where elv – elevation, km^2 and m – values in km^2 and m
Channel mask (*chan*)	Channel presence in the grid cell indicator. Note LISFLOOD specific requirement to have channels in every 'mask' grid cell	'mask' (main model's field)	Channel mask is equal to 1 everywhere
Side slope (*chans*)	Slope of river banks (i.e. horizontal distance divided by vertical distance)		Side slope of all channels is 45°, hence side slope is equal to 1 everywhere
Bankfull channel depth (*chanbnkf*)	Channel depth (i.e. river bed depth)	*upArea*	Transformation based on equation* $chanbnkf = 0.27 \cdot upArea_{km^2}^{0.33}$, where km^2 – values in km^2

3.3 Regional examples

Most fields in catchment morphology and river network category are quite technical and hard to interpret. The ones that can be easy digested are upstream area and standard deviation of elevation which are presented in Figure 4 for Po River area in 1 ~~arc min~~ and 3 ~~arc min~~arcminute resolution, and in Figure 5 for Amazon River and Brahmaputra River areas at 3 ~~arc min~~arcminute resolution. The field of standard deviation of elevation shows high level of detail over the Brahmaputra River and the benefit of high resolution dataset is clearly seen over the Po River.
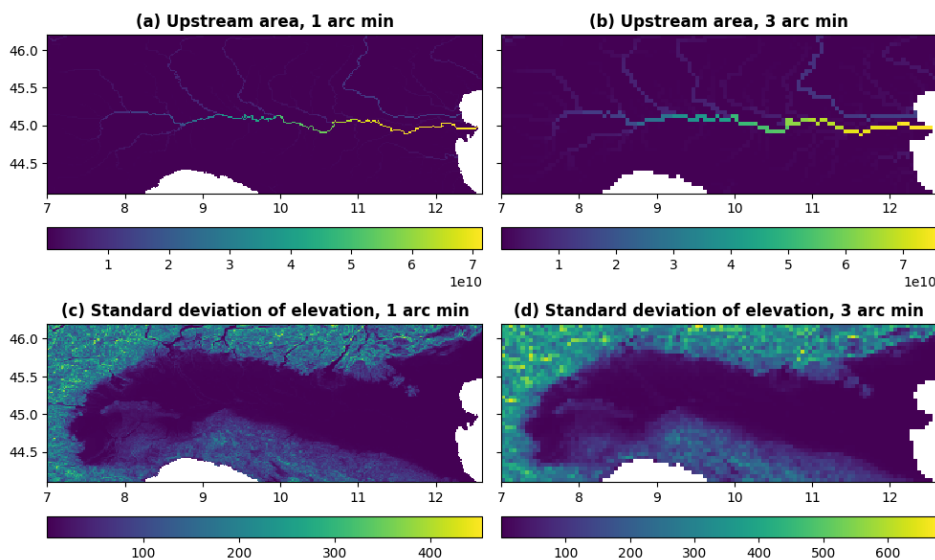
Figure 4. Upstream drainage area in square meters (upper row, plots a and b) and standard deviation of elevation in meters (lower row, plots c and d) at 1 ~~arc min~~arcminute (~1.9 km at the equator, left column, plots a and c) and 3 ~~arc min~~arcminute (~5.6 km at the equator, right column, plots b and d) resolution for Po River area in Italy.
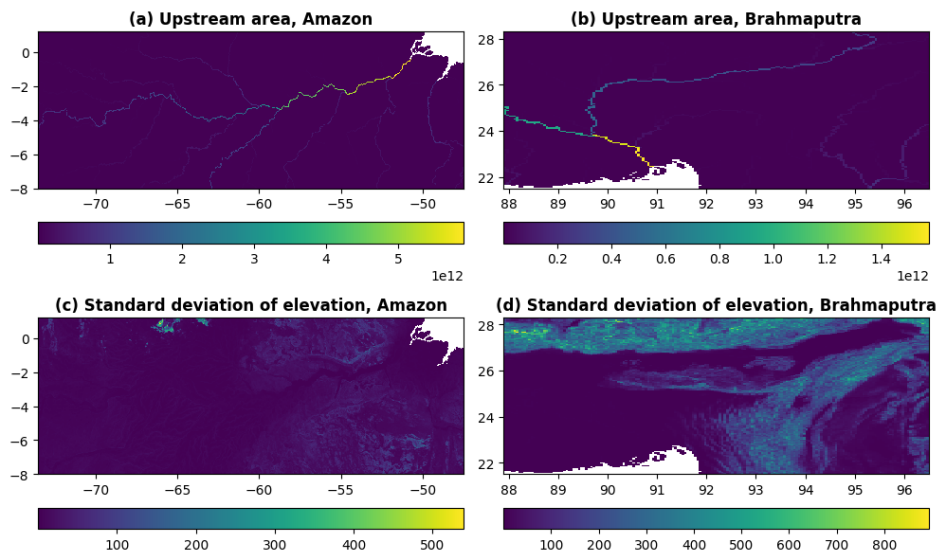
Figure 5. Upstream drainage area in square meters (upper row, plots a and b) and standard deviation of elevation in meters (lower row, plots c and d) at 3 ~~are min~~arcminute (~5.6 km at the equator) resolution for Amazon River area (left column, plots a and c) and Brahmaputra River area (right column, plots b and d).

4 Land use fields

4.1 General information

Land use is an essential component of environmental models. Many models use a sub-grid cell approach where a single grid cell can include several different land uses with each land use being subject to different prominent physical processes. This approach allows to keep a high level of accuracy when representing how different types of land cover affect e.g. the hydrological cycle (e.g. evaporation is different in urban areas compared to forests) while limiting the increase in computational time. Application of land surface fractions ~~include~~includes grid cell weighted average skin temperature calculations, biogenic flux calculations, urban planning, and climate mitigation plan preparation. For example, sealed surface fraction is necessary for carbon budget calculations and trace gas emissions in general, more explicitly for anthropogenic and residential emission calculations~~, and irrigated~~. Irrigated crop and irrigated rice fractions (combined with rice planting and harvesting days) useful for crop yield and methane emissions modelling.

The dataset differentiates between six different land uses (~~name~~names in brackets in italics correspond to the ~~field's name~~field names in the data repository):

- Forest: areas where the main hydrological processes are canopy interception, evapotranspiration from canopies, canopies drainage and evapotranspiration, root uptake and evaporation from the soil (fraction of forest; *fracforest*, dimensionless fraction);
- Sealed surface: impervious areas where there is no water infiltration into the soil, i.e. water is accumulated in the surface depression, yet evaporates, but once the depression is full, water is transported by a surface runoff (fraction of sealed surface; *fracsealed*, dimensionless fraction);
- Inland water: open water bodies where the most prominent hydrological process is evaporation (fraction of inland water; *fracwater*, dimensionless fraction);
- Irrigated crops: areas used by agriculture – water is abstracted from ground water and surface water bodies to irrigate the fields. The main hydrological processes connected with the irrigated crops are canopy interception, evapotranspiration from canopies, canopies drainage and evapotranspiration, root uptake and evaporation from the soil (fraction of all irrigated crops, excluding rice; *fracirrigated*, dimensionless fraction);
- Irrigated rice: areas used to grow rice with flooded irrigation agricultural technique, when water is abstracted from the inland water bodies and delivered to the rice fields. The main hydrological processes connected with rice fields are soil saturation, flooding, rice growing phase, soil drainage phase (fraction of irrigated rice; *fracrice*, dimensionless fraction);
- Other land cover: used in canopy interception, evaporation from the canopies, canopy drainage, plant evapotranspiration, evaporation from the soil hydrological processes. The relative importance of these processes depends on the LAI (fraction of other cover types; *fracother*, dimensionless fraction).

4.2 Reference data and methodology

In models explicitly accounting for sub-grid variability, the fraction of each land use in every cell must be provided so that process representation for each land use can be weighted accordingly. Here the majority of land use fields are derived from The Copernicus Global Land Service (CGLS) Land Cover (LC) 100m map (further referred as CGLS-LC100) — a set of global land cover maps at 100 m resolution covering land and ocean area from 90 N to 60 S, representative of the year 2015; rest of the land use fields (i.e. irrigated). Irrigated crops and irrigated rice fractions) are derived from (i) The Spatial Production Allocation Model (SPAM) – Global Spatially-Disaggregated Crop Production Statistics Data for 2010 v2.0 (further referred as SPAM2010) — a global dataset with crop distribution and production information at 10 km (5 arc min) resolution covering land area from 90 N to 60 S, representative of the year 2010,), and (ii) The Coordination of Information on the Environment (CORINE) Land Cover (CLC) inventory for 2018 (further referred as CLC2018) — a set of maps describing the land cover/ land use status at 100 m resolution covering land area over Europe (i.e. 39 countries), representative of the time period 2017-2018 (for). For reference data details see Appendix 1).. The derivation of fractions of the five land use classes used in LISFLOOD (and additional ocean fraction for consistency check) each followfollows specific steps (see Figure 6) summarised in Table 2. Note that LISFLOOD requires all 'mask' (main model's field) grid cells to have at least one non-zero fraction type, hence. Hence the extra step in the generation of the inland water fraction field was to set empty grid cells (i.e. grid cells that based on the data source are fully covered with ocean) as fully covered with inland water.
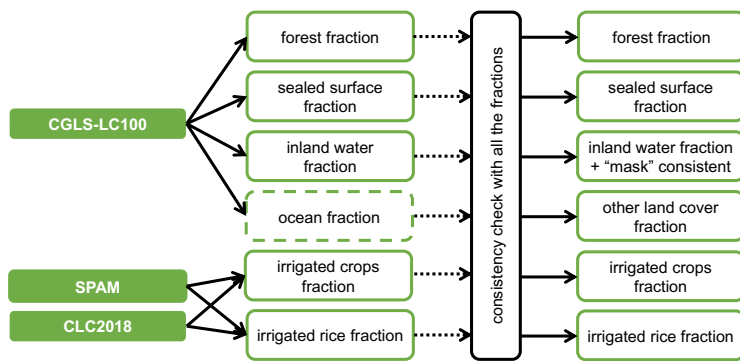
Figure 6. Workflow of complex manipulations to create land use fields; solid arrows indicate a function transformation, dotted – upscaling; dashed boxes indicate the intermediate fields used for other field generation.

Table 2. Fraction of land use fields, their description, data source and applied transformations; 'sum' refers to the sum of all fractions except 'other land cover fraction'; cells with bold italics show required intermediate fields; name in brackets in italics next to each field correspondcorresponds to the name in the data repository.

Field type	Description	Data source (variable)	Transformation (in order)
Forest fraction (*fracforest*)	Evergreen and deciduous needle leaf and broad leaf tree areas	CGLS-LC100 (tree-coverfraction)	Unit conversion % to fraction; Reprojecting and upscaling to final grid and resolution with mean; Consistency check with other fractions
Sealed surface fraction (*fracsealed*)	Urban areas, characterizing the human impact on the environment	CGLS-LC100 (urban-coverfraction)	Unit conversion % to fraction, scaled by 0.75[7]; Reprojecting and upscaling to final grid and resolution with mean; Consistency check with other fractions
Inland water fraction (*fracwater*)	Rivers, freshwater and saline lakes, ponds and other permanent water bodies over the continents	CGLS-LC100 (water-permanent-coverfraction)	Force Fox Basin and Caspian Sea to be fully covered with water; Unit conversion % to fraction; Reprojecting and upscaling to final grid and resolution with mean; Consistency check with other fractions; Cross-checking with 'mask' and forcing empty grid cells as inland water
Irrigated crops fraction (*fracirrigated*)	Irrigated areas of all possible crops excluding rice	SPAM (spam2010v1r0_global_physi	Shapefile gridding to its native resolution (~10 km); Unit conversion ha to fractions;

---

[7] For the sealed surface fraction, it is assumed that water can infiltrate in roughly 25 % of urban areas at kilometre scale through e.g. trees along the road, bushes along the fence, grass or moss between concrete tiles or cobble stones.

		cal-area_CROP_i, 41 crops rice excluding)	Reprojecting and downscaling to CLC2018 grid and resolution (~100 m) with nearest neighbour
		CLC2018 (landcover = '212')	Unit conversion class to fraction
			Merging SPAM- and CLC2018-derived fractions, priority to CLC2018; Reprojecting and upscaling to final grid and resolution with mean; Consistency check with other fractions
Irrigated rice fraction (*fracrice*)	Irrigated areas of rice	SPAM (spam2010v1r0_global_physical-area_RICE_i)	Shapefile gridding to its native resolution (~10 km); Unit conversion ha to fractions; Reprojecting and downscaling to CLC2018 grid and resolution (~100 m) with nearest neighbour
		CLC2018 (landcover = '213')	Unit conversion class to fraction
			Merging SPAM- and CLC2018-derived fractions, priority to CLC2018; Reprojecting and upscaling to final grid and resolution with mean; Consistency check with other fractions
Other land cover fraction (*fracother*)	Agricultural areas, non-forested natural area, pervious surface of urban areas	Non-negative residual from 1 subtracting 'sum' of all other fractions	$fracother = \max((1-sum),0)$
Ocean fraction (*fracocean*)	Oceans	CGLS-LC100 (discrete_classification = '200')	Unit conversion class to fraction; Forcing NoData to zero over 'mask' grid cells, otherwise – fully covered; Reprojecting and upscaling to final grid and resolution with mean; Consistency check with other fractions

To ensure consistency between fractions, the sum of all fraction fields must be 1 at any resolution. When sum is greater than 1, the inland water fraction value is assumed correct (input data corrected prior computation over Fox Basin and Caspian Sea) and all other fractions are corrected ($fracXX$) following Eq. (1):

$$fracXX = fracXX_{raw}\left(1 - \frac{fracwater_{raw}+fracocean_{raw}+fracforest_{raw}+fracsealed_{raw}+fracirrigated_{raw}+fracrice_{raw}-1}{fracforest_{raw}+fracsealed_{raw}+fracirrigated_{raw}+fracrice_{raw}}\right), \quad (1)$$

where *raw* refers to the original (i.e. before consistency check) fraction of *XX* which can be the forest, irrigated crops, rice and sealed surfaces.

The generated fraction fields, e.g. forest (see Figure 7a) and other land cover (see Figure 7b), have generally good consistency with other up-to-date products like ESA CCI Land Cover time-series v2.0.7 (ESA CCI map viewer https://maps.elie.ucl.ac.be/CCI/viewer/, last accessed: 21.01.2024; Defourny et al., 2017).
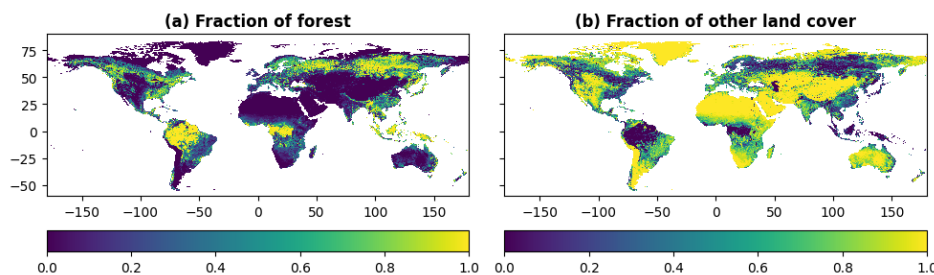
Figure 7. Fraction of forest (left column, plot a) and fraction of other land cover (right column, plot b) at 3 ~~arc min~~arcminute (~5.6 km at the equator) resolution for global region.

4.3 Regional examples

All fields in land use category are easy to interpret as they represent the fraction of grid cell covered by one or another surface cover type. The most interesting ones are fraction of forest, fraction of inland water, fraction of irrigated crops, and fraction of rice ~~which~~. These fractions are presented in Figure 8 for Po River area in 1 ~~arc min~~ and 3 ~~arc min~~arcminute resolution, and in Figure 9 for Amazon River and Brahmaputra River areas at 3 ~~arc min~~arcminute resolution. ~~With~~Figures show high level of detail visible for the fields of fraction of forest and fraction of inland water (e.g. Amazon River) especially at the highest spatial resolution (Po River).

323
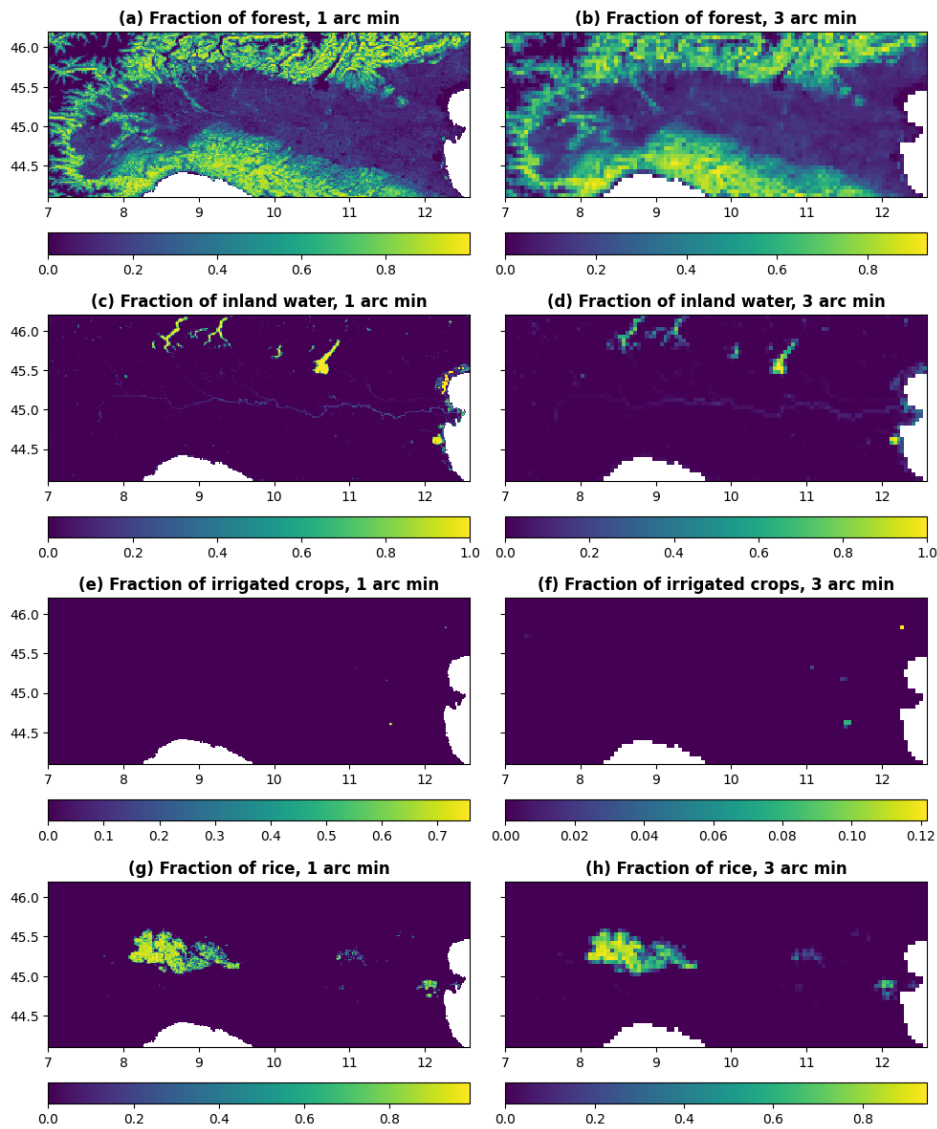
324
325 **Figure 8. Fraction of forest (upper row, plots a and b), fraction of inland water (second row, plots c and d), fraction of**
326 **irrigated crops (third row, plots e and f), and fraction of rice (lower row, plots g and h) at 1 ~~arc min~~arcminute (~1.9**
327 **km at the equator, left column, plots a, c, e and g) and 3 ~~arc min~~arcminute (~5.6 km at the equator, right column, plots**
328 **b, d, f and h) resolution for Po River area in Italy.**
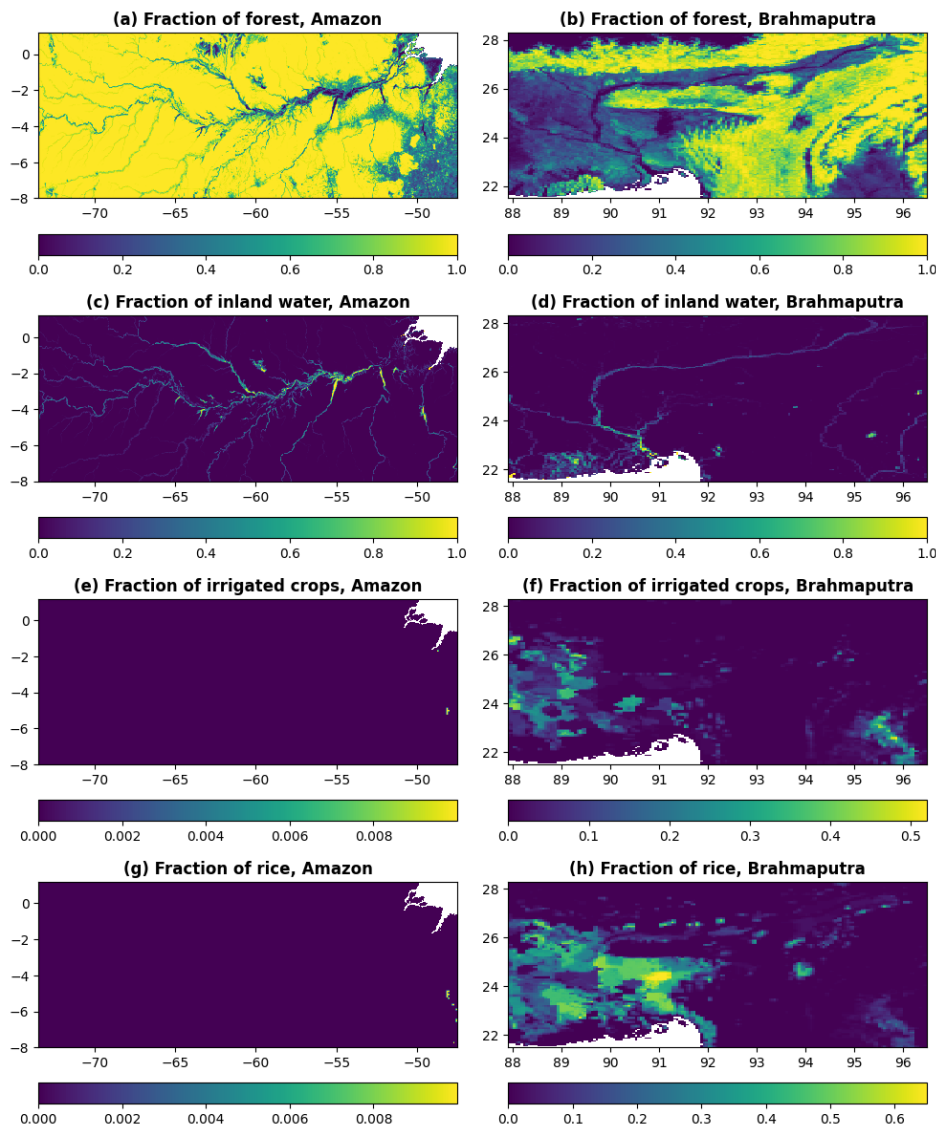
Figure 9. Fraction of forest (upper row, plots a and b), fraction of inland water (second row, plots c and d), fraction of irrigated crops (third row, plots e and f), and fraction of rice (lower row, plots g and f) at 3 ~~are min~~arcminute (~5.6 km at the equator) resolution for Amazon River area (left column, plots a, c, e and g) and Brahmaputra River area (right column, plots b, d, f and h).

5 Vegetation properties

5.1 General information

Vegetation-related information contributes to the computation of precipitation interception, evaporation, transpiration, and root water uptake. Depending on the model, vegetation dynamics can be represented with different degrees of complexity including in hydrology processes, vegetation growth and feedback on climate (Bonan et al., 2002). Rice being the world's most important food crop and having specific water demands, its water cycle is often considered explicitly~~, with~~. Rice planting and harvesting dates being critical information to represent the inter-annual variability in its water demand, provided the maximum three growing seasons. The variables allow to model how vegetation affects the hydrology, with a particular focus on root water uptake and transpiration depending on vegetation type and vegetation state (e.g. water stress conditions). For example, the crop group number depends on the critical amount of soil moisture below which water uptake from plants is reduced as they start closing their stomata. Alternative use of fields such as the Leaf Area Index LAI ~~include~~includes biomass allocation, which can be used for fire danger forecasting, and carbon stock monitoring~~, whilst rice~~. Rice planting/ harvesting days are important for yearly cycle of methane modelling.

The dataset describes vegetation properties through four variables (note that LAI consists in total of 36 10-day average fields) for each of forest (_f), irrigated crops (_i) and other land cover types (_o), and another six (two types times three seasons) variables for rice (~~name~~names in brackets in italics correspond to the ~~field's name~~field names in the data repository):

- Transpiration rate: crop coefficient (*cropcoef_f*, *cropcoef_i*, *cropcoef_o*, dimensionless);
- Water uptake: crop group number (*cropgrpn_f*, *cropgrpn_i*, *cropgrpn_o*, dimensionless);
- Surface runoff generation and water routing: Manning's surface roughness coefficient (*mannings_f*, *mannings_o*, s/m$^{1/3}$), rice planting and harvesting days (*riceplantingday1*, *riceplantingday2*, *riceplantingday3*, calendar day number; *riceharvestday1*, *riceharvestday2*, *riceharvestday3*, calendar day number);
- Water interception and evaporation: leaf area index (*laif*, *laii*, *laio*, m^2/m^2).

5.2 Reference data and methodology

In complement to the land use fraction, the distribution of vegetation type and characteristics is required to capture the difference in environmental processes such as water intake of evaporation to be represented accurately. Here the vegetation properties are derived from many data sources using maps to account for the species spatial distribution (i.e. CGLS-LC100 and SPAM2010) and tables to obtain associated hydro-dynamics properties for crops, e.g. (i) The Food and Agriculture Organisation (FAO) of the United Nations Irrigation and Drainage Paper No. 56 (further referred as FAO56~~) — a publication covering geographically referenced statistics for crop development stages, crop coefficients, crop height, rooting depth, and soil water depletion fraction for common crops found across the world, (ii)~~ **Burek** ~~et al. (2014) — a publication covering summarised information for crop coefficients, rooting depth, crop group number and Manning's surface roughness coefficient for different surface types, (iii)~~ **Intara** ~~et al. (2018) — a publication covering oil palm roots architecture,~~). and (iv) The Wofost 6.0 crop simulation model description (further referred as SUPIT~~) — a publication covering crop group information for several crops as examples, and relation of a crop group from water depletion fraction;~~); for river hydraulics The Open-Channel Hydraulics manual (further referred as CHOW~~) — a publication containing information on roughness coefficient over different surfaces.~~). Time evolution of vegetation is based on The Copernicus Global Land Service (CGLS) Leaf Area Index (LAI) 1km Version 2 collection (further referred as CGLS-LAI~~) — a set of global maps without missing data describing vegetation dynamics at 10-day intervals at 1 km resolution covering land area from 90 N to 60 S and representative of the 10-year period of 2010-2019;~~); time evolution of crops is based on The RiceAtlas v3 (further referred as RiceAtlas~~) — a spatial database of global rice calendars and production at 1 km resolution for the national production totals to match the years 2010-2012 (for~~). For reference data details see Appendix 1~~).~~. This requires assumptions to be made in case different sources did not contain the same information, and transformations to be applied depending on the vegetation type. The main data sources and general transformation steps (see Figure 10) to derive the 18 vegetation properties fields are summarised in Table 3 and following text. Note that 'crop group number' variable corresponds to a water depletion value and can be averaged across different crop types.
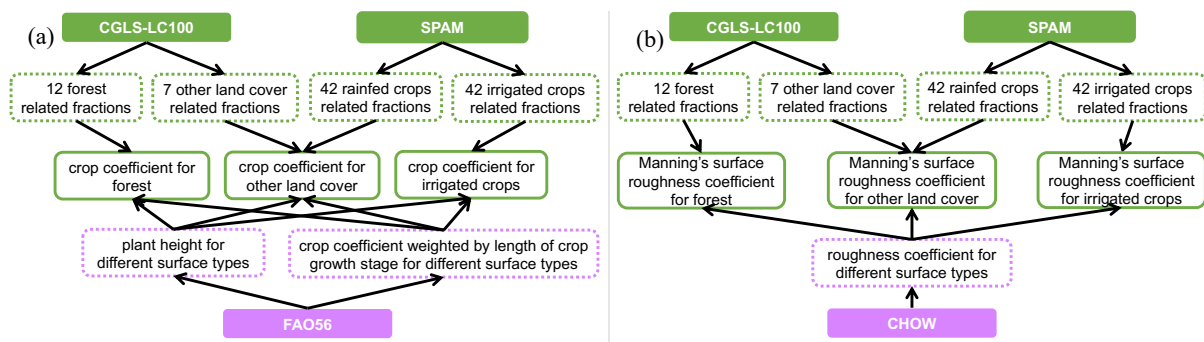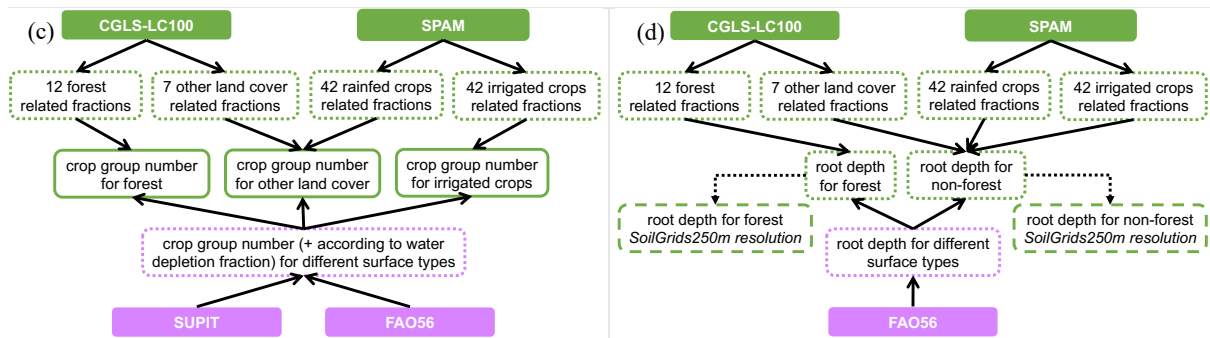
Figure 10. Workflow of complex manipulations to create some of the vegetation property fields, e.g. crop coefficient (left column, upper row, plot a), Manning's surface roughness coefficient (right column, upper row, plot b), crop group number (left column, lower row, plot c), root depth (right column, lower row, plot d); solid arrows indicate a function transformation, dotted – upscaling; dashed boxes indicate the intermediate fields used for other field generation, dotted – the fields only used for the vegetation-related fields.

Table 3. Vegetation property fields, their description, data source and applied transformations; cells with bold italics show required intermediate fields; name in brackets in italics next to each field ~~correspond~~corresponds to the name in the data repository.

Field type	Description	Data source	Transformation (in order)
Crop coefficient for forest, irrigated crops and other land cover type (*cropcoef_f*, *cropcoef_i*, *cropcoef_o*)	Ratio between the potential (reference) evapotranspiration rate, in mm/day, and the potential evaporation rate of a specific crop (averaged by time and ecosystem type)	CGLS-LC100 (discrete_classification = '111', '112', '113', '114', '115', '116', '121', '122', '123', '124', '125', '126' [forest types], '20', '30', '40', '60', '70', '90', '100' [other land cover types])	Force Fox Basin and Caspian Sea to be fully covered with water; Unit conversion class to fraction (in total 12 forest related and 7 other land cover related fraction fields); Reprojecting and upscaling to final grid and resolution with mean
		SPAM (spam2010v1r0_global_physical-area_CROP_i/r, 42 crops, 'i' – irrigated, 'r' – rainfed)	Shapefile gridding to its native resolution (~10 km); Unit conversion ha to fractions (in total 42 irrigated crop related and 42 rainfed crop related fraction fields); Reprojecting and downscaling to final grid and resolution with nearest neighbour; Limiting values to 0.0-1.0 interval
		FAO56 (Table 11, 12 – information on crop coefficient and crop height); Intara et al. (2018); Burek et al. (2014)	Average crop coefficient value across climate zones for each crop growing stage and crop/ land cover type; Weighted average of crop coefficient per different crop growth stages (weighted by stage duration in days if available, otherwise mean); Average crop height value across climate zones for each crop/ land cover type
			Weighted average of relevant crop coefficient for forest, irrigated crops and other land cover type (weighted by crop height and fraction) following Eq. (2); Note: for other land cover type computation of crop coefficient of all rainfed crops is used for CGLS-LC100 (discrete_classification = '40'); Zero/ NoData filling with global mean
Crop group number for forest, irrigated crops and other land cover type (*cropgrpn_f*, *cropgrpn_i*, *cropgrpn_o*)	Represents a vegetation type and is an indicator of its adaptation to dry climate (averaged by ecosystem type)	CGLS-LC100 (discrete_classification = '111', '112', '113', '114', '115', '116', '121', '122', '123', '124', '125', '126' [forest types], '20', '30', '40', '60', '70', '90', '100' [other land cover types])	Same steps as for crop coefficient
		SPAM (spam2010v1r0_global_physical-	Same steps as for crop coefficient

		area_CROP_i/r, 42 crops, 'i' – irrigated, 'r' – rainfed)	
		FAO56 (Table 22 – information on crop depletion fraction); SUPIT (Table 6.1, 6.2 – information on crop groups); Burek et al. (2014)	Applying function (SUPIT) to water depletion fraction (FAO56) for each crop/ land cover type $cropgrpn = 10 \cdot fr_{dep} - 1.5$, where fr_{dep} – water depletion fraction; Limiting values to 1.0-5.0 interval; Note: if fr_{dep} missing – using precomputed crop group number (Burek et al., 2014)
			Same steps as for crop coefficient, but in Eq. (2) weighted by fraction only
Manning's surface roughness coefficient for forest and other land cover type (*mannings_f*, *mannings_o*)	Roughness or friction applied to the flow by the surface on which water is flowing (averaged by ecosystem type)	CGLS-LC100 (discrete_classification = '111', '112', '113', '114', '115', '116', '121', '122', '123', '124', '125', '126' [forest types], '20', '30', '40', '60', '70', '90', '100' [other land cover types])	Same steps as for crop coefficient
		SPAM (spam2010v1r0_global_physical-area_CROP_i/r, 42 crops, 'i' – irrigated, 'r' – rainfed)	Same steps as for crop coefficient
		CHOW (Table 5, 6 – information on roughness coefficient n); Burek et al. (2014)	Matching roughness coefficient for each crop/ land cover type
			Same steps as for crop coefficient, but in Eq. (2) weighted by fraction only
Leaf area index for forest, irrigated crops and other land cover type (*laif*, *laii*, *laio*)	Defined as half the total area of green elements of the canopy per unit horizontal ground area m^2/m^2 (10-day average; 36 fields in total)	CGLS-LAI 10-day average for 2010-2019; *fracforest*; *fracirrigated*; *fracother*	Upscaling to final temporal resolution (in total 36 LAI fields); Reprojecting and upscaling to final grid and spatial resolution with unweighted mean; Filtering sparce areas of relevant fractions $fr < 0.7$, where fr – fraction; NoData filling DEEP (upscaling to 1, 3, 15 ~~are min~~arcminute, 1, 3, 15, 60 degrees spatial resolution with unweighted mean; replacing NoData at final resolution with first available precomputed less coarser resolution, if not – with zero)
Rice planting day (*riceplantingday1*, *riceplantingday2*, *riceplantingday3*)	Most probable day of the year when rice is planted for the first, second and third time	RiceAtlas (PLANT_PKn, 3 seasons)	Ordering planting seasons by increasing Julian day (in total 3 planting dates per spatial unit); Shapefile gridding to final grid and spatial resolution (in total 3 fields); Note: if less than 3 seasons – repeating last available planting/ harvesting seasons date; NoData filling with global unweighted mode date of first planting/ harvesting season (i.e. 105 – 15th April/ 227 – 15th August)
Rice harvest day (*riceharvestday1*, *riceharvestday2*, *riceharvestday3*)	Most probable day of the year when rice is harvested after planting for the first, second and third time	RiceAtlas (HARV_PKn, 3 seasons)	
Root depth for forest and non-forest (*root_depth_f*, *root_depth_o*)	Deepest soil depth reached by the crop roots	CGLS-LC100 (discrete_classification = '111', '112', '113', '114', '115', '116', '121', '122', '123', '124', '125', '126' [forest types], '20', '30', '40', '60', '70', '90', '100' [other land cover types])	Same steps as for crop coefficient
		SPAM (spam2010v1r0_global_physical-area_CROP_i/r, 42 crops, 'i' – irrigated, 'r' – rainfed)	Same steps as for crop coefficient

| | | FAO56 (Table 22 – information on crop rooting depth); Burek et al. (2014) | Matching rooting depth for each crop/ land cover type |
| | | | Same steps as for crop coefficient, but in Eq. (2) weighted by fraction only; Downscaling to native SoilGrids250m resolution with nearest neighbour (for soil depth calculations) |

393
394 The final step of the crop coefficient, crop group number, Manning's surface roughness coefficient, and additional
395 crop height (for crop coefficient calculation) and root depth (for soil depth calculation, see Section 6.2) for forest,
396 irrigated crops and other land cover type is to compute weighted average of their components (e.g. different forest
397 types) following Eq. (2):
398 $K = \frac{A_1 \cdot fr_1 \cdot K_1 + A_2 \cdot fr_2 \cdot K_2 + \cdots + A_N \cdot fr_N \cdot K_N}{A_1 \cdot fr_1 + A_2 \cdot fr_2 + \cdots + A_N \cdot fr_N},$ (2)
399 where A is a scaling parameter (equals 1, except for crop coefficient where it equals to crop height), fr refers to
400 the fraction of crop or land cover type, K – default (i.e. source table based) variable in question values, $1..N$ –
401 number of crop or land cover types included in the field (i.e. for forest $N=12$, irrigated crops $N=41$, other land
402 cover type $N=7$ and for CGLS-LC100 type '40' (cropland) default values are based on 42 rainfed crops).
403 The generated vegetation property fields, e.g. crop coefficient for forest (see Figure 11a) and other land cover (see
404 Figure 11b), follow main features of e.g. generated forest fraction.
405
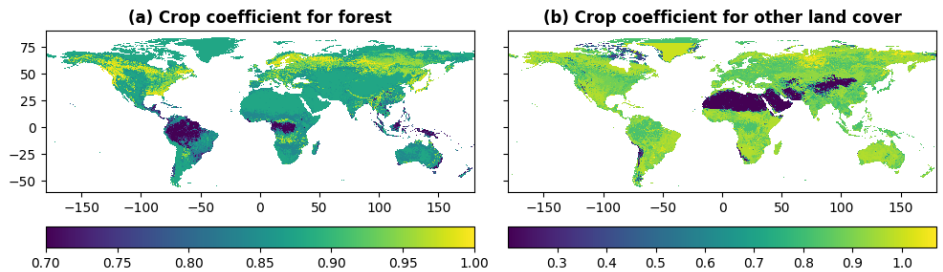
406
407 **Figure 11. Crop coefficient for forest (left column, plot a) and crop coefficient for other land cover type (right column,**
408 **plot b) at 3** ~~are min~~arcminute **(~5.6 km at the equator) resolution for global region.**

409 **5.3 Regional examples**

410 All fields in the vegetation properties category are complementary to the land use fractions, and help to understand
411 for example the difference in evaporation water intake. The fields easiest to interpret are the crop coefficient and
412 the crop group number which are presented for forest in Figure 12 for Po River area in 1 ~~arc min~~ and 3 ~~are~~
413 ~~min~~arcminute resolution, and in Figure 13 for Amazon River and Brahmaputra River areas at 3 ~~are min~~arcminute
414 resolution. For example, fields of crop group number for forest (i.e. different forest ~~type~~types) show transition of
415 vegetation resilience towards dry conditions in the Brahmaputra River area.
416
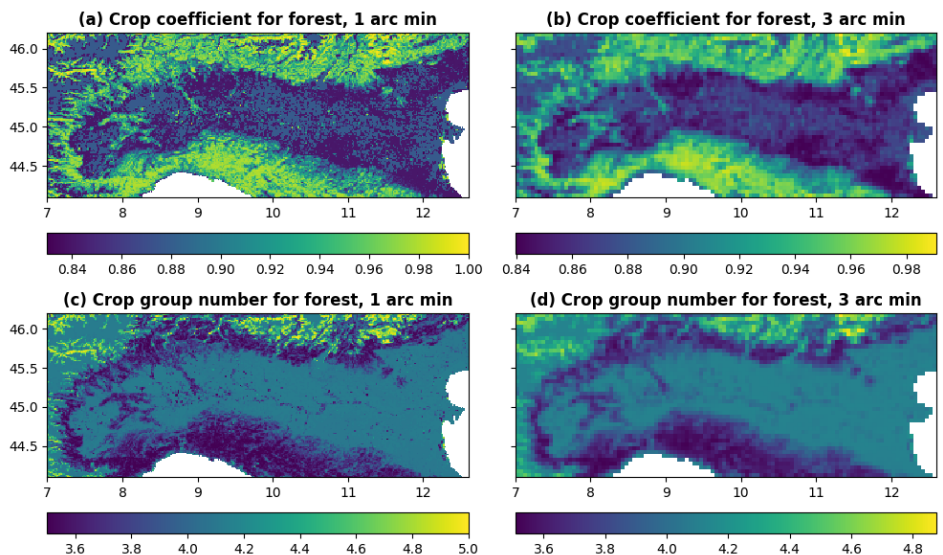
417

418 **Figure 12. Crop coefficient for forest (upper row, plots a and b) and crop group number for forest (lower row, plots c**
419 **and d) at 1 ~~are min~~arcminute (~1.9 km at the equator, left column, plots a and c) and 3 ~~are min~~arcminute (~5.6 km at**
420 **the equator, right column, plots b and d) resolution for Po River area in Italy.**
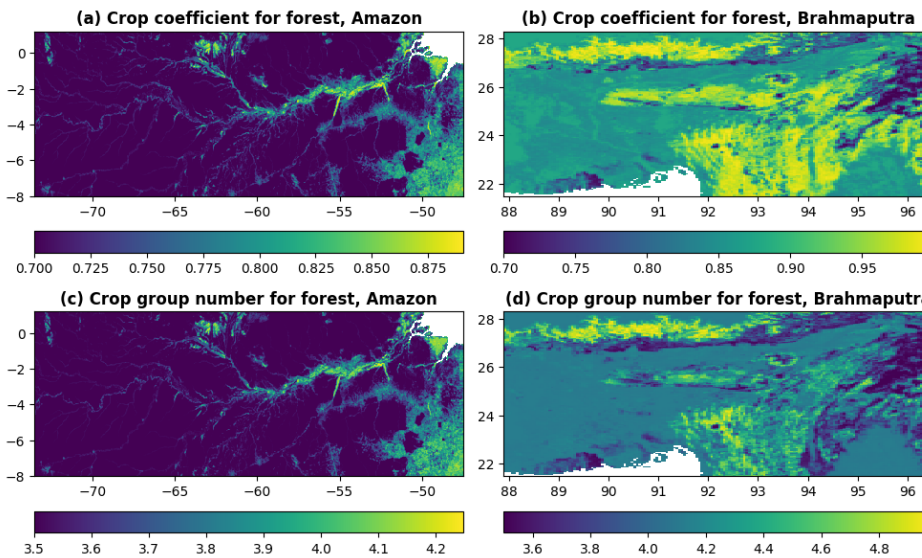
421
422 **Figure 13. Crop coefficient for forest (upper row, plots a and b) and crop group number for forest (lower row, plots c**
423 **and d) at 3 ~~are min~~arcminute (~5.6 km at the equator) resolution for Amazon River area (left column, plots a and c)**
424 **and Brahmaputra River area (right column, plots b and d).**

6 Soil properties
425

6.1 General information
426

427 In land surface and distributed hydrological models, the water movement, storage and plants' water-uptake from
428 the soil are often described by the soil~~/~~ / water retention curve (SWRC). The SWRC is derived empirically by
429 measuring how water is retained and released by different soil types. Throughout time different SWRC have been
430 developed and integrated into models~~, the~~. The most widely applied are Van Brooks and Corey (Brooks and
431 Corey, 1964), Fredlund and Xing (Fredlund and Xing, 1994), van Genuchten (van Genuchten, 1980), and Gardner
432 (Gardner, 1956) SWRCs. Different SWRC equations require different parameters, some shared between different
433 SWRC concepts, e.g. referring to physical soil characteristics such as water saturated and unsaturated content,
434 hydraulic conductivity and pore size, others uniquely describing the SWRC function shape, not directly related to
435 soil properties. Often, for computational reasons, the soil profile from ground level to bedrock depth is sliced into
436 layers, at the modeller's choice, and the SWRC function is applied to each soil layer. Alternative use of soil
437 properties is for soil moisture calculations.
438 The dataset includes variables required to apply the Van Genuchten SWRC equations (van Genuchten, 1980) to
439 describe the water dynamics through a vertical soil profile composed of three layers (1, 2, 3~~), each~~). Each variable
440 is required for each soil layer and for forest (_f) or non-forest (_o) land use, with different soil depth in forest (_f)
441 and non-forest (_o) areas following root depth values from Allen at al. (1998), ~~further~~ referred as FAO56, (total
442 of 29 variables; ~~name~~names in brackets in italics correspond to the ~~field's name~~field names in the data repository):

- Soil profile: surface layer depth (*soildepth1_f*, *soildepth1_o*, mm), middle layer depth (*soildepth2_f*,
443 *soildepth2_o*, mm), subsoil depth (*soildepth3_f*, *soildepth3_o*, mm);
444
445 - Soil hydraulic properties: saturated (*thetas1_f*, *thetas1_o*, *thetas2_f*, *thetas2_o*, *thetas3*, m^3/m^3) and
446 residual (*thetar1*, *thetar2*, *thetar3*, m^3/m^3) volumetric soil moisture content, pore size index (*lambda1_f*,
447 *lambda1_o*, *lambda2_f*, *lambda2_o*, *lambda3*, dimensionless), Van Genuchten equation parameter
448 (*genua1_f*, *genua1_o*, *genua2_f*, *genua2_o*, *genua3*, cm^{-1}), saturated soil conductivity (*ksat1_f*, *ksat1_o*,
449 *ksat2_f*, *ksat2_o*, *ksat3*, mm/day).

6.2 Reference data and methodology
450

451 Soil proprieties are derived from The International Soil Reference and Information Centre (ISRIC) SoilGrids250m
452 global gridded soil information release 2017 (further referred as SoilGrids250m~~) – an output of special predictions~~
453 ~~produced by the SoilGrids system, as a set of global soil property and class maps on soil characteristics at six~~

454 ~~standard depths, including soil textures (clay, silt, sand), depth to bedrock, bulk density, organic carbon, pH and~~
455 ~~cation exchange capacity at 250 meters resolution covering land area with no permanent ice and representative~~
456 ~~for the year 2010 (for reference data details see Appendix 1); and~~). For reference data details see Appendix 1. Soil
457 proprieties are computed for both forested and non-forested (also known in literature as 'others') areas, expressed
458 as fractions (main source is forest fraction based on CGLS-LC100, see Section **~~Error! Reference source not~~**
459 **~~found.~~**),4.2), where non-forested area is the complementary fraction of forest. Soil depth layers are derived first
460 and used as input to the soil hydraulic equations used to derive the properties, following a sequential workflow
461 (see Figure 14 and Table 4). Equations used are from Toth et al. (2015).
462
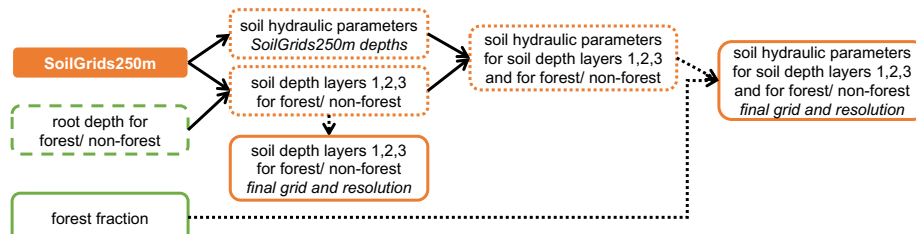
463
464 **Figure 14. Workflow to generate the soil related fields; solid arrows indicate a function transformation, dotted –**
465 **upscaling; dashed boxes indicate the intermediate fields used for other field generation, dotted – the fields only used**
466 **for the soil-related fields; 'SoilGrids250m depths' – fields at the SoilGrids250m native grid and resolution with six**
467 **default depths, 'final grid and resolution' – fields at the dataset's final grid and resolution, boxes with no explicit**
468 **indication – fields at SoilGrids250m native grid and resolution only.**

469 **Table 4. Soil property fields, their description, and applied transformations; name in brackets in italics next to each**
470 **field ~~correspond~~corresponds to the name in the data repository.**

Field type	Description	Data Source	Transformation (in order)
Soil depth layers 1, 2, 3 for forest and non-forest (*soildepth1_f, soildepth1_o, soildepth2_f, soildepth2_o, soildepth3_f, soildepth3_o*)	Root depths assumed to divide the total soil depth between topsoil (surface [layer 1] and middle [layer 2]) and subsoil (bottom [layer 3])	SoilGrids250m (absolute_depth_to_bedrock); *root_depth_f*; *root_depth_o*	Transforming at SoilGrids250m native grid and resolution as described in Appendix 3 'Soil Depth' (in total 3 forest and 3 non-forest soil depth layer fields); Reprojecting and upscaling to final grid and resolution with unweighted mean; NoData filling DEEP (upscaling to 1, 3, 15 ~~are min~~arcminute, 1, 3, 15, 60 degrees spatial resolution with unweighted mean; replacing NoData at final resolution with first available precomputed less coarser resolution, if not – with zero)
Saturated volumetric soil moisture content for soil depth layers 1, 2, 3, and for forest and non-forest (*thetas1_f, thetas1_o, thetas2_f, thetas2_o, thetas3*)	Saturated water content soil hydraulic property representing the maximum water content in the soil	SoilGrids250m (clay_content, silt_content, bulk_density); *soildepth1_f; soildepth1_o; soildepth2_f; soildepth2_o; soildepth3_f; soildepth3_o; fracforest*	Transforming at SoilGrids250m native grid and resolution as described in Appendix 3 'Soil hydraulic parameters' (in total 5 fields per soil hydraulic parameter, except *thetar* – only 3 as no forest/ non-forest separation); Limiting values and weighting by forest/ non-forest fraction (limits $thetas < 1.0$, $thetar < thetas$, $lambda \leq 0.42$, $genua \leq 0.055$, $ksat > 0.0$); Upscaling to final grid and resolution with unweighted mean; NoData filling DEEP (upscaling to 1, 3, 15 ~~are min~~arcminute spatial resolution with unweighted mean; replacing NoData at final resolution with
Residual volumetric soil moisture content for soil depth layers 1, 2, 3 (*thetar1, thetar2, thetar3*)	Residual water content soil hydraulic property representing the minimum water content in the soil	SoilGrids250m (clay_content, silt_content); *soildepth1_f; soildepth1_o; soildepth2_f; soildepth2_o; soildepth3_f; soildepth3_o; fracforest*	
Pore size index for soil depth layers 1, 2, 3, and for forest and non-forest (*lambda1_f, lambda1_o, lambda2_f, lambda2_o, lambda3*)	Van Genuchten parameter λ (also referred as 'n-1' in literature) soil hydraulic property representing the pore size index of the soil	SoilGrids250m (clay_content, silt_content, bulk_density, organic_carbon_content); *soildepth1_f; soildepth1_o; soildepth2_f; soildepth2_o; soildepth3_f; soildepth3_o; fracforest*	

Van Genuchten equation parameter for soil depth layers 1, 2, 3, and for forest and non-forest (*genua1_f*, *genua1_o*, *genua2_f*, *genua2_o*, *genua3*)	Van Genuchten parameter α soil hydraulic property	SoilGrids250m (clay_content, silt_content, bulk_density, organic_carbon_content); *soildepth1_f*; *soildepth1_o*; *soildepth2_f*; *soildepth2_o*; *soildepth3_f*; *soildepth3_o*; *fracforest*	first available precomputed less coarser resolution, if not – with global unweighted mean)
Saturated soil conductivity for soil depth layers 1, 2, 3, and for forest and non-forest (*ksat1_f, ksat1_o, ksat2_f, ksat2_*o, *ksat3*)	Saturated hydraulic conductivity soil hydraulic property representing the ease with which water moves through pore spaces of the soil	SoilGrids250m (clay_content, silt_content, soil_pH, cation_exchange_capacity); *soildepth1_f*; *soildepth1_o*; *soildepth2_f*; *soildepth2_o*; *soildepth3_f*; *soildepth3_o*; *fracforest*	

471

472 Two of the most common soil parameters of land surface and hydrological models, saturated hydraulic
473 conductivity *ksat* and saturated water content, are shown in Figure 15.
474 Saturated hydraulic conductivity *ksat* (see Figure 15a) ranges from 2 to 7445 mm/day. The highest *ksat* values are
475 concentrated in desertic areas such as the Sahara, Arabian Peninsula, Gobi, Patagonian, Sonoran-Mojave and
476 Kalahari and Namib deserts. Low *ksat* between, 2 and 18 mm/day, are found in the Amazon river basin, the lower
477 Mississippi river basin and South East Asia. *ksat* was visually compared against 8 global datasets developed with
478 different input data and/ or PTFs (Zhang and Schaap, 2019; Gupta et al., 2021); a general agreement is noticeable
479 in areas that show low variability across all datasets. Northern Russia, Canada, South East Asia and Sonoran-
480 Mojave Desert are the areas with high variability among datasets, with values ranging from very low to very high
481 *ksat*. Source of uncertainties in *ksat* values are primarily due to little availability of soil samples and measurements
482 carried out in those areas. Moreover, the climatic context plays a relevant role in clay mineralogy composition,
483 organic composition and soil pores structure (Hodnett and Tomasella, 2002), which influence how water flows
484 through the soil. Therefore, the PTF developed using soil samples collected in temperate areas (such as Europe)
485 are expected to have a different hydraulic behaviour compared to those collected in tropical climates (Gupta et
486 al., 2021), as also seen in Figure 15a.
487 Saturated water content (see Figure 15b) ranges between 0.27 to 0.79, with 80% of values between 0.40 and 0.46.
488 A comparison with other global datasets was not carried out, however uncertainties are expected to be of the same
489 order of magnitude than those of *ksat* given the fact the saturated water content is calculated using bulk density
490 and clay content data.

491
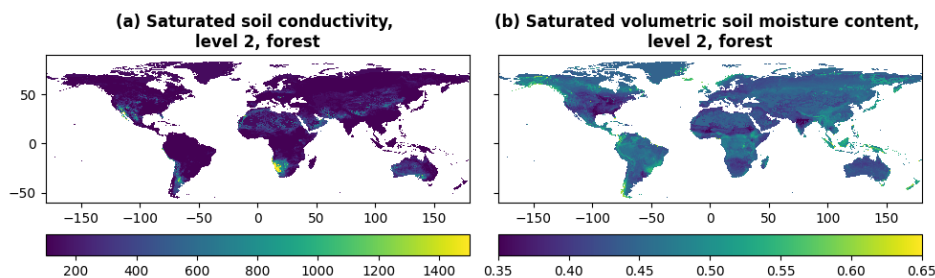
492
493 **Figure 15. Saturated soil hydraulic conductivity for forested areas of soil depth layer 2 in mm per day (left column,**
494 **plot a) and saturated volumetric soil moisture (i.e. water) content for forested areas of soil depth layer 2 (right column,**
495 **plot b) at 3 ~~are min~~arcminute (~5.6 km at the equator) resolution for global region.**

496 **6.3 Regional examples**

497 The majority of soil properties fields are easy to interpret. Saturated soil conductivity *ksat* and saturated volumetric
498 soil moisture content are presented for forested areas of soil depth layer 2 in Figure 16 for the Po River area in 1
499 ~~are min~~ and 3 ~~are min~~arcminute resolution, and in Figure 17 for the Amazon River and the Brahmaputra River
500 areas at 3 ~~are min~~arcminute resolution. The field of saturated soil conductivity for forest shows how easy it is for
501 water to penetrate soil depending on forest type~~, and the~~. The field of saturated volumetric soil moisture content
502 shows what is the maximum amount of water that the soil can absorb depending on forest type. These fields have
503 interesting features over Brahmaputra River area.

504
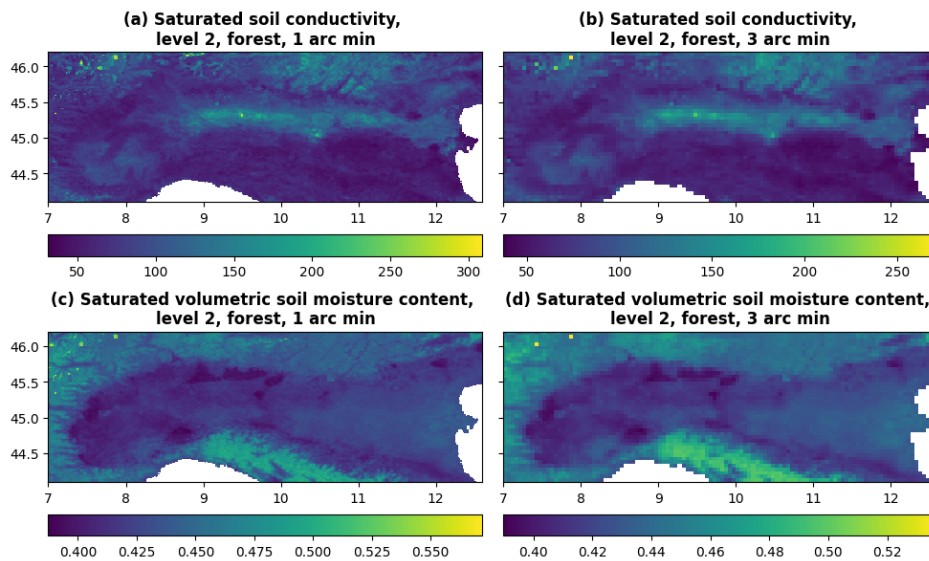
Figure 16. Saturated soil hydraulic conductivity for forested areas of soil depth layer 2 in mm per day (upper row, plots a and b) and saturated volumetric soil moisture (i.e. water) content for forested areas of soil depth layer 2 (lower row, plots c and d) at 1 ~~are min~~arcminute (~1.9 km at the equator, left column, plots a and c) and 3 ~~are min~~arcminute (~5.6 km at the equator, right column, plots b and d) resolution for Po River area in Italy.
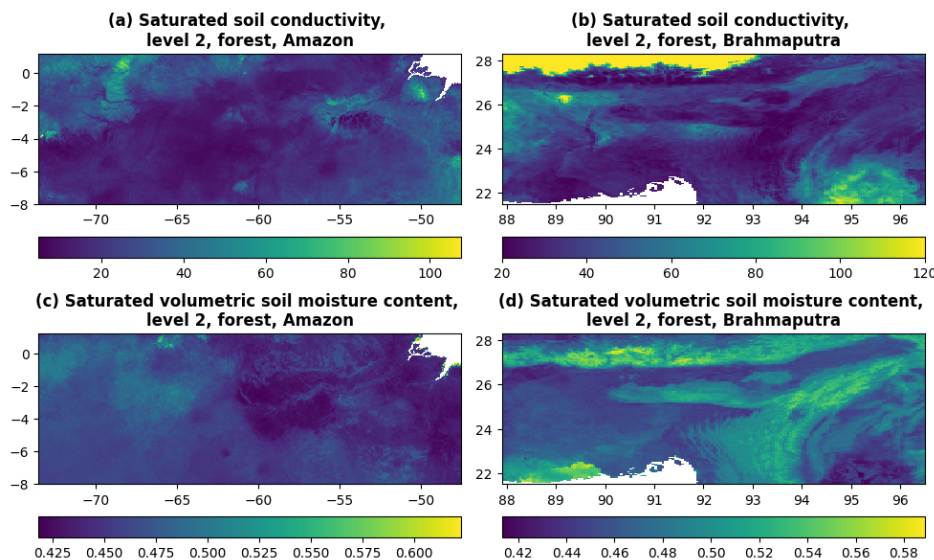
Figure 17. Saturated soil hydraulic conductivity for forested areas of soil depth layer 2 in mm per day (upper row, plots a and b) and saturated volumetric soil moisture (i.e. water) content for forested areas of soil depth layer 2 (lower row, plots c and d) at 3 ~~are min~~arcminute (~5.6 km at the equator) resolution for Amazon River area (left column, plots a and c) and Brahmaputra River area (right column, plots b and d).

7 Lakes

7.1 General information

Lakes (and reservoirs) are important as they influence river discharge variability but also the atmosphere regionally and globally. The area covered by lakes can be used for computing evaporation from open water, freshwater storage, unregulated surface water extent, fresh water scarcity indexes, and biogenic green house gas emission, as well as for reproducing different climate mitigation scenarios. The CEMS_SurfaceFields_2022 dataset only includes data on lake extent and not reservoirs (generally smaller~~), described as a lake~~). Lake mask ~~where~~describes the presence of lakes, is consistent with fraction of inland water~~; the~~. The field's name in the data repository is *lakemask*, dimensionless~~).~~.

7.2 Reference data and methodology

The lake mask field is derived from The Global Lakes and Wetlands Database (further referred as GLWD) — a global database of water bodies at spatial resolutions of up to 1:1 million — GLWD-1 with 3067 largest lake and 654 largest reservoir polygons, and GLWD-2 with ~250000 smaller lake and reservoir polygons (see Table 7).). For reference data details see Appendix 1, for workflow see Table 7.

Table 5. Lake field, its description, data source and transformation; name in brackets in italics next to the lake field corresponds to the name in the data repository.

Field type	Description	Data source	Transformation (in order)
Lake mask (*lakemask*)	Area covered by lakes only (binary representation)	GLWD (GLWD-1, GLWD-2, lake type only); *fracwater*	Filtering non-lake spatial units; Shapefile gridding to final grid and resolution; If *fracwater* > 0 and GLWD is 'lake', then *lakemask* is 1, otherwise 0

7.3 Regional examples

The lake mask field is easy to interpret as it shows which grid cells from fraction of inland water field have lakes. The lake mask field is presented in Figure 18 for Po River area inat 1 are min and 3 are minarcminute resolution, and in Figure 19 for Amazon River and Brahmaputra River areas at 3 are minarcminute resolution, where it shows. Figures show the abundance of lakes over Amazon River area and detailed lake shapes over Po River area described by the 1 are minarcminute resolution field.
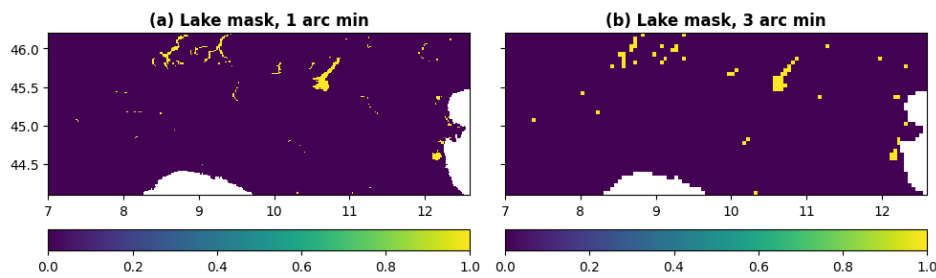
Figure 18. Lake mask at 1 are minarcminute (~1.9 km at the equator, left column, plot a) and 3 are minarcminute (~5.6 km at the equator, right column, plot b) resolution for Po River area in Italy.
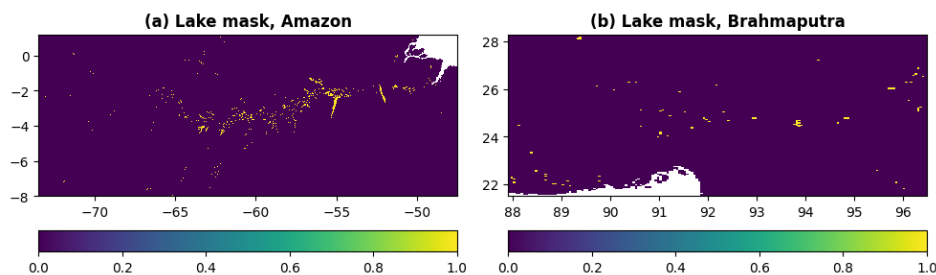
Figure 19. Lake mask at 3 are minarcminute (~5.6 km at the equator) resolution for Amazon River area (left column, plot a) and Brahmaputra River area (right column, plot b).

8 Water demand

8.1 General information

Some environmental models explicitly represent a number of the human interventions impacting on the water cycle. One of the most common is water demand, which represents the withdrawal of water from natural water sources (e.g. rivers, reservoirs, groundwater) to satisfy the water demand for anthropogenic use. The segregation of the total water demand for anthropogenic use into four main sectors, namely domestic, energy, industrial, and livestock water withdrawal, enables a more accurate representation of the processes, and follows the Food and Agriculture Organisation of the United Nations (FAO) terminology (Kohli et al., 2012). Domestic water withdrawal represents indoor and outdoor household water use as well as other uses (e.g. industrial and urban agriculture) connected to the municipal system (e.g., water use by shops, schools, and public buildings). Electricity

555 (energy) water withdrawal is the water use for the cooling of thermoelectric and nuclear power plants. Water
556 withdrawal for industry is the water used for fabricating, processing, washing, cooling or transporting products,
557 also includes water within the final products and water used for sanitation within the manufacturing facility.
558 Livestock withdrawal is the demand for drinking and cleaning purposes of livestock.
559 Higher accuracy in environmental modelling is achieved by differentiating water demand sources and by
560 allocating different levels of priority to different usages. Within LISFLOOD, for instance, water demand for the
561 energy sector and flooded irrigation (rice crops) is supplied by surface water bodies only, while non. Non-flooded
562 irrigation, domestic, industrial, livestock water demand can be supplied by both groundwater and surface water
563 bodies. Moreover, domestic water demand has the highest priority in case of water scarcity conditions.
564 It must be noted that the fields of water demand for agriculture are not included in this dataset because LISFLOOD
565 computes crops water demand internally by accounting for climatic conditions, information on land cover (see
566 Section 4.2), crops properties (see Section 5.2), and soil properties (see Section 6.2). Conversely, fields
567 representing the volume of water to satisfy the domestic, energy, industrial, and livestock demand must be
568 provided as input. Domestic, industrial, energy, and livestock water demand volumes have seasonal (e.g. due to
569 temperature differences) and inter-annual variations (e.g. due to population changes and different economic
570 conditions). In order to account for this variability, in LISFLOOD the four sectoral water demand fields provide
571 daily water demand data with monthly or annual variability from 01.01.1979 to 31.12.2019: the. The water
572 demand values are provided in mm/day, one field per month (the first day of each month is used as representative
573 timestamp for the entire month) for domestic and energy demand, one value per year (the monthly fields are
574 repeated twelve times per each year) for industrial and livestock demand.
575 Water availability, ecosystem long term ecological status, and anthropogenic needs must be accounted for to
576 evaluate the long term sustainability of water withdrawals. However, the spatial scales of water use data and
577 available water resources data often do not match due to different ways of data surveying and/or modelling
578 (McManamay et al., 2021; Zhang et al., 2023) and this creates a technical hurdle. Alternative use of the gridded
579 sectoral water demand information is e.g. for (i) the statistical analysis of long term spatiotemporal patterns and
580 trends of water demand; (ii) the evaluation of the long term sustainability and impacts of water withdrawals (e.g.
581 in connection to remote sensing-derived datasets of surface water extent or groundwater total storage); (iii) the
582 analysis of ecosystem–water–food–energy nexus (Karabulut et al., 2016); (iv) the evaluation of the impacts on
583 water resources of economical and price policies (Dolan et al., 2021); (v) the analysis of the responses in sectoral
584 water use during hydro climatic extremes (Belleza et al., 2023).
585 The CEMS_SurfaceFields_2022 dataset includes water demand for four main sectors (note that each sector
586 consists in total of 12 daily water demand fields per 41 (1979-2019) years, so 492 fields per sector) for
587 (namenames in brackets in italics correspond to the field's namefield names in the data repository): livestock (*liv*,
588 mm/day), industry (*ind*, mm/day), energy production, (*ene*, mm/day) and domestic use (*dom*, mm/day). The
589 temporal extension of the water demand fields presented in this manuscript includes the most recent information
590 of water demand at the time of the dataset's preparation. Readers that are interested in using more recent water
591 demand data are invited to follow the protocol presented in Section 8.2 to further extend in time the provided
592 fields.

593 **8.2 Reference data and methodology**

594 Global gridded water demand fields with monthly variability were generated for the four sectors using the main
595 data sources listed here and following the transformations summarised in Table 8 (for additional information and
596 extra details see GitHub repository 'lisflood-utilities/src/lisfloodutilities/water-demand-historic at master · ec-
597 jrc/lisflood-utilities · GitHub', last accessed: 21.01.2024): (i) AQUASTAT the FAO's global information system
598 with yearly country data on water resources and agricultural water management for "Gross Domestic Product
599 (GDP)", "Industry, value added to GDP", "Agricultural water withdrawal", "Industrial water withdrawal",
600 "Municipal water withdrawal", "Total water withdrawal", and "Irrigation water withdrawal";. (ii) United States
601 Geological Survey National Water Information System (further referred as USGS NWIS) a United States (US)
602 database on water use data for the annual state statistics for "Domestic total self supplied withdrawals, fresh, in
603 Mgal/d", "Public Supply total self-supplied withdrawals, fresh, in Mgal/d", "Industrial total self-supplied
604 withdrawals, fresh, in Mgal/d", "Total Thermoelectric Power total self supplied withdrawals, fresh, in Mgal/d",
605 "Total Thermoelectric Power power generated, in gigawatt hours", and "Livestock total self supplied
606 withdrawals, fresh, in Mgal/d"; (iii) **Global Change Analysis Model** (further referred as GCAM) an integrated,
607 multi-sector model's output that provides estimates on water withdrawals for energy, agriculture, and municipal
608 uses as lumped values of 235 hydrologic basins; (iv) **Global-scale gridded estimates of thermoelectric power
609 and manufacturing water use** (further referred as Vassolo and Doll, 2005) a global scale gridded on 0.5° by
610 0.5° grid estimate of water withdrawal for cooling of thermal power stations and for manufacturing, representative
611 for the year 1995; (v) **The Gridded Livestock of the World (GLW) version3** (further referred as GLW3) a
612 global-scale gridded on 0.083333° by 0.083333° (~10 km at the equator) grid of eight livestock species

613 distribution, representative for the year 2010; (vi) **World Bank manufacturing value added and gross domestic**
614 **product** (further referred as World Bank) — data provide "Manufacturing, value added (constant 2015 US$)"
615 values (further referred as MVA) and "Gross Domestic Product GDP (constant 2015 US$)" values; (vii), (iii)
616 Global Change Analysis Model (further referred as GCAM), (iv) The Gridded Livestock of the World (GLW)
617 version3 (further referred as GLW3), (v) The Global Human Settlement Population Grid multitemporal version
618 R2019A (further referred as GHS-POP) — a global-scale gridded on 9 arc sec (~ 300 m at the equator) grid
619 distribution of population, expressed as the number of people per grid cell, representative for the years 1975, 1990,
620 2000 and 2015; (viii) **Thematic Mapping Country Borders** shapefile (further referred as TM 'country borders')
621 — world country borders dataset; (ix) **The United States Census Bureau** Cartographic Boundary Files — Shapefile
622 (further referred as US CB) — the State boundaries for the USA, representative for the year 2018; (x) **Multi-Source**
623 **Weather** (further referred as MSWX) — a global-scale gridded high-resolution (3-hourly, 0.1°), bias-corrected
624 meteorological product with 2-meter daily and monthly maximum and minimum air temperature; (xi) **Huang et**
625 **al. (2018)** — a publication presenting 0.5° resolution global monthly gridded sectoral water withdrawal dataset for
626 the period 1971–2010 with calibrated R coefficient values and technique for temporal downscaling of domestic
627 and energy water demands.). For the full list of reference data and details see Appendix 1.
628 The water demand values are provided in mm/day, one field per month from 01.01.1979 to 31.12.2019 (the first
629 day of each month is used as the representative timestamp for the entire month). The methodology applied largely
630 follows Huang et al. (2018), with the key differences being the use of freely available datasets and the higher
631 resolution of the resulting fields. Spatial downscaling was achieved following the approach of Hejazi et al. (2014);
632 temporal downscaling was performed following the approaches of Wada et al. (2011), Voisin et al. (2013) and
633 Huang et al. (2018). It should be noted that country-scale estimates (from AQUASTAT) were integrated with
634 state-level water withdrawal estimates (from USGS NWIS). The protocol for the integration of local information
635 with global data sources was developed for further use in the future, to enable the integration of other regional or
636 national datasets as soon as they become available.
637
638 **Table 6. Water demand fields, their description, data source and applied transformations; cells with bold italics show**
639 **required intermediate fields; name in brackets in italics next to each field correspondcorresponds to the name in the**
640 **data repository.**

Field type	Description	Data source	Transformations (in order)
Population density (*pop*)	Number of people per grid cell	GHS-POP R2019A (1975, 1990, 2000, 2015)	Reprojecting and upscaling from native (9 arc sec) to the final grid and intermediate resolution of 0.01°x0.01° with sum (in total four fields); Transforming from population number to density per grid cell (i.e. dividing by grid cell area) and upscaling from intermediate to final resolution with mean (in total four fields); NoData filling (year) with linear interpolation till 2015, and with years 2000 and 2015 trend extrapolation 2016 onwards (pop_{year}^{grid}; in total 41 fields)
		TM 'country borders', US CB 'state borders'	Shapefile (country, US State) gridding to final grid and intermediate resolution of 0.01°x0.01°, then to final resolution; Transforming from population density per grid cell to population per country (i.e. multiplying by grid cell area and summing grid cells according to the country mask from step above; $pop_{year}^{country}$; in total one table)
Water demand for domestic use (*dom*)	Daily supply of water volume for indoor and outdoor household purposes and for all the uses that are connected to the municipal system (e.g., water used by shops, schools, and public buildings)	AQUASTAT (per country), USGS NWIS (per US State), *pop*	Unit conversion from native to km³/year; NoData filling (year): for countries – with linear interpolation and forward/ backward extrapolation based on $pop_{year}^{country}$, for US states – with linear interpolation and nearest neighbour extrapolation ($demand_{year}^{country}$, in total one table)
		pop, TM 'country borders', US CB 'state borders'	Transforming water demand ($demand_{year}^{country}$) to water demand per capita per country/ US State per year (in total one table): $perCapitaDemand_{year}^{country} = \frac{demand_{year}^{country}}{pop_{year}^{country}}$; NoData filling (country) with nearest neighbour; Transforming from water demand per capita to water demand per grid cell (i.e. weighting by pop_{year}^{grid}; in total one field per year): $demand_{year}^{grid} = perCapitaDemand_{year}^{country} \cdot pop_{year}^{grid}$
		MSWX, Huang et al. (2018) [Table 3, Eq. (2)].	Temporal downscaling (month) to account for the withdrawal fluctuations between the warmest and coldest months based on Huang et al. (2018) Eq. (2) (in total 12 fields per year):

			$demand_{month,year}^{grid} = \frac{demand_{year}^{grid}}{month_{year}^{number}} \cdot \left(\frac{\bar{T}_{month,year}^{grid} - avg\bar{T}_{year}^{grid}}{max\bar{T}_{year}^{grid} - min\bar{T}_{year}^{grid}} \cdot R + 1 \right)$, where $avg\bar{T}_{year}^{grid}$, $max\bar{T}_{year}^{grid}$, $min\bar{T}_{year}^{grid}$ are the average, maximum, minimum monthly temperatures in a year; $\bar{T}_{month,year}^{grid}$ is the average temperature in a month of the year; R is the amplitude of the monthly fluctuations from Huang et al. (2018) [Table 3]; $month_{year}^{number}$ is number of months in a year, i.e. 12; Temporal downscaling (day; in total 12 fields per year): $demand_{day,month,year}^{grid} = \frac{demand_{month,year}^{grid}}{day_{month}^{number}}$, where day_{month}^{number} is number of days in a month of a certain year
Water demand for industrial use (*ind*)	Daily supply of water volume for fabricating, processing, washing and sanitation, cooling or transporting a product, incorporating water into a product	AQUASTAT (per country), USGS NWIS (per US State), GCAM (per region), Vassolo and Doll (2005), World Bank (MVA), *pop*, TM 'country borders'	Unit conversion from native to km³/year; NoData filling (year; in total one table): • regional data – downscaling (spatial) to country values (i.e. weighting by $pop_{year}^{country}$), then linear interpolation (between years) and nearest neighbour extrapolation in time, finally rescaling values according to Vassolo and Doll (2005); • country data – with linear interpolation (between years) and forward/ backward extrapolation based on *MVA* or $pop_{year}^{country}$, value disaggregation from industrial water demand to manufacturing and thermoelectric water demands according to regional data results; • for US States data – with linear interpolation (between years) and nearest neighbour extrapolation; • mosaicking results from US States and country data, from regional data, if not – with zero
		pop, TM 'country borders', US CB 'state borders'	Transforming from water demand per country/ US State to per grid cell (i.e. weighting by $pop_{year}^{grid}/pop_{year}^{country}$; in total one field per year): $demand_{year}^{grid} = \frac{demand_{year}^{country}}{pop_{year}^{country}} \cdot pop_{year}^{grid}$; Temporal downscaling (day; in total one field per year): $demand_{day,year}^{grid} = \frac{demand_{year}^{grid}}{day_{year}^{number}}$, where day_{year}^{number} is number of days in a year
Water demand for thermoelectric use (*ene*)	Daily supply of water volume for the cooling of thermoelectric and nuclear power plants	AQUASTAT (per country), USGS NWIS (per US State), GCAM (per region), Vassolo and Doll (2005), World Bank (MVA), *pop*, TM 'country borders'	Same steps as for water demand for industrial use, but using the energy withdrawals as input data (in total one table)
		pop, TM 'country borders', US CB 'state borders'	Same steps as for water demand for industrial use (in total one field per year)
		GCAM (per region), MSWX, Huang et al. (2018) [Eq. (3)-(10)].	Temporal downscaling (month) to account for the withdrawal fluctuations between the warmest and coldest months based on Huang et al. (2018) Eq. (3)-(10) (in total 12 fields per year)
Water demand for livestock use (*liv*)	Daily supply of water volume for domestic animal needs	AQUASTAT (per country), USGS NWIS (per US State), GCAM (per region), GLW3, TM 'country borders'	Unit conversion from native to km³/year; NoData filling (year; in total one table): • regional data – spatial downscaling from regional withdrawals to country values (i.e. weighting by total livestock mass estimates per country from GLW3, $livestock_{year}^{country}$): $demand_{year}^{country} = \frac{withdrawal_{year}^{region}}{livestock_{year}^{region}} \cdot livestock_{year}^{country}$, then value linear interpolation (between years) and nearest neighbour extrapolation, finally rescaled with country data (if available) • for US States data – with linear interpolation (between years) and nearest neighbour extrapolation;

			• mosaicking results from US States and regional data, if not – with zero
	GLW3, TM 'country borders', US CB 'state borders'		Transforming from water demand per country/ US State to per grid cell (i.e. weighting by $\frac{livestockDensity_{year}^{grid}}{livestockDensity_{year}^{country}}$; in total one field per year): $demand_{year}^{grid} = \frac{demand_{year}^{country}}{livestockDensity_{year}^{country}} \cdot livestockDensity_{year}^{grid}$; Temporal downscaling (day; in total one field per year): $demand_{day,year}^{grid} = \frac{demand_{year}^{grid}}{day_{year}^{number}}$, where day_{year}^{number} is number of days in a year

To the best of the authors' knowledge, no other publicly accessible temporally varying global water demand field set exists (only static datasets). A rigorous validation of the temporally varying water demand fields is not straightforward at the global scale, as the only comprehensive global data source, FAO AQUASTAT, was used to create the fields.

8.3 Regional examples

In general fields in water demand category are easy to interpret as they show how much water per day is needed to satisfy certain type of human induced needs. In reality water demand fields are mainly covering urbanised areas and are scattered around (i.e. not continuously looking field), with relatively small variations in field values from month to month. Example for domestic water use is presented for August 2018 in Figure 20 for Po River area in 1 ~~are min~~ and 3 ~~are min~~arcminute resolution, and in Figure 21 for Amazon River and Brahmaputra River areas at 3 ~~are min~~arcminute resolution.
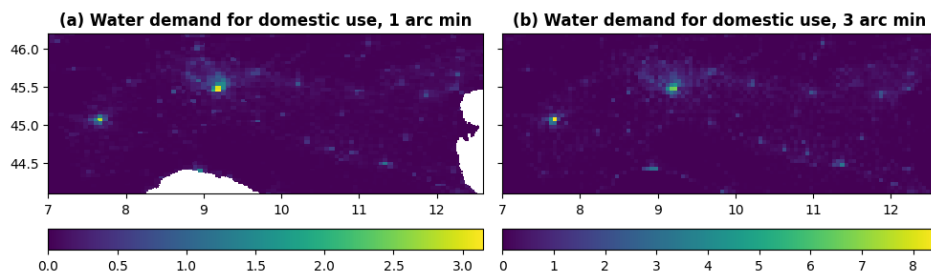
Figure 20. Water demand for domestic use in mm per day at 1 ~~are min~~arcminute (~1.9 km at the equator, left column, plot a) and 3 ~~are min~~arcminute (~5.6 km at the equator, right column, plot b) resolution for Po River area in Italy.
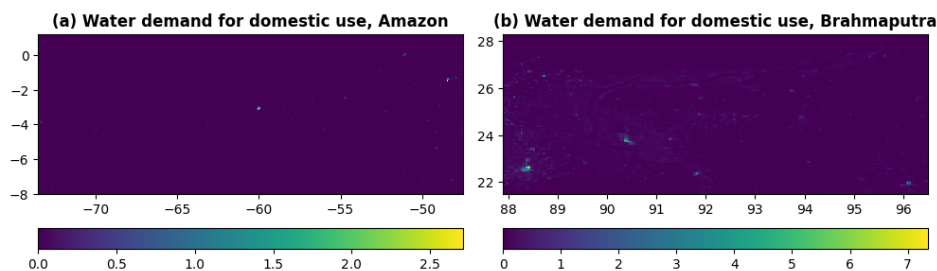
Figure 21. Water demand for domestic use in mm per day at 3 ~~are min~~arcminute (~5.6 km at the equator) resolution for Amazon River area (left column, plot a) and Brahmaputra River area (right column, plot b).

9 Data, access, licensing, documentation

The new CEMS_SurfaceFields_2022 is an open-source dataset of the Copernicus Emergency Management Service describing key components of the Earth surface generally required in environmental and hydrological modelling, including Earth system modelling and numerical weather prediction. The dataset includes static fields (e.g. forest fraction), yearly cycle fields (e.g. 10-day average LAI, in total 36 fields), and yearly varying fields (e.g. water demand). The surface fields are based on 25 different sources, including global and regional high resolution (up to 100 m) gridded and vector datasets. They were processed into two set of fields (i) at 1 ~~are min~~arcminute resolution (~1.86 km at the equator) over Europe (72.25 N/ 22.75 N, 25.25 W/ 50.25 E; 4530x2970 grid cells), and (ii) at 3 ~~are min~~arcminute resolution (~5.57 km at the equator) over the Globe (90.00 N/ 90.00 S,

668 180.00 W/ 180.00 E; 7200x3600 grid cells), to provide an up-to-date surface state for six main field groups: (1)
669 catchment morphology and river network, (2) land use fields, (3) vegetation properties, (4) soil properties, (5)
670 lakes, (6) water demand.
671 The CEMS_SurfaceFields_2022 dataset consist in total of 140 gridded fields at EPSG:4326 – WGS84: World
672 Geodetic System projection in NetCDF format with information on Earth's surface state (see Table 9 for the full
673 list of fields), which are grouped thematically in sub-folders. The 1 ~~are min~~arcminute European fields have a total
674 volume of 9.3 GB and the 3 ~~are min~~arcminute global fields have a total volume of 22.7 GB. The
675 CEMS_SurfaceFields_2022 dataset is freely available for download from the Joint Research Centre (JRC) Data
676 Catalogue (https://data.jrc.ec.europa.eu/). The set of global surface fields at 3 ~~are min~~arcminute resolution can be
677 found here (JRC Data Catalogue – LISFLOOD static and parameter maps for GloFAS – European Commission
678 (europa.eu), https://data.jrc.ec.europa.eu/dataset/68050d73-9c06-499c-a441-dc5053cb0c86) and the set of
679 surface fields for the European domain at 1 ~~are min~~arcminute resolution can be found here (JRC Data Catalogue
680 – LISFLOOD static and parameter maps for Europe – European Commission (europa.eu),
681 https://data.jrc.ec.europa.eu/dataset/f572c443-7466-4adf-87aa-c0847a169f23). The README.txt file that can be
682 found there contains the basic description of each surface fields including general information, data description,
683 file overview, methodological information and data access and sharing information ~~(for~~. For detailed technical
684 description of how the surface fields were generated refer to the LISFLOOD User Guide, available online:
685 https://ec-jrc.github.io/lisflood-code/4_Static-Maps-introduction~~)~~./. The changelog.txt file – provides users with
686 information on updates to the datasets. The copyright.txt file – information about the data license (CC BY 4.0).
687
688 **Table 9. Full list of surface fields with short description and units included in CEMS_SurfaceFields_2022 dataset; name**
689 **in italics ~~correspond~~corresponds to the field's file name in the data repository.**

Field group	Description	Name	Units
Main	model's field (i.e. in technical for model operation/ running sense)	*mask*	dimensionless
Catchment morphology and river network	local drainage direction (i.e. flow direction from one cell to another)	*LDD*	dimensionless
	grid cell area	*pixarea*	m^2
	grid cell length	*pixlength*	m
	upstream drainage area	*upArea*	m^2
	standard deviation of elevation	*elvstd*	m
	gradient	*gradient*	m/m
	channel bottom width	*chanbw*	m
	channel length	*chanlenght*	m
	channel gradient	*changrad*	m/m
	Manning's roughness coefficient for channels	*chanman*	$s/m^{1/3}$
	channel mask (i.e. presence of river channel)	*chan*	dimensionless
	channel side slope (i.e. channel's horizontal distance divided by vertical distance)	*chans*	m/m
	bankfull channel depth	*chanbnkf*	m
	channel floodplain (i.e. width of the area where the surplus of water is distributed when the water level in the channel exceed the channel depth)	*chanflpn*	m
Land use fields	fraction of forest	*fracforest*	dimensionless
	fraction of sealed surface	*fracsealed*	dimensionless
	fraction of inland water	*fracwater*	dimensionless
	fraction of irrigated crops	*fracirrigated*	dimensionless
	fraction of rice	*fracrice*	dimensionless
	fraction of other cover types	*fracother*	dimensionless
Vegetation properties (for forest [f], irrigated crops [i], other land cover types [o])	crop coefficient	*cropcoef_f, cropcoef_i, cropcoef_o*	dimensionless
	crop group number	*cropgrpn_f, cropgrpn_i, cropgrpn_o*	dimensionless
	Manning's surface roughness coefficient	*mannings_f, mannings_o,*	$s/m^{1/3}$
	rice planting days (3 seasons)	*riceplantingday1, riceplantingday2, riceplantingday3*	calendar day number
	rice harvesting days (3 seasons)	*riceharvestday1, riceharvestday2, riceharvestday3*	calendar day number
	leaf area index	*laif, laii, laio*	m^2/m^2
Soil properties (for [1, 2,	surface layer depth	*soildepth1_f, soildepth1_o*	mm
	middle layer depth	*soildepth2_f, soildepth2_o,*	mm
	subsoil depth	*soildepth3_f, soildepth3_o*	mm

3] layers; for forest [f], non-forest [o])	saturated volumetric soil moisture content	*thetas1_f, thetas1_o, thetas2_f, thetas2_o, thetas3*	m³/m³
	residual volumetric soil moisture content	*thetar1, thetar2, thetar3*	m³/m³
	pore size index	*lambda1_f, lambda1_o, lambda2_f, lambda2_o, lambda3*	dimensionless
	Van Genuchten equation parameter	*genua1_f, genua1_o, genua2_f, genua2_o, genua3*	cm⁻¹
	saturated soil conductivity	*ksat1_f, ksat1_o, ksat2_f, ksat2_o, ksat3*	mm/day
Lakes	lake mask (i.e. presence of lakes)	*lakemask*	dimensionless
Water demand	livestock	*liv*	mm/day
	industry	*ind*	mm/day
	thermoelectric production	*ene*	mm/day
	domestic use	*dom*	mm/day

690
691 Whilst the CEMS_SurfaceFields_2022 dataset followed strict requirements of the LISFLOOD-OS model (e.g.
692 format, treatment of missing values, number of soil layers, etc…) it definitely can be used outside the LISFLOOD
693 context, using the full dataset or its parts, for applications such as modelling risk assessment. The workflow and
694 methodology used to generate the dataset and published in this manuscript can be used as reference and be easily
695 modified if further adaptation to the dataset is needed (e.g. using different set of equations to describe the soil
696 properties, or sourcing new/ more relevant local datasets).

697 **10   Conclusion**

698 The Earth's surface has a strong impact on the surface energy and water balance that drives lower atmosphere
699 weather conditions and river discharge fluctuations. Depending on the surface type (e.g. land use, terrain or soil),
700 weather in the region can be colder/ warmer, more/ less humid, drier/ rainier, and/ or calmer/ windier than its
701 surroundings, and. Depending on the surface type also the terrestrial water cycle can differ, with water infiltrating
702 more/ less in the soil, leaving as evaporation in a larger/ smaller rate, and reaching rivers faster/ slower. Surface
703 information is provided by land use and ecosystem type (e.g., forest, rice paddy, bare ground, urban), river
704 geometry (e.g., channel width, channel length), soil properties (e.g., depth, porosity, hydraulic properties),
705 amongst others.
706 Information of underlying surface fields can be accounted for in Earth system and environmental models (e.g.
707 atmospheric, hydrological, etc.) to simulate the evolution in space and time of water, energy and carbon cycles. If
708 artificial influences and human intervention are included within the modelled processes (e.g. irrigation or water
709 management through reservoirs), the information required to describe the processes must also be integrated within
710 the modelling framework. Generally, this is achieved through a set of independent files used as input to the models.
711 Because of the temporal non-stationarity of some surface fields, typically associated with human intervention such
712 as land use and water use, but also due to climatic variation such as lake extent (new lakes forming or lakes
713 shrinking), input surface fields must be as representative as possible to the simulated period of interest. For
714 medium-range forecasting systems, this should be as close from present as possible, for example. When simulating
715 long periods, especially looking at past or future decades, caution must be given to results especially. Especially,
716 if some surface fields which have substantially changed during the simulation period do not explicitly incorporate
717 time and instead are based on the most recent period, as they. Most recent period may not be representative to the
718 full study period and can introduce substantial biases that grow with time. Same is applicable if surface fields are
719 used for collecting statistical data in general, as stats based on stationary fields represent only the period used to
720 generate stationary field in question.
721 In addition, in recent years the horizontal resolution of global Earth system and environmental models has been
722 constantly increasing reaching the kilometre scale milestone,. This has been supported by the technological
723 developments in the field of High Performance Computers and the wealth of high resolution datasets freely
724 available. This imposes another condition to the input surface fields – it has tofields must be of rather high
725 horizontal resolution (i.e. ~2 and 6 km at the equator).
726 Thanks to the availability of a wide range of high resolution environmental data derived from the use of ground,
727 unconventional and satellite measurement sensors, new high resolution datasets describing the Earth's surface are
728 nowadays released regularly. Even though each dataset may have a very low absolute and root mean square errors
729 compared against available independent data, merging different datasets for modelling purposes (e.g. to model
730 hydrological surface parameters) might lead to questionable results and even model crash, due to possible
731 discontinuity or inconsistency in the combined datasets. In the specific case of hydrological modelling where river
732 flow is also represented, high horizontal resolution does not guarantee better modelling per se. Sources of
733 potentially large errors can be easily hidden in high resolution datasets. This is the case for instance of errors in

the Digital Elevation Models when they are used to obtain the rivers drainage network. Small errors in the elevation of a grid cell can lead to a totally inaccurate representation of the location and the direction in which the river is flowing in the model compared to reality. Mislocating a river or having a slightly inaccurate catchment area can represent a trivial inaccuracy for most applications, but it can also lead to missed flood warning for thousands of people within a flood awareness system. To benefit from different recent high resolution datasets based on satellite and ground measurements, it is essential that a well-defined, thorough workflow is designed and implemented so that the final products are consistent and compatible with each other, and can be used in combination.

The work presented in this manuscript is focused not only on the final surface field set generation (i.e. CEMS_SurfaceFields_2022), but also on deriving robust reproducible methodology that could be re-applied once new versions of 25 or less input sources are released. Understanding of the methodology applied helps to interpret values in the final surface fields and possibly even numerical model results that use these surface fields. The collection of input sources and their preparation for actual use is a very important step as it includes going through all technical documentation, comparison and verification of papers, and investigation of the actual data, as well as data gridding, interpolation, and scaling. All input sources for CEMS_SurfaceFields_2022 are ranked according to their quality and up-to-date in order to favour one value in ambiguous situations when several datasets provide different information for the same location. Consistency check between all surface type fractions is carried out to address that ambiguity during the merge of information of different origin (i.e. adjust fractions to sum to one in each grid cell). Some fields, like forest fraction, were rather straightforward to create from available source, yet it was noted that prior correction of the source was needed to delete erroneous forest grid cells from the Fox Basin in Canada (the mismatch was only spotted during the investigation of the actual data, as it was absent from the documentation). Other fields, like soil hydraulic properties, are created not only from the source information but also from the forest fraction that had to be generated prior, the. The soil hydraulic property methodology also includes several steps that have to be performed at the data native resolution (i.e. 250 m) using information from several global fields simultaneously which becomes technically and computationally challenging. Surface fields with clear multi-annual changes, like water demand maps, are created using temporal interpolation and extrapolation from multiple data sources to create time series fields. A final and non-trivial task is to have all resulting fields on the identical required grid without deterioration of the actual value precision, even after several file type translations (e.g. local drainage direction field can be automatically checked and corrected if needed for required boundaries only in PCRaster format, not NetCDF). Due to the number of data sources and surface fields required to represent the main variables (i.e. 70) used in Earth system and environmental models, the overall effort to generate the CEMS_SurfaceFields_2022 dataset (both human and computing resources) was substantial.

The CEMS_SurfaceFields_2022 dataset is a new data source open to all offering a kilometre-scale resolution of high-quality data describing the Earth's surface (openly available online from the data catalogue of the JRC for Europe at ~1.9 km at the equator or 1 arc-min resolution: https://data.jrc.ec.europa.eu/dataset/f572c443-7466-4adf-87aa-c0847a169f23, and for Globe at ~5.6 km at the equator or 3 arc-min resolution: https://data.jrc.ec.europa.eu/dataset/68050d73-9c06-499c-a441-dc5053cb0c86, last accessed: 21.01.2024), providing exceptional opportunity for the research and scientific community to extend and multiply European and global applications in wide ranging fields of the water-energy-food nexus. The CEMS_SurfaceFields_2022 surface fields use can be vast, e.g. standardhere are only few of them. Standard deviation of elevation and other orographic sub-grid parameters are critical for radiation parametrization, especially for shadowing effect; channel. Channel geometry fields are vital to describe overbank inundation and infer inundated areas in wetland methane and soil carbon modelling; land. Land use fractions are needed for skin temperature calculations, biogenic flux calculations, urban planning, and climate mitigation plan preparation;. LAI use include biomass allocation, which can be used for fire danger forecasting, and carbon stock monitoring, whilst rice. Rice planting/ harvesting days are important for yearly cycle of methane modelling; soil. Soil properties are used for soil moisture calculations; and the. The area covered by lakes can be used for computing evaporation from open water, freshwater storage, unregulated surface water extent, fresh water scarcity indexes, and biogenic green house gas emission, as well as for reproducing different climate mitigation scenarios. All of the above state that CEMS_SurfaceFields_2022 surface fields can be used for weather prediction, Earth system modelling, hydrological and environmental modelling, or statistical analysis in general, with a spatial scale allowing for global, regional and even national applications.

Data availability. The CEMS_SurfaceFields_2022 datasets are freely available for download from the JRC Data Catalogue – global at ~5.6 km at the equator or 3 arc minarcminute resolution: https://data.jrc.ec.europa.eu/dataset/68050d73-9c06-499c-a441-dc5053cb0c86), over Europe at ~1.9 km at the equator or 1 arc minarcminute resolution: https://data.jrc.ec.europa.eu/dataset/f572c443-7466-4adf-87aa-c0847a169f23, and are documented in this paper.

Author contributions. CP and PS shaped initial plan of the research; MC and FM executed initial plan; CM, SG and JD reviewed initial results and provided guidance in further research. MC, FM and CP prepared a first draft of the paper, which was adapted to its present state by contributions from CM, SG, JD, PS and HB.

Competing interests. The authors declare that they have no conflict of interest.

Acknowledgements. CEMS_SurfaceFields_2022 is a product and service of the Copernicus Emergency Management Service. Financial support for MC, FM, CM and CP was provided by contract 941462-IPR-2021. Authors thank two anonymous reviewers for their valuable comments and suggestions that helped to shape the manuscript to it's current state.

Financial support. This research has been supported by contract 941462-IPR-2021.

References

Alfieri, L., Lorini, V., Hirpa, F. A., Harrigan, S., Zsoter, E., Prudhomme, C., and Salamon, P.: A global streamflow reanalysis for 1980–2018. Journal of Hydrology X, 6, 100049, ISSN 2589-9155, https://doi.org/10.1016/j.hydroa.2019.100049, 2020. (Available online https://www.sciencedirect.com/science/article/pii/S2589915519300331, last accessed: 21.01.2024).

Allen, R. G., Pereira, L. S., Raes, D., and Smith, M.: FAO Irrigation and Drainage Paper No. 56: Crop Evapotranspiration (guidelines for computing crop water requirements), 1998. (Available online: https://www.researchgate.net/publication/284300773_FAO_Irrigation_and_drainage_paper_No_56, last accessed: 21.01.2024).

Balsamo, G.: Interactive lakes in the Integrated Forecasting System. ECMWF Newsletter No. 137 – Autumn 2013, pp. 30–34, https://doi.org/10.21957/rffv1gir, 2013. (Available online: https://www.ecmwf.int/en/elibrary/80145-interactive-lakes-integrated-forecasting-system, last accessed: 21.01.2024).

Bates, P. D. and De Roo, A. P. J.: A simple raster-based model for flood inundation simulation. Journal of hydrology, vol. 236, 1-2, pp. 54–77, ISSN 0022-1694, https://doi.org/10.1016/S0022-1694(00)00278-X, 2000. (Available online: https://www.sciencedirect.com/science/article/abs/pii/S002216940000278X, last accessed: 21.01.2024).

Beck, H. E., van Dijk, A. I. J. M., Larraondo, P. R., McVicar, T. R., Pan, M., Dutra, E., and Miralles, D. G.: MSWX: Global 3-Hourly 0.1° Bias-Corrected Meteorological Data Including Near-Real-Time Updates and Forecast Ensembles. Bulletin of the American Meteorological Society, 103(3), pp. E710-E732, https://doi.org/10.1175/BAMS-D-21-0145.1, 2022. (Available online: https://journals.ametsoc.org/view/journals/bams/103/3/BAMS-D-21-0145.1.xml, last accessed: 21.01.2024).

Belleza, G. A. C., Bierkens, M. F. P., and van Vliet M. T. H.: Sectoral water use responses to droughts and heatwaves: analyses from local to global scales for 1990–2019. Environ. Res. Lett., 18 (10), 104008, https://doi.org/10.1088/1748-9326/acf82e, 2023.

Best, M. J., Pryor, M., Clark, D. B., Rooney, G. G., Essery, R .L. H., Menard, C. B., Edwards, J. M., Hendry, M. A., Porson, A., Gedney, N., Mercado, L. M., Sitch, S., Blyth, E., Boucher, O., Cox, P. M., Grimmond, C. S. B., and Harding, R. J.: The Joint UK Land Environment Simulator (JULES), model description – Part 1: Energy and water fluxes. Geosci. Model Dev., 4, 677–699, https://doi.org/10.5194/gmd-4-677-2011, 2011. (Available online: www.geosci-model-dev.net/4/677/2011/, last accessed: 21.01.2024).

Bhardwaj, A.: Evaluation of Openly Accessible MERIT DEM for Vertical Accuracy in Different Topographic Regions of India. 39th INCA International Congress, Dehradun (India), vol. 39, pp. 239–245, 2021. (Available online: https://www.researchgate.net/publication/356726804_Evaluation_of_openly_Accessible_MERIT_DEM_for_vertical_accuracy_in_different_topographic_regions_of_India, last accessed: 21.01.2024).

Bonan, G., Levis, S., Sitch, S., Vertenstein, M., and Oleson, K.: A dynamic global vegetation model for use with climate models: Concepts and description of simulated vegetation dynamics. Global Change Biology, 9, pp. 1543–1566, https://doi.org/10.1046/j.1365-2486.2003.00681.x, 2003.

Brooks, R. H. and Corey, A. T.: Hydraulic properties of porous media. Hydrology paper No. 3, Colorado State Univ., Fort Collins, 1964.

Buchhorn, M., Smets, B., Bertels, L., De Roo, B., Lesiv, M., Tsendbazar, N.-E., Herold, M., and Fritz, S.: Copernicus Global Land Service: Land Cover 100m: collection 3: epoch 2015: Globe (V3.0.1) [Data set]. Zenodo, https://doi.org/10.5281/zenodo.3939038, 2020.

Buchhorn, M., Smets, B., Bertels, L., De Roo, B., Lesiv, M., Tsendbazar, N.-E., Li, L., and Tarko, A.: Copernicus Global Land Service: Land Cover 100m: version 3 Globe 2015-2019: Product User Manual (Dataset v3.0, doc issue 3.4). Zenodo, https://doi.org/10.5281/zenodo.4723921, 2021.

850 Burek, P., Van Der Knijff, J., and De Roo, A.: LISFLOOD – Distributed Water Balance and Flood Simulation
851 Model – Revised User Manual. Luxembourg: Publications Office of the European Union, JRC78917, 2013.
852 (Available online: https://publications.jrc.ec.europa.eu/repository/handle/JRC78917, last accessed: 21.01.2024).
853 Burek, P., Bianchi, A., and Gentile, A.: JRC Technical Report: A Pan-European Data Set for hydrological
854 modelling. Luxembourg: Publications Office of the European Union, 2014.
855 Büttner, G. and Kosztra, B.: CLC2018 Technical Guidelines, Environment Agency, Austria, 2017. (Available
856 online: https://land.copernicus.eu/en/technical-library/clc-2018-technical-guidelines/@@download/file, last
857 accessed: 21.01.2024).
858 Calvin, K., Patel, P., Clarke, L., Asrar, G., Bond-Lamberty, B., Cui, R. Y., Di Vittorio, A., Dorheim, K., Edmonds,
859 J., Hartin, C., Hejazi, M., Horowitz, R., Iyer, G., Kyle, P., Kim, S., Link, R., McJeon, H., Smith, S. J., Snyder, A.,
860 Waldhoff, S., and Wise, M.: GCAM v5.1: representing the linkages between energy, water, land, climate, and
861 economic systems. Geosci. Model Dev., 12, 677–698, https://doi.org/10.5194/gmd-12-677-2019, 2019.
862 Carver, G.: Ten years of OpenIFS at ECMWF. ECMWF Newsletter No. 170 – Winter 2021/22, pp. 6-7, 2022.
863 (Available online: https://www.ecmwf.int/en/newsletter/170/news/ten-years-openifs-ecmwf, last accessed:
864 21.01.2024).
865 Chai, L. T., Wong, C. J., James, D., Loh, H. Y., Liew, J. J. F., Wong, W. V. C., and Phua, M. H.: Vertical accuracy
866 comparison of multi-source Digital Elevation Model (DEM) with Airborne Light Detection and Ranging
867 (LiDAR). IOP Conf. Ser.: Earth Environ. Sci., 1053, 012025, 2022. (Available online:
868 https://iopscience.iop.org/article/10.1088/1755-1315/1053/1/012025/pdf, last accessed: 21.01.2024).
869 Clark, D. B., Mercado, L. M., Sitch, S., Jones, C. D., Gedney, N., Best, M. J., Pryor, M., Rooney, G. G., Essery,
870 R. L. H., Blyth, E., Boucher, O., Harding, R. J., Huntingford, C., and Cox, P. M.: The Joint UK Land Environment
871 Simulator (JULES), model description – Part 2: Carbon fluxes and vegetation dynamics. Geosci. Model Dev., 4,
872 701–722, https://doi.org/10.5194/gmd-4-701-2011, 2011. (Available online: www.geosci-model-
873 dev.net/4/701/2011/, last accessed: 21.01.2024).
874 De Roo, A. P. J., Van Der Knijff, J., Schmuck, G., and Bates, P.: A simple floodplain inundation model to assist
875 in floodplain management. New trends in water and environmental engineering for safety and life: Eco-compatible
876 solutions for aquatic environments, 1–10, Balkema, Rotterdam, The Netherlands, 2000.
877 De Roo, A., Odijk, M., Schmuck, G., Koster, E., and Lucieer, A.: Assessing the effects of land use changes on
878 floods in the Meuse and Oder catchment. Physics and Chemistry of the Earth, Part B: Hydrology, Oceans and
879 Atmosphere, vol. 26, 7-8, 593–599, Pergamon, 2001.
880 Defourny, P., Lamarche, C., Bontemps, S., De Maet, T., Van Bogaert, E., Moreau, I., Brockmann, C., Boettcher,
881 M., Kirches, G., Wevers, J., and Santoro, M.: Land Cover CCI PRODUCT USER GUIDE VERSION 2.0 Tech.
882 Rep. ESA, 2017. (Available online: https://maps.elie.ucl.ac.be/CCI/viewer/download/ESACCI-LC-Ph2-
883 PUGv2_2.0.pdf, last accessed: 21.01.2024).
884 Dolan, F., Lamontagne, J., Link, R., Hejazi, M., Reed, P., and Edmonds, J.: Evaluating the economic impact of
885 water scarcity in a changing world. Nat Commun 12, 1915, https://doi.org/10.1038/s41467-021-22194-0, 2021.
886 Eerola, K., Rontu, L., Kourzeneva, E., Kheyrollah Pour, H., and Duguay, C.: Impact of partly ice-free Lake
887 Ladoga on temperature and cloudiness in an anticyclonic winter situation – a case study using a limited area
888 model. Tellus A, 66, 23929, https://doi.org/10.3402/tellusa.v66.23929, 2014.
889 Florczyk, A. J., Corbane, C., Ehrlich, D., Freire, S., Kemper, T., Maffenini, L., Melchiorri, M., Pesaresi, M.,
890 Politis, P., Schiavina, M., Sabo, F., Zanchetta, L., European Commission, Joint Research Centre: GHSL Data
891 Package 2019 – Public release GHS P2019, EUR 29788 EN, Publications Office of the European Union,
892 Luxembourg, ISBN 978-92-76-13186-1, JRC 117104, https://data.europa.eu/doi/10.2760/290498, 2019.
893 Fredlund, D.G. and Xing, A.: Equations for the Soil-Water Characteristic Curve. Canadian Geotechnical Journal,
894 31, 521–532, http://dx.doi.org/10.1139/t94-061, 1994.
895 Freire, S., MacManus, K., Pesaresi, M., Doxsey-Whitfield, E., and Mills, J.: Development of new open and free
896 multi-temporal global population grids at 250 m resolution. Geospatial Data in a Changing World; Association of
897 Geographic Information Laboratories in Europe (AGILE), 2016.
898 Gardner, W. R.: Calculation of capillary conductivity from pressure plate outflow data. Soil Science Society
899 Proceeding, 20(3), pp. 317–320, https://doi.org/10.2136/sssaj1956.03615995002000030006x, 1956.
900 Google Earth Engine: Frequently Asked Questions (GEE: FAQ), 2023. (Available online:
901 https://earthengine.google.com/faq/, last accessed: 21.01.2024).
902 Gilbert, M., Nicolas, G., Cinardi, G., Van Boeckel, T. P., Vanwambeke, S. O., Wint, G. R. W., and Robinson, T.
903 P.: Global distribution data for cattle, buffaloes, horses, sheep, goats, pigs, chickens and ducks in 2010. Sci Data
904 5, 180227, https://doi.org/10.1038/sdata.2018.227, 2018.
905 Gorelick, N., Hancher, M., Dixon, M., Ilyushchenko, S., Thau, D., and Moore, R.: Google Earth Engine:
906 Planetary-scale geospatial analysis for everyone. Remote Sensing of Environment, vol. 202, pp. 18–27,
907 https://doi.org/10.1016/j.rse.2017.06.031, 2017. (Available online:
908 https://www.sciencedirect.com/science/article/pii/S0034425717302900, last accessed: 21.01.2024).

Grimaldi, S., Salamon, P., Disperati, J., Zsoter, E., Russo, C., Ramos, A., Carton De Wiart, C., Barnard, C., Hansford, E., Gomes, G., and Prudhomme, C.: River discharge and related historical data from the Global Flood Awareness System. v4.0. Copernicus Climate Change Service (C3S) Climate Data Store (CDS) [Data set], https://doi.org/10.24381/cds.a4fdd6b9, 2022. (Available online: https://cds.climate.copernicus.eu/cdsapp#!/dataset/10.24381/cds.a4fdd6b9?tab=form, last accessed: 21.01.2024).

Gupta, S., Lehmann, P., Bonetti, S., Papritz, A., and Or, D.: Global prediction of soil saturated hydraulic conductivity using random forest in a Covariate-based GeoTransfer Function (CoGTF) framework. Journal of Advances in Modeling Earth Systems, 13(4), e2020MS002242, https://doi.org/10.1029/2020MS002242, 2021.

Harrigan, S., Zsoter, E., Cloke, H., Salamon, P., and Prudhomme, C.: Daily ensemble river discharge reforecasts and real-time forecasts from the operational Global Flood Awareness System. Hydrol. Earth Syst. Sci., 27, 1–19, https://doi.org/10.5194/hess-27-1-2023, 2023. (Available online: https://hess.copernicus.org/articles/27/1/2023/, last accessed: 21.01.2024).

Hejazi, M., Edmonds, J., Clarke, L., Kyle, P., Davies, E., Chaturvedi, V., Wise, M., Patel, P., Eom, J., Calvin, K., Moss, R., and Kim, S.: Long-term global water projections using six socioeconomic scenarios in an integrated assessment modeling framework. Technol. Forecast. Social Change, 81, pp. 205–226, https://doi.org/10.1016/j.techfore.2013.05.006, 2014. (Available online: https://www.sciencedirect.com/science/article/abs/pii/S0040162513001169, last accessed: 21.01.2024).

Hengl, T., de Jesus, J. M., MacMillan, R. A., Batjes, N. H., Heuvelink, G. B. M., Ribeiro, E., Samuel-Rosa, A., Kempen, B., Leenaars, J. G. B., Walsh, M. G., and Ruiperez Gonzalez, M.: SoilGrids1km – Global Soil Information Based on Automated Mapping. PLOS ONE 9(8): e105992, https://doi.org/10.1371/journal.pone.0105992, 2014.

Hengl, T., de Jesus, J. M., Heuvelink, G. B. M., Ruiperez Gonzalez, M., Kilibarda, M., Blagotić, A., Shangguan, W., Wright, M. N., Geng, X., Bauer-Marschallinger, B., Guevara, M. A., Vargas, R., MacMillan, R. A., Batjes, N. H., Leenaars, J. G. B., Ribeiro, E., Wheeler, I., Mantel, S., and Kempen, B.: SoilGrids250m: Global gridded soil information based on machine learning. PLOS ONE 12(2): 1–40, https://doi.org/10.1371/journal.pone.0169748, 2017.

Hirpa, F. A., Salamon, P., Beck, H. E., Lorini, V., Alfieri, L., Zsoter, E., and Dadson, S. J.: Calibration of the Global Flood Awareness System (GloFAS) using daily streamflow data. Journal of Hydrology, vol. 566, 595–606, https://doi.org/10.1016/j.jhydrol.2018.09.052, 2018.

Hodnett, M. G. and Tomasella, J.: Marked differences between van Genuchten soil water-retention parameters for temperate and tropical soils: a new water-retention pedo-transfer functions developed for tropical soils. Geoderma, vol. 108 (3-4), pp. 155–180, ISSN 0016-7061, https://doi.org/10.1016/S0016-7061(02)00105-2, 2002.

Huang, Z., Hejazi, M., Li, X., Tang, Q., Vernon, C., Leng, G., Liu, Y., Döll, P., Eisner, S., Gerten, D., Hanasaki, N., and Wada, Y.: Reconstruction of global gridded monthly sectoral water withdrawals for 1971–2010 and analysis of their spatiotemporal patterns. Hydrol. Earth Syst. Sci., 22, 2117–2133, https://doi.org/10.5194/hess-22-2117-2018, 2018.

Huijnen, V., Le Sager, P., Köhler, M. O., Carver, G., Rémy, S., Flemming, J., Chabrillat, S., Errera, Q., and van Noije, T.: OpenIFS/AC: atmospheric chemistry and aerosol in OpenIFS 43r3. Geosci. Model Dev., 15, 6221–6241, https://doi.org/10.5194/gmd-15-6221-2022, 2022.

International Food Policy Research Institute (IFPRI): Global Spatially-Disaggregated Crop Production Statistics Data for 2010 Version 2.0 [Data set]. Harvard Dataverse, https://doi.org/10.7910/DVN/PRFF8V, 2019. (Available online: https://dataverse.harvard.edu/dataset.xhtml?persistentId=doi:10.7910/DVN/PRFF8V, last accessed: 21.01.2024).

Intara, Y. I., Nusantara, A. D., Supanjani, Caniago, Z., and Ekawita, R.: Oil Palm Roots Architecture in Response to Soil Humidity. International Journal of Oil Palm Vol. 1, Nr. 2, ISSN: 2614-2376, 2018. (Available online: https://ijop.id/index.php/ijop/article/view/11/10, last accessed: 21.01.2024).

Karabulut, A., Egoh, B. N., Lanzanova, D., Grizzetti, B., Bidoglio, G., Pagliero, L., Bouraoui, F., Aloe, A., Reynaud, A., Maes, J., Vandecasteele, I., and Mubareka, S.: Mapping water provisioning services to support the ecosystem–water–food–energy nexus in the Danube river basin. Ecosystem Services, 17, 278–292, https://doi.org/10.1016/j.ecoser.2015.08.002, 2016. (Available online: https://www.sciencedirect.com/science/article/pii/S221204161530019X, last accessed: 21.01.2024).

Karssenberg, D., Schmitz, O., Salamon, P., de Jong, K., and Bierkens, M. F. P.: A software framework for construction of process-based stochastic spatio-temporal models and data assimilation. Environmental Modelling & Software, 25(4), pp. 489–502, https://doi.org/10.1016/j.envsoft.2009.10.004, 2010.

Kimpson, T., Choulga, M., Chantry, M., Balsamo, G., Boussetta, S., Dueben, P., and Palmer, T.: Deep learning for quality control of surface physiographic fields using satellite Earth observations. Hydrol. Earth Syst. Sci., 27(24), 4661–4685, https://doi.org/10.5194/hess-27-4661-2023, 2023.

Köhler, M. O., Hill, A. A., Huijnen, V., and Le Sager, P.: Enhancing OpenIFS by adding atmospheric composition capabilities. ECMWF Newsletter No. 175 – Spring 2023, pp. 27-31, http://doi.org/10.21957/np36mk1s9d, 2023.

968 (Available online: https://www.ecmwf.int/en/newsletter/175/earth-system-science/enhancing-openifs-adding-
969 atmospheric-composition, last accessed: 21.01.2024).
970 Kohli, A., Frenken, K., and Spottorno, C.: Disambiguation of water statistics. FAO AQUASTAT Report,
971 AQUASTAT Programme, FAO, pp. 1-6, 2012. (Available online: https://www.fao.org/3/bc816e/bc816e.pdf, last
972 accessed: 21.01.2024).
973 Laborte, A. G., Gutierrez, M. A., Balanza, J. G., Saito, K., Zwart, S. J., Boschetti, M., Murty, M. V. R., Villano,
974 L., Aunario, J. K., Reinke, R., Koo, J., Hijmans, R. J., and Nelson, A.: RiceAtlas, a spatial database of global rice
975 calendars and production [Data set]. Harvard Dataverse, V3, https://doi.org/10.7910/DVN/JE6R2R, 2017a.
976 Laborte, A. G., Gutierrez, M. A., Balanza, J. G., Saito, K., Zwart, S. J., Boschetti, M., Murty, M. V. R., Villano,
977 L., Aunario, J. K., Reinke, R., Koo, J., Hijmans, R. J., and Nelson, A.: RiceAtlas, a spatial database of global rice
978 calendars and production. Sci Data., 4:170074, PMID: 28556827, PMCID: PMC5448352,
979 https://doi.org/10.1038/sdata.2017.74, 2017b. (Available online:
980 https://www.ncbi.nlm.nih.gov/pmc/articles/PMC5448352/, last accessed: 21.01.2024).
981 Lawrence, D. M., Fisher, R. A., Koven, C. D., Oleson, K. W., Swenson, S. C., Bonan, G., Collier, N., Ghimire,
982 B., van Kampenhout, L., Kennedy, D., Kluzek, E., Lawrence, P. J., Li, F., Li, H., Lombardozzi, D., Riley, W. J.,
983 Sacks, W. J., Shi, M., Vertenstein, M., Wieder, W. R., Xu, C., Ali, A. A., Badger, A. M., Bisht, G., van den
984 Broeke, M., Brunke, M. A., Burns, S. P., Buzan, J., Clark, M., Craig, A., Dahlin, K., Drewniak, B., Fisher, J. B.,
985 Flanner, M., Fox, A. M., Gentine, P., Hoffman, F., Keppel-Aleks, G., Knox, R., Kumar, S., Lenaerts, J., Leung,
986 L. R., Lipscomb, W. H., Lu, Y., Pandey, A., Pelletier, J. D., Perket, J., Randerson, J. T., Ricciuto, D. M.,
987 Sanderson, B. M., Slater, A., Subin, Z. M., Tang, J., Thomas, R. Q., Val Martin, M., and Zeng, X.: The Community
988 Land Model version 5: Description of new features, benchmarking, and impact of forcing uncertainty. Journal of
989 Advances in Modeling Earth Systems, 11(12), pp. 4245-4287, https://doi.org/10.1029/2018MS001583, 2019.
990 Lehner, B. and Döll, P.: Development and validation of a global database of lakes, reservoirs and wetlands. Journal
991 of Hydrology, vol. 296(1-4), pp. 1–22, https://doi.org/10.1016/j.jhydrol.2004.03.028, 2004. (Available online:
992 http://dx.doi.org/10.1016/j.jhydrol.2004.03.028, last accessed: 21.01.2024).
993 Lv, S., Zeng, Y., Wen, J., Zhao, H., and Su, Z.: Estimation of Penetration Depth from Soil Effective Temperature
994 in Microwave Radiometry. Remote Sens., vol. 10(4), 519. https://doi.org/10.3390/rs10040519, 2018.
995 Marthews, T. R., Dadson, S. J., Clark, D. B., Blyth, E. M., Hayman, G. D., Yamazaki, D., Becher, O. R. E.,
996 Martinez-de la Torre, A., Prigent, C., and Jimenez, C.: Inundation prediction in tropical wetlands from JULES-
997 CaMa-Flood global land surface simulations. Hydrology and Earth System Sciences, vol. 26(12), 3151–3175,
998 https://doi.org/10.5194/hess-26-3151-2022, 2022. (Available online:
999 https://hess.copernicus.org/articles/26/3151/2022/, last accessed: 21.01.2024).
1000 Martínez-Sánchez, E.: Scientific Quality Evaluation of LAI/FAPAR/FCOVER Collection 1km Version 1 and
1001 Version 2 Issue I1.00, 2020. (Available online:
1002 https://land.copernicus.eu/global/sites/cgls.vito.be/files/products/CGLOPS1_SQE2019_LAI1km-
1003 V1%26V2_I1.00.pdf, last accessed: 21.01.2024).
1004 McManamay, R. A., KC, B., Allen-Dumas, M. R., Kao, S. C., Brelsford, C. M., Ruddell, B. L., Sanyal, J., Stewart,
1005 R. N., and Bhaduri, B. L.: Reanalysis of water withdrawal for irrigation, electric power, and public supply sectors
1006 in the conterminous United States, 1950–2016. Water Resources Research, 57(2), e2020WR027751,
1007 https://doi.org/10.1029/2020WR027751, 2021.
1008 Moiret-Guigand, A.: Copernicus Land monitoring services – CLC2018 / CLCC1218 VALIDATION REPORT,
1009 Issue 1.3, 2021 (Available online: https://land.copernicus.eu/en/technical-library/clc-2018-and-clc-change-2012-
1010 2018-validation-report/@@download/file, last accessed: 21.01.2024).
1011 Notaro, M., Holman, K., Zarrin, A., Fluck, E., Vavrus, S., and Bennington, V.: Influence of the Laurentian Great
1012 Lakes on Regional Climate. J. Climate, 26(3), pp. 789–804, https://doi.org/10.1175/JCLI-D-12-00140.1, 2013.
1013 O'Callaghan, J. F. and Mark, D. M.: The Extraction of Drainage Networks from Digital Elevation Data. Computer
1014 Vision, Graphics, and Image Processing, 28(3), pp. 323–344, https://doi.org/10.1016/S0734-189X(84)80011-0,
1015 1984.
1016 Pesaresi, M. and Politis, P.: GHS-BUILT-S R2022A - GHS built-up surface grid, derived from Sentinel2
1017 composite and Landsat, multitemporal (1975-2030) [Data set]. European Commission, Joint Research Centre
1018 (JRC), https://doi.org/10.2905/D07D81B4-7680-4D28-B896-583745C27085, 2022. (Available online:
1019 http://data.europa.eu/89h/d07d81b4-7680-4d28-b896-583745c27085, last accessed: 21.01.2024).
1020 Rosbjerg, D. and Madsen, H.: Concepts of hydrologic modeling. In Encyclopedia of Hydrological Sciences (eds
1021 M.G. Anderson and J.J. McDonnell), 10, 1–9, https://doi.org/10.1002/0470848944.hsa009, 2006.
1022 Samuelsson, P., Kourzeneva, E., and Mironov, D.: The impact of lakes on the European climate as simulated by
1023 a regional climate model. Boreal Environ. Res., 15(2), pp. 113–129, http://hdl.handle.net/10138/233079, 2010.
1024 (Available online: https://helda.helsinki.fi/server/api/core/bitstreams/feb9f8de-e831-4e9e-9ee6-
1025 07ac7df898eb/content, last accessed: 21.01.2024).
1026 Schiavina, M., Freire, S., and MacManus, K.: GHS-POP R2019A - GHS population grid multitemporal (1975,
1027 1990, 2000, 2015). European Commission, Joint Research Centre (JRC) [Data set],

https://doi.org/10.2905/0C6B9751-A71F-4062-830B-43C9F432370F, 2019. (Available online: https://data.jrc.ec.europa.eu/dataset/0c6b9751-a71f-4062-830b-43c9f432370f, last accessed: 21.01.2024).

Schiavina, M., Melchiorri, M., Pesaresi, M., Politis, P., Freire, S., Maffenini, L., Florio, P., Ehrlich, D., Goch, K., Tommasi, P., Kemper, T., European Commission, Joint Research Centre: GHSL Data Package 2022 – Public release GHS P2022, Publication Office of the European Union, JRC 129516, ISBN 978-92-76-53071-8, https://doi.org/10.2760/19817, 2022.

Smets, B.: Product User Manual of LAI/FAPAR/FCOVER Collection 1km Version 2 Issue 1.33, 2019. (Available online: https://land.copernicus.eu/global/sites/cgls.vito.be/files/products/CGLOPS1_PUM_LAI1km-V2_I1.33.pdf, last accessed: 21.01.2024).

Smith, P. J., Pappenberger, F., Wetterhall, F., Del Pozo, J. T., Krzeminski, B., Salamon, P., Muraro, D., Kalas, M., and Baugh, C.: On the operational implementation of the European Flood Awareness System (EFAS). Flood forecasting: A Global Perspective, Academic Press, pp. 313–348, https://doi.org/10.1016/B978-0-12-801884-2.00011-6, 2016.

Sparrow, S., Bowery, A., Carver, G. D., Köhler, M. O., Ollinaho, P., Pappenberger, F., Wallom, D., and Weisheimer, A.: OpenIFS@home version 1: a citizen science project for ensemble weather and climate forecasting. Geosci. Model Dev., 14(6), 3473–3486, https://doi.org/10.5194/gmd-14-3473-2021, 2021.

Supit, I., Hoojier, A. A., and Van Diepen, C. A.: System description of the Wofost 6.0 crop simulation model implemented in CGMS. Volume 1: Theory and Algorithms, 1994. (Available online: https://www.researchgate.net/publication/282287246_System_description_of_the_Wofost_60_crop_simulation_model_implemented_in_CGMS_Volume_1_Theory_and_Algorithms, last accessed: 21.01.2024).

Te Chow, V.: Open-channel Hydraulics. Civil engineering series (publisher McGraw-Hill Book Company Inc.), ISBN 07-010776-9, 1959. (Available online: https://heidarpour.iut.ac.ir/sites/heidarpour.iut.ac.ir/files/u32/open-chow.pdf, last accessed: 21.01.2024).

Tóth, B., Weynants, M., Nemes, A., Makó, A., Bilas, G., and Tóth, G.: New generation of hydraulic pedotransfer functions for Europe. Eur J Soil Sci, 66(1), pp. 226-238, https://doi.org/10.1111/ejss.12192, 2015.

Van Der Knijff, J. and De Roo, A.: LISFLOOD – Distributed Water Balance and Flood Simulation Model, Revised User Manual. EUR 22166 EN/2, Office for Official Publications of the European Communities, Luxembourg, 109 pp, 2008.

Van Der Knijff, J. M., Younis, J., and De Roo, A. P. J.: LISFLOOD: A GIS-based distributed model for river basin scale water balance and flood simulation. Int. J. Geogr. Inf. Sci., 24(2), 189–212, 2010.

van Genuchten, M. T.: A closed-form equation for predicting the hydraulic conductivity of unsaturated soils. Soil Sci. Soc. Am. J., 44, 892–898, 1980.

Vanham, D., Alfieri, L., Flörke, M., Grimaldi, S., Lorini, V., De Roo, A., and Feyen, L.: The number of people exposed to water stress in relation to how much water is reserved for the environment: a global modelling study. The Lancet Planetary Health, vol. 5(11), pp. e766–e774, https://doi.org/10.1016/S2542-5196(21)00234-5, 2021. (Available online: https://www.sciencedirect.com/science/article/pii/S2542519621002345, last accessed: 21.01.2024).

Vassolo, S. and Döll, P.: Global-scale gridded estimates of thermoelectric power and manufacturing water use. Water Resour. Res. 41(4), https://doi.org/10.1029/2004WR003360, 2005.

Vavrus, S., Notaro, M., and Zarrin, A.: The role of ice cover in heavy lake-effect snowstorms over the Great Lakes Basin as simulated by RegCM4. Mon. Weather Rev., 141, 148–165, 2013.

Voisin, N., Liu, L., Hejazi, M., Tesfa, T., Li, H., Huang, M., Liu, Y., and Leung, L. R.: One-way coupling of an integrated assessment model and a water resources model: evaluation and implications of future changes over the US Midwest. Hydrol. Earth Syst. Sci., 17(11), 4555–4575, https://doi.org/10.5194/hess-17-4555-2013, 2013.

Wada, Y., van Beek, L. P. H., Viviroli, D., Dürr, H. H., Weingartner, R., and Bierkens, M. F. P.: Global monthly water stress: 2. Water demand and severity of water stress. Water Resour. Res., 47(7), W07518, https://doi.org/10.1029/2010WR009792, 2011.

Yamazaki, D., Oki, T., and Kanae, S.: Deriving a global river network map and its sub-grid topographic characteristics from a fine-resolution flow direction map. Hydrol. Earth Syst. Sci., 13(11), 2241–2251, https://doi.org/10.5194/hess-13-2241-2009, 2009.

Yamazaki, D., Kanae, S., Kim, H., and Oki, T.: A physically based description of floodplain inundation dynamics in a global river routing model. Water Resour. Res., 47(4), W04501, https://doi.org/10.1029/2010WR009726, 2011.

Yamazaki, D., Ikeshima, D., Tawatari, R., Yamaguchi, T., O'Loughlin, F., Neal, J. C., Sampson, C. C., Kanae, S., and Bates, P. D.: A high-accuracy map of global terrain elevations. Geophys. Res. Lett., 44(11), pp. 5844–5853, https://doi.org/10.1002/2017GL072874, 2017.

Yamazaki, D., Ikeshima, D., Sosa, J., Bates, P. D., Allen, G. H., and Pavelsky, T. M.: MERIT Hydro: A high-resolution global hydrography map based on latest topography datasets. Water Resources Research, vol. 55(6), pp. 5053–5073, https://doi.org/10.1029/2019WR024873, 2019.

Yu, Q., You, L., Wood-Sichra, U., Ru, Y., Joglekar, A. K. B., Fritz, S., Xiong, W., Lu, M., Wu, W., and Yang, P.: A cultivated planet in 2010 – Part 2: The global gridded agricultural-production maps. Earth Syst. Sci. Data, 12(4), 3545–3572, https://doi.org/10.5194/essd-12-3545-2020, 2020.

Zhang, Y. and Schaap, M. G.: Estimation of saturated hydraulic conductivity with pedotransfer functions: A review. Journal of Hydrology, vol. 575, pp. 1011–1030, ISSN 0022-1694, https://doi.org/10.1016/j.jhydrol.2019.05.058, 2019.

Zhang, J., Liu, D., Guo, S., Xiong, L., Liu, P., Chen, J., and Yin, J.: High resolution annual irrigation water use maps in China based-on input variables selection and convolutional neural networks. Journal of Cleaner Production, 405, 136974, https://doi.org/10.1016/j.jclepro.2023.136974, 2023. (Available online: https://www.sciencedirect.com/science/article/pii/S0959652623011320, last accessed: 21.01.2024).

Appendix

Appendix 1

All data sources used to produce dataset's surface fields, mentioned in Sections 3 to 9, are described here. All data considered were open source, freely available, updated as recently as possible, with recognised reference on their quality.

1.1 Catchment morphology and river network

The MERIT DEM: Multi-Error-Removed Improved-Terrain Digital Elevation Model v.1.0.3 [15 October, 2018] (further referred as MERIT DEM) is a high accuracy global DEM at 3 arc second resolution (~90 m at the equator) covering land area from 90 N to 60 S, selected for its ability to clearly represent landscapes such as river networks and hill-valley structures even in flat areas where height errors could be larger than topography variability (Yamazaki et al., 2017; Bhardwaj, 2021; Chai et al., 2022). It is derived from seven different open-source datasets, delivered as 57 GeoTiff files 30º by 30º region each, at ~90 m resolution (in total 90.0 GB), representative of the year 2018. More detail on method, data content and access can be found in Yamazaki et al. (2017) and MERIT DEM web-page http://hydro.iis.u-tokyo.ac.jp/~yamadai/MERIT_DEM.
The MERIT DEM was used to compute standard deviation of elevation, gradient and channel geometry fields.

The Catchment-based Macro-scale Floodplain (CaMa-Flood) Global River Hydrodynamics Model v4.0 maps (further referred as CaMa-Flood) are used for the basic maps describing all physical properties of the river network. It is derived from MERIT Hydro (MERIT Hydro is a global hydrography dataset, created by using elevation (i.e. MERIT DEM) and several inland water maps; more detail can be found in Yamazaki et al. (2019) and MERIT Hydro web-page http://hydro.iis.u-tokyo.ac.jp/~yamadai/MERIT_Hydro) for high resolution river routing applications using the FLOW algorithm (Yamazaki et al., 2009; Yamazaki et al., 2011). The maps include information on channel length, river topography parameters, floodplain elevation profile, channel width and channel depth. The maps exist at 15, 6, 5, 3 and 1 ~~arc min~~arcminute resolutions covering land area from 90 N to 60 S, representative of the year 2017, and for each resolution, they are available as one single file with all variables in NetCDF format (for 1 ~~arc min~~arcminute 737.0 MB). More detail on method, data content and access can be found in Yamazaki et al. (2011) and CaMa-Flood web-page http://hydro.iis.u-tokyo.ac.jp/~yamadai/cama-flood/index.html. Note that whilst the CaMaFlood maps where originally generated for the specific use of the CaMa-Flood model, they can also serve as basic to derive alternative maps for other environmental models, as done here.
The CaMa-Flood maps were used to create the local drainage direction (LDD), upstream drainage area, channel geometry and land masks fields.

1.2 Land use fields

The Copernicus Global Land Service (CGLS) Land Cover (LC) 100m map (further referred as CGLS-LC100) is a global land cover map of the year 2015 (Buchhorn et al., 2020). It is derived from the PROBA-V 100 m satellite image collection, a database of high quality land cover training sites and ancillary datasets, reaching an accuracy of 80 % at Level1 (Buchhorn et al., 2021). It contains 23 classes for discrete classification and 10 classes for continuous cover fractions; and it is delivered as 15 files in GeoTiff format (in total 39.3 GB) at 100 m resolution covering land area from 90 N to 60 S and representative of the year 2015. More detail on method, data content and access can be found in Buchhorn et al. (2021) and Copernicus web-site https://land.copernicus.eu/global/products/lc.

1138 The CGLS-LC100 was used to generate crop parameters and Manning's surface roughness coefficient for forest
1139 and other land cover types, to generate forest, inland water, and sealed surface fraction fields, following a basic
1140 quality check on large water bodies (i.e. correcting Fox Basin and Caspian Sea).
1141

1142 **The Coordination of Information on the Environment (CORINE) Land Cover (CLC) inventory for 2018**
1143 (further referred as CLC2018) is a set of maps describing the land cover/ land use status of 2018 covering
1144 39 countries in Europe with a total area of over 5.8 Mkm^2. The dataset is derived from satellite imagery (mainly
1145 Sentinel-2, based on a constellation of two satellites orbiting Earth at altitude of 786 km 180° apart revisiting
1146 equator every 5 days, and for gap filling Landsat-8, making a constellation together with Landsat-9 satellite
1147 orbiting Earth at altitude of 705 km each revisiting equator every 16 days) and in-situ data and contains 44 classes,
1148 delivered as one GeoTiff raster file (125.0 MB) at 100m resolution covering land area over Europe, representative
1149 of the time period 2017-2018. The overall accuracy for CLC2018 is 92 % for the blind analysis (i.e. validation
1150 team had no knowledge of the CLC2018 thematic classes) but there are regional variations: the Black Sea
1151 geographical region has the lowest accuracy of 84 %; country-wise overall accuracy vary from 86 % for Portugal
1152 to 99 % for Iceland, lowest accuracy being linked to the landscape complexity (Moiret-Guigand, 2021). More
1153 detail on method, data content and access can be found in Büttner and Kosztra (2017) and Moiret-Guigand (2021),
1154 and Copernicus web-site https://land.copernicus.eu/pan-european/corine-land-cover/clc2018.
1155 The CLC2018 was used to generate the irrigated crop fraction and rice fraction fields.
1156

1157 **The Spatial Production Allocation Model (SPAM) – Global Spatially-Disaggregated Crop Production**
1158 **Statistics Data for 2010 v2.0** (further referred as SPAM2010) is a global dataset generated in 2020, which
1159 redistributes crop production information from country and sub-national provinces level to a finer grid cell level
1160 (IFPRI, 2019). It is derived from numerous data sources, including crop production statistics, cropland data,
1161 biophysical crop "suitability" assessments, spatial distribution of specific crops or crop systems, and population
1162 density. SPAM2010 contains estimates of crop distributions within disaggregated units (based on a cross-entropy
1163 approach) for 42 crops and two production systems (irrigated and rainfed), and is delivered as 84 files in shapefile
1164 format at 10 km (5 ~~are min~~arcminute) resolution covering land area from 90 N to 60 S and representative of the
1165 year 2010 (in total 2.2 GB). Based on crop expert judgement from international (i.e. International Rice Research
1166 Institute, International Maize and Wheat Improvement Center) and national organisations (i.e. The Chinese
1167 Academy of Agricultural Sciences) SPAM2010 over Europe and America is more accurate than over Africa and
1168 South East Asia, with best performance in allocating rice; grid-by-grid comparison of crop areas with independent
1169 Cropland Data Layer (produced by using satellite images and vast amount of ground truth) over continental United
1170 States shows coefficient of determination (R^2) 0.7-0.9 and root mean square error (RMSE) 231-307 ha indicating
1171 a relatively high reliability, with highest R^2 and lowest RMSE values are for maize and soybean (Yu et al., 2020).
1172 More detail on method, data content and access can be found in Yu et al. (2020) and MapSPAM web-site
1173 https://mapspam.info.
1174 SPAM2010 was used to compute the irrigated crop and rice fractions, crop parameters and Manning's surface
1175 roughness coefficient for irrigated crop fields.

1176 **1.3 Vegetation properties**

1177 **The Food and Agriculture Organisation (FAO) of the United Nations Irrigation and Drainage Paper No.**
1178 **56** (further referred as FAO56) is a publication covering geographically referenced statistics for crop development
1179 stages, crop coefficients, crop height, rooting depth, and soil water depletion fraction for common crops found
1180 across the world; it also covers procedures for information aggregation, e.g. on the grid. It is delivered as an article
1181 with a set of tables and equations and can be considered as the most complete source of information on crop
1182 properties. More detail on method and data content can be found in Allen et al. (1998) and FAO online crop
1183 information web-page http://www.fao.org/land-water/databases-and-software/crop-information/tobacco/en/.
1184 FAO56 was used to compute the crop coefficients for forest, irrigated crops and other land cover types (online
1185 crop information was specifically used for tobacco); and for intermediate computations such as depletion fraction
1186 for different crop and surface types (table), crop height and root depth fields.
1187

1188 **Intara** et al. (2018) is a publication covering oil palm roots architecture.
1189 Intara et al. (2018) was used for oil palm root depth information in addition to FAO56.
1190

1191 **Burek** et al. (2014) is a publication covering summarised information for crop coefficients, rooting depth, crop
1192 group number and Manning's surface roughness coefficient for different surface types.
1193 Burek et al. (2014) was used for built-up, bare/ sparse vegetation, snow & ice, permanent inland water, ocean &
1194 seas, herbaceous wetland, moss & lichen surface types crop coefficients, rooting depth, crop group number and
1195 Manning's surface roughness coefficient information in addition to FAO56 and other sources.

1196

1197 **The Wofost 6.0 crop simulation model description** (further referred as SUPIT) is a publication on developing,
1198 validating, and testing new or already existing agrometeorological models (Supit et al., 1994). It contains crop
1199 group information for several crops as examples, and relation of a crop group from water depletion fraction. The
1200 publication is delivered as a book with a set of tables and equations. Information on crop group is still considered
1201 up-to-date. More detail on method and data content can be found in Supit et al. (1994).
1202 SUPIT was used to compute the crop group fields for forest, irrigated crops and other land cover types.

1203

1204 **The Open-Channel Hydraulics manual** (further referred as CHOW) is a publication on open-channel
1205 hydraulics, including basic principles and different types of flows, i.e. uniform, gradually varied, rapidly varied,
1206 and unsteady (Te Chow, 1959). It contains information on roughness coefficient over different surfaces. The
1207 publication is delivered as a book with a set of tables and equations. More detail on method and data content can
1208 be found in Te Chow (1959).
1209 CHOW was used to compute the Manning's surface roughness coefficient fields for forest, irrigated crops and
1210 other land cover types.

1211

1212 **The Copernicus Global Land Service (CGLS) Leaf Area Index (LAI) 1km Version 2 collection** (further
1213 referred as CGLS-LAI) is a set of global maps without missing data describing vegetation dynamics – the annual
1214 evolution of LAI at 10-day intervals over the period of 1999-2020. The dataset is derived from
1215 SPOT/VEGETATION and PROBA-V data. The dataset's root mean square deviations over 20 GBOV sites over
1216 the period 2014-2018 is 0.92, compared to 1.19 for MODIS C6 LAI product (Martinez-Sanchez, 2020). The
1217 dataset is delivered as one multi-band file per year in NetCDF (netCDF4 CF-1.6) format (14.7 GB per year) at 1
1218 km resolution covering land area from 90 N to 60 S and representative of the 10-year period of 2010-2019. More
1219 detail on method, data content and access can be found in Smets (2019) and Martinez-Sanchez (2020), and
1220 Copernicus web-site https://land.copernicus.eu/global/products/lai.
1221 CGLS-LAI was used to compute the LAI fields for forest, irrigated crops and other land cover types.

1222

1223 **The RiceAtlas v3** (further referred as RiceAtlas) is a spatial database of global rice calendars and production. It
1224 contains information on start, peak and end dates of sowing, transporting and harvesting rice, derived from global
1225 and regional databases, national publications, online reports, and expert knowledge. It is delivered as 7 files in
1226 shapefile format (in total 195.8 MB) for administrative units (in total 2725 spatial units) at 1 km resolution for the
1227 national production totals to match the years 2010-2012 (Laborte et al., 2017a). RiceAtlas is ~10 times more
1228 spatially detailed, and has ~7 times more special units comparing with other global datasets (Laborte et al., 2017b).
1229 More detail on method, data content and access can be found in Laborte et al. (2017a) and Laborte et al. (2017b).
1230 RiceAtlas was used to compute rice planting and rice harvesting days for three different seasons.

1231 **1.4 Soil properties**

1232 **The International Soil Reference and Information Centre (ISRIC) SoilGrids250m global gridded soil**
1233 **information release 2017** (further referred as SoilGrids250m) is an output of special predictions produced by the
1234 SoilGrids system, as a set of global soil property and class maps at 250 m resolution. It is derived from soil profile
1235 data (from ~150,000 sites globally) with the use of machine learning, and contains information on soil
1236 characteristics at six standard depths, including soil textures (clay, silt, sand), depth to bedrock, bulk density,
1237 organic carbon, pH and cation exchange capacity. It is delivered as 43 files in GeoTiff format (in total 111.8 GB)
1238 at 250 meters resolution covering land area with no permanent ice and representative for the year 2010 (according
1239 to land cover) (Hengl et al., 2017). SoilGrids250m pH comparison with SSURGO data over California (depth 0-
1240 200 cm) and Soil and Landscape Grid of Australia data over Tasmania (depth 0-5 cm) show high correlation, 0.79
1241 and 0.71 respectively (Hengl et al., 2017). Despite its limited accuracy (i.e. between 30 and 70 %, according to
1242 the SoilGrids web-site) due to the scarcity of soil profile observations (especially in Central Asia, Artic regions
1243 costal area and desert), low resolution of covariates data and algorithms, it was selected as the most recent source
1244 of information. More detail on method, data content and access can be found in Hengl et al. (2017) and
1245 SoilGrids250m web-site https://www.isric.org/explore/soilgrids/faq-soilgrids-2017.
1246 SoilGrids250m was used to compute the soil depth and soil hydraulic properties for forest and non-forest.

1247 **1.5 Lakes**

1248 **The Global Lakes and Wetlands Database** (further referred as GLWD) is a global database of water bodies. It
1249 is derived from a combination of global and regional lake data sets, registers and inventories (i.e. point information
1250 with descriptive attributes), and digital maps (i.e. polygons, rasterised global land cover and land use maps). The
1251 database consists of two global files in shapefile format at spatial resolutions of up to 1:1 million – GLWD-1 with

1252 3067 largest lake and 654 largest reservoir polygons (6.4 MB), and GLWD-2 with ~250000 smaller lake and
1253 reservoir polygons (32.0 MB); and of one global file in ADF raster format at 30 arc sec resolution – GLWD-3
1254 combines GLWD-1, GLWD-2 and additional information (8.9 MB). Validation against documented data shows
1255 that GLWD represents good wetland maximum extent, and describes comprehensively lakes with surface area
1256 greater or equal 1 km^2 (Lehner and Döll, 2004). More detail on method, data content and access can be found in
1257 Lehner and Döll (2004) and GLWD web-site https://www.worldwildlife.org/pages/global-lakes-and-wetlands-
1258 database.
1259 GLWD (i.e. only GLWD-1 and GLWD-2) was used to compute the discrete lake mask field.

1260 **1.6 Water demand**

1261 **AQUASTAT** is the FAO's global information system on water resources and agricultural water management.
1262 AQUASTAT collects information on water use via the network of AQUASTAT National Correspondents who
1263 are required to fill the annual questionnaire and collaborate with AQUASTAT team in the data validation process.
1264 Five types of manual checks are followed by automatic implementation of almost 200 validation rules. The dataset
1265 includes data for 180 countries worldwide, yearly data from 1979 to 2019 were used to produce the maps presented
1266 by this manuscript. Float, lumped values for each country for the variables "Gross Domestic Product (GDP)",
1267 "Industry, value added to GDP", "Agricultural water withdrawal", "Industrial water withdrawal", "Municipal
1268 water withdrawal", "Total water withdrawal", and "Irrigation water withdrawal" were obtained in CSV format (2
1269 files, in total 2.0 MB) from the AQUASTAT data acquisition dashboard
1270 (https://tableau.apps.fao.org/views/ReviewDashboard-v1/country_dashboard). More detail on method, data
1271 content and access can be found in AQUASTAT web-site
1272 https://www.fao.org/aquastat/en/overview/methodology/.
1273 AQUASTAT variables were used accordingly to compute water demand fields for domestic, industrial, energy,
1274 livestock use.
1275
1276 **United States Geological Survey National Water Information System** (further referred as USGS NWIS) is a
1277 national database on water use data for the United States (US) with annual statistics provided every 5 years since
1278 1950. The water use data are best estimates produced by the USGS in cooperation with local, state, and federal
1279 agencies as well as academic and private organisations. The water use data are lumped values (float numbers) for
1280 each state, delivered in plain text format (52 files, in total 56.0 MB). Following variables were used: "Domestic
1281 total self-supplied withdrawals, fresh, in Mgal/d", "Public Supply total self-supplied withdrawals, fresh, in
1282 Mgal/d", "Industrial total self-supplied withdrawals, fresh, in Mgal/d", "Total Thermoelectric Power total self-
1283 supplied withdrawals, fresh, in Mgal/d", "Total Thermoelectric Power power generated, in gigawatt-hours", and
1284 "Livestock total self-supplied withdrawals, fresh, in Mgal/d". More detail on method, data content and access can
1285 be found in USGS NWIS web-site https://waterdata.usgs.gov/nv/nwis/wu. For this study, data from 1985 to 2015
1286 were used.
1287 USGS NWIS variables were used accordingly to refine the global water demand fields for the domestic, industrial,
1288 energy, livestock use sectors for the US.
1289
1290 **Global Change Analysis Model** (further referred as GCAM) is an integrated, multi-sector model developed by
1291 the Joint Global Change Research Institute (JGCRI) to explore the overall behaviour of human and physical
1292 systems dynamics and interactions. GCAM includes five main systems. One of these systems, the water module,
1293 provides information about water withdrawals for energy, agriculture, and municipal uses as lumped values of
1294 235 hydrologic basins; a detailed explanation can be found in Calvin et al. (2019). Estimates of industrial,
1295 thermoelectric water withdrawals (energy sector) and electricity consumption were computed by running the
1296 GCAM model, the output used are two files in CSV format (in total 4.0 MB). Data from the following sectors was
1297 used: "biomass", "electricity", "nuclearFuelGenII", "nuclearFuelGenIII", "regional coal", "regional natural gas",
1298 "regional oil", "SheepGoat", "Beef", "Dairy", "Pork", and "Poultry". More detail on method, data content and
1299 access can be found in the documentation of the open source package https://github.com/JGCRI/gcam-
1300 core/tree/gcam-v6.0.
1301 GCAM variables were used accordingly to estimate water withdrawals for industrial, energy, livestock use.
1302
1303 **Global-scale gridded estimates of thermoelectric power and manufacturing water use** (further referred as
1304 Vassolo and Doll, 2005) is a global-scale gridded estimate of water withdrawal for cooling of thermal power
1305 stations and for manufacturing. Estimates of values for the year 1995 are provided with a spatial resolution of 0.5°
1306 by 0.5°. Thermoelectric power water use is based on the geographical location of 63590 thermal power stations.
1307 Manufacturing water use is computed by estimating country-specific water withdrawal values, and spatial
1308 downscaling using city night-time lights. Dataset verification of Vassolo and Doll (2005) showed satisfactory
1309 representation of thermoelectric power water use but high uncertainty in the representation of manufacturing water

1310 use. The data are delivered as one shapefile (2.5 MB). More details on method, data content and validation, and
1311 data access can be found in Vassolo and Doll (2005).
1312 Vassolo and Doll (2005) dataset was used for the computation of energy demand fields.
1313

1314 **The Gridded Livestock of the World (GLW) version3** (further referred as GLW3) is a spatial gridded dataset
1315 of the global distribution of eight livestock species for 2010. It is delivered as 8 GeoTiff files at 0.083333° (~10
1316 km at the equator) resolution (in total 208.0 MB). The species abundance was converted to total livestock mass.
1317 More detail on method, data content and access can be found in Gilbert et al. (2018).
1318 GLW3 was used to spatially disaggregate the water demand for livestock use.
1319

1320 **World Bank manufacturing value added and gross domestic product** (further referred as World Bank) data
1321 provide "Manufacturing, value added (constant 2015 US$)" values (further referred as MVA) and "Gross
1322 Domestic Product GDP (constant 2015 US$)" values. The data provided as a table, downloaded in CSV format
1323 (6 files, in total 6.0 MB) from https://data.worldbank.org.
1324 World Bank dataset was used to temporally downscale the values of water demand fields for the industrial and
1325 energy sectors.
1326

1327 **The Global Human Settlement Population Grid multitemporal version R2019A** (further referred as GHS-
1328 POP) is a spatial raster dataset that depicts the distribution of population, expressed as the number of people per
1329 grid cell (Freire et al., 2016; Florczyk et al., 2019; Schiavina et al., 2019). GHS-POP residential population
1330 estimates for target years provided by CIESIN GPWv4.10 were disaggregated from census or administrative units
1331 to grid cells, informed by the distribution and density of built-up as mapped in the Global Human Settlement
1332 Layer. The dataset has a spatial resolution of 9 arc sec (~300 m at the equator) resolution and is delivered as
1333 individual files in GeoTiff format for 1975, 1990, 2000 and 2015 (4 files, in total 6.5 GB; available online:
1334 https://ghsl.jrc.ec.europa.eu/ghs_pop2019.php, last accessed: 21.01.2024).
1335 GHS-POP was used to spatially disaggregate the country, state, basin-level information of domestic, industrial,
1336 energy water withdrawal.
1337

1338 **Thematic Mapping Country Borders** shapefile (further referred as TM 'country borders') was derived from
1339 Thematic Mapping ™, which is a tool enabling web browsers to create thematic maps and associated world
1340 datasets. For this work, the TM World Borders Dataset was downloaded as one shapefile (10.0 MB). **The United
1341 States Census Bureau** Cartographic Boundary Files – Shapefile (further referred as US CB) provides the State
1342 boundaries for the USA. For this work, the 2018 version was retrieved as one shapefile (3.2 MB; available online:
1343 https://www.census.gov/geographies/mapping-files/time-series/geo/carto-boundary-file.html, last accessed:
1344 21.01.2024). More detail on method, data content and access can be found in
1345 http://thematicmapping.org/downloads/.
1346 TM 'country borders' and US CB were used to spatially disaggregate the information of water withdrawal for
1347 domestic, industrial, energy use.
1348

1349 **Multi-Source Weather** (further referred as MSWX) is a high-resolution (3-hourly, 0.1°), bias-corrected
1350 meteorological product with global coverage from 1979 to 7 months into the future. The data for 42 years
1351 (~316700 files in NetCDF format, in total 128.0 GB) were retrieved via www.gloh2o.org/mswx/. For more
1352 detailed information, see Beck et al. (2022).
1353 MSWX 2-meter daily and monthly maximum and minimum air temperature were used to account for the climate-
1354 induced intra- and inter- annual fluctuations of domestic, livestock, and energetic water demand.
1355

1356 **Huang et al. (2018)** is a publication presenting 0.5° resolution global monthly gridded sectoral water withdrawal
1357 dataset for the period 1971–2010.
1358 Huang at al. (2018) Table 3 (calibrated R coefficient values) and Eq. (2) to (6) for temporal downscaling of
1359 domestic and energy water demands were used in this study, respectively.

Appendix 2

1361 Unit conversion to fraction

1362 Hectare (ha): $fraction = {ha \cdot 10^4}/{GridCellArea_{m^2}}$;

1363 Percentage (%): $fraction = {\%}/{100}$;

1364 Class (landcover type): $fraction = 1$, i.e. assumes full 100 % coverage of the grid cell.

Appendix 3

Soil depth
Soil depth layers are derived following Burek et al. (2014) in which the total soil depth is horizontally divided in three layers. The total soil depth is the 'absolute_depth_to_bedrock' from SoilGrids250m, whereas root depths of forest and non-forest are derived from FAO56 and CGLS-LC100 dataset at SoilGrids250m native (~250 m) resolution (see Section 6.2 for more details). The methodology implemented for the creation of three soil layers is the following:

Soil depth layer 1 (surface) SD_1 is assumed constant, equal to 50 mm all over the world for consistency with satellite-derived datasets (satellite signal penetration depth of 50 mm is a good approximation to take into account different meteorological conditions at different hour of the day globally based on Lv et al. (2018)), and follow Eq. (A1):

$$SD_1 = 50mm \tag{A1}$$

Soil depth layer 2 (middle) SD_2 depends on the absolute depth to bedrock adb – if it is equal or less than 300 mm computation follow Eq. (A2), otherwise it is conditional of the root depths as per Eq. (A3), and must meet requirement from Eq. (A4):

$$SD_2 = (adb - SD_1)/2, \, adb \leq 300mm \tag{A2}$$
$$SD_2 = \min(root\_depth, (adb - 300mm - SD_1)), \, adb > 300m \tag{A3}$$
$$SD_2 = 50mm, \, SD2 < 50mm \tag{A4}$$

Soil depth layer 3 (bottom) SD_3, is computed following Eq. (A5):

$$SD3 = adb - (SD_1 + SD_2) \tag{A5}$$

This set of equations is used twice, once with the root depth of forest area and a second time with the root depth of non-forested areas, resulting in a total of six soil depth layers computed at SoilGrids250m native resolution.

Soil hydraulic parameters
Soil hydraulic parameters are derived by following three main steps (see Figure A1).

First, soil hydraulic properties are derived at native resolution by applying pedotransfer functions (PTFs) to each SoilGrids250m soil characteristics layer at each available depth. Pedotransfer functions translate field measured soil information (such as soil texture, pH and structure) into proprieties and parameters needed to describe soil processes. The PTFs implemented here are the ones proposed by Toth et al. (2015). Users can decide to derive soil proprieties from different PTFs, but the general principle presented here remains valid.

Second, the soil hydraulic parameters calculated at SoilGrids250m depths are vertically downscaled to the model soil depth (previously computed) by weighted average (Figure A1, Step 2 with theta saturated as an example) at the native SoilGrids250m resolution (~250 m).

Third, the soil hydraulic parameters at the final soil depths are upscaled from native to final resolution by average using forest and non-forest fraction layers as weights (Figure A1, Step 3).
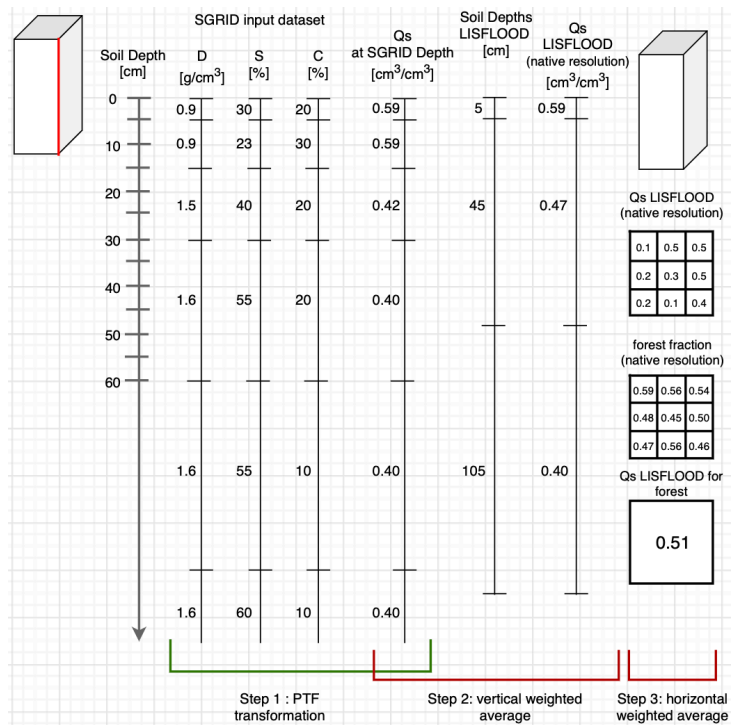
Figure A1. Creation of theta saturated parameter 'Qs' using SoilGrids250m dataset 'SoilGRID' and forest fraction.

Appendix 4

Here more regional examples of the most interesting surface fields of CEMS_SurfaceFields_2022 are provided to show what level of details is available at each resolution and field, and to emphasise consistency through all the fields that is the most valuable requirement when running any type of surface model.
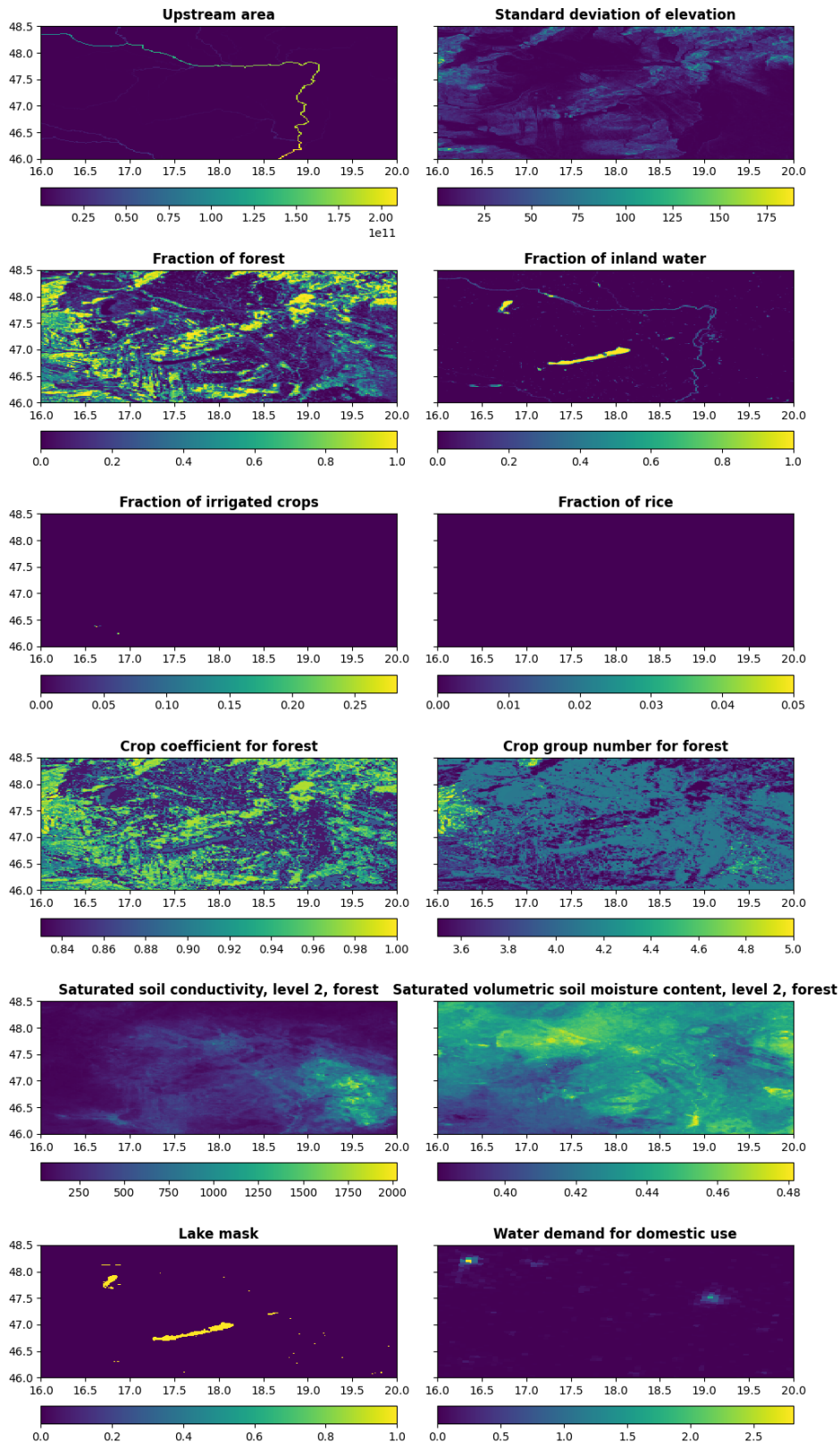
1417
1418
1419
1420
1421
1422
Figure A2. Upstream drainage area in square meters, standard deviation of elevation in meters, fraction of forest, fraction of inland water, fraction of irrigated crops, fraction of rice, crop coefficient for forest, crop group number for forest, saturated soil hydraulic conductivity for forested areas of soil depth layer 2 in mm per day, saturated volumetric soil moisture (i.e. water) content for forested areas of soil depth layer 2, lake mask, and water demand for domestic use at 1 ~~arc min~~arcminute (~1.9 km at the equator) resolution for Danube River area in Europe.
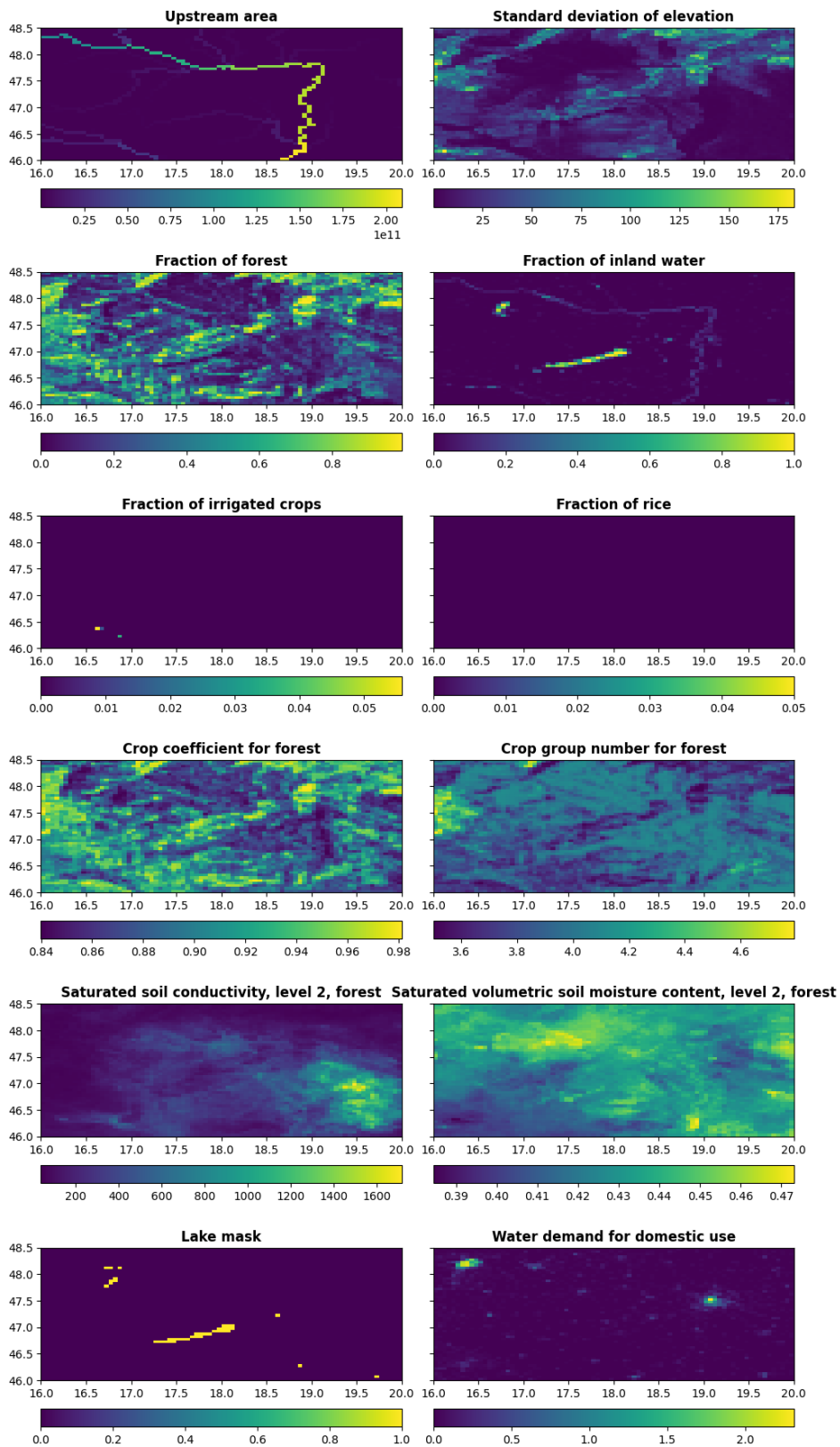
1423
1424 **Figure A3. Same as Figure A2, but at 3 ~~are min~~arcminute (~5.6 km at the equator) resolution for Danube River area**
1425 **in Europe.**
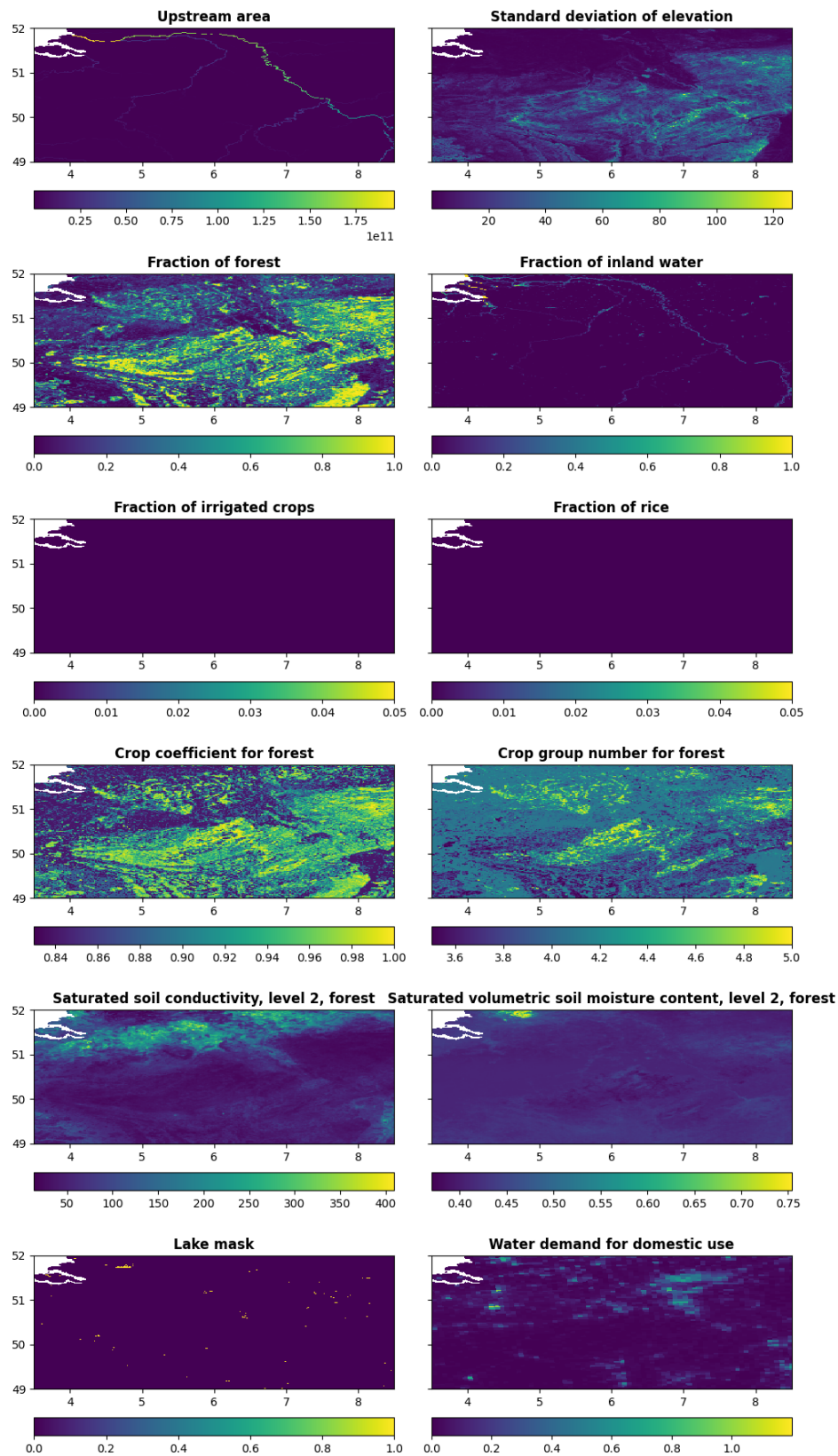
1426
1427 **Figure A4. Same as Figure A2, but at 1 ~~are min~~arcminute (~1.9 km at the equator) resolution for Rhine River area in**
1428 **Germany.**
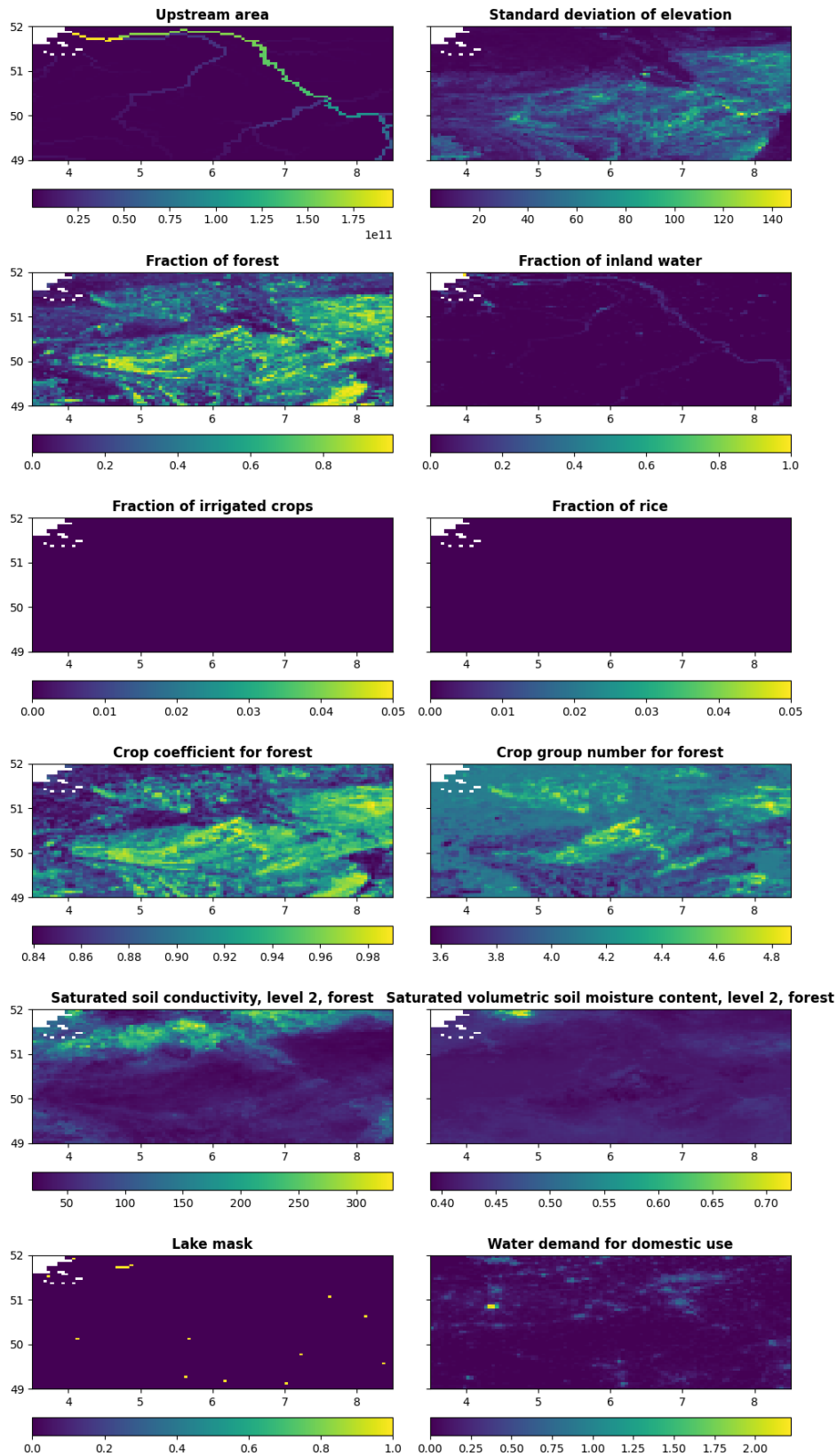
1429
1430 **Figure A5. Same as Figure A2, but at 3 ~~are min~~arcminute (~5.6 km at the equator) resolution for Rhine River area in**
1431 **Germany.**
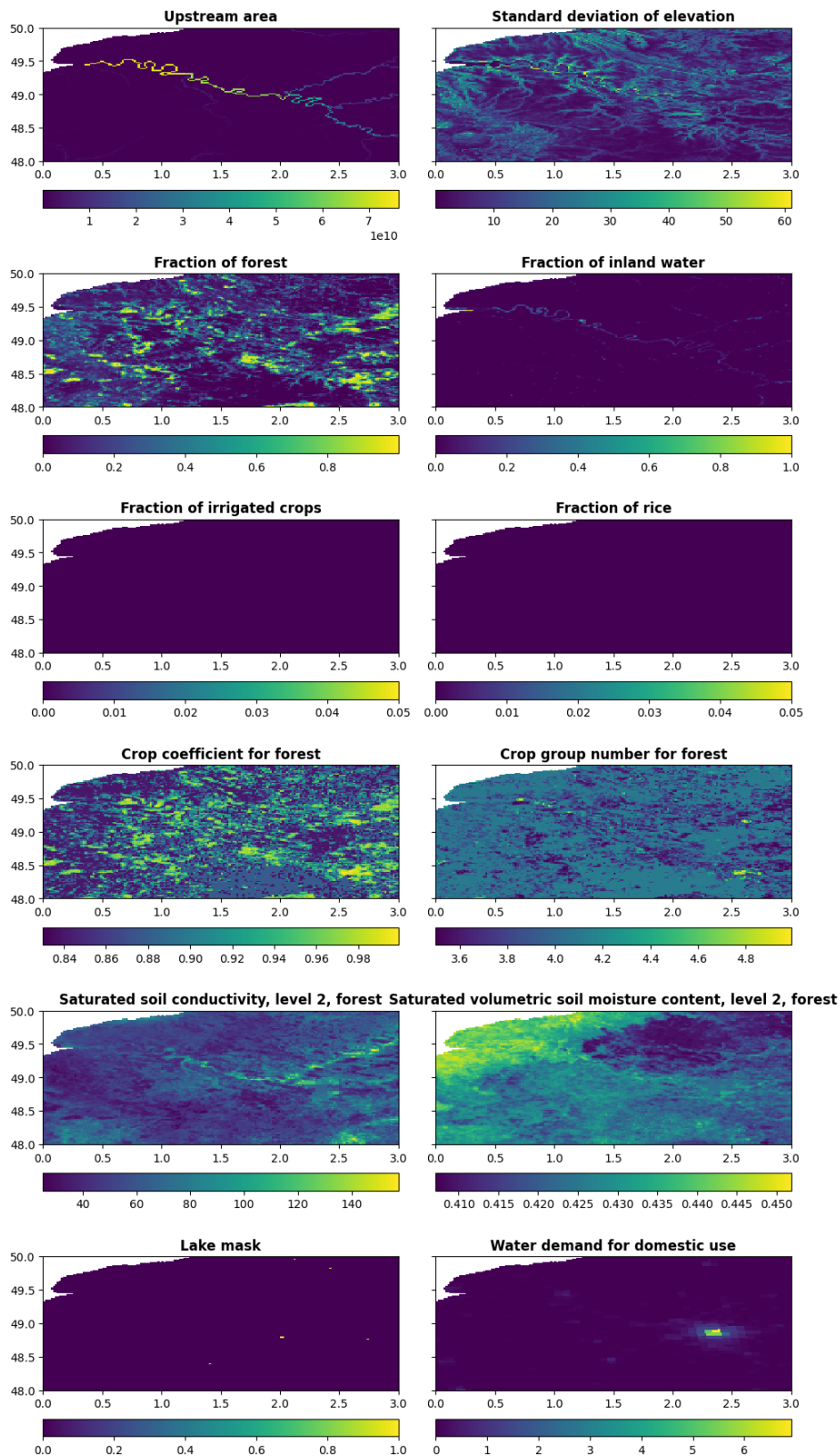
1432
1433
1434

Figure A6. Same as Figure A2, but at 1 ~~arc min~~arcminute (~1.9 km at the equator) resolution for Seine River area in France.
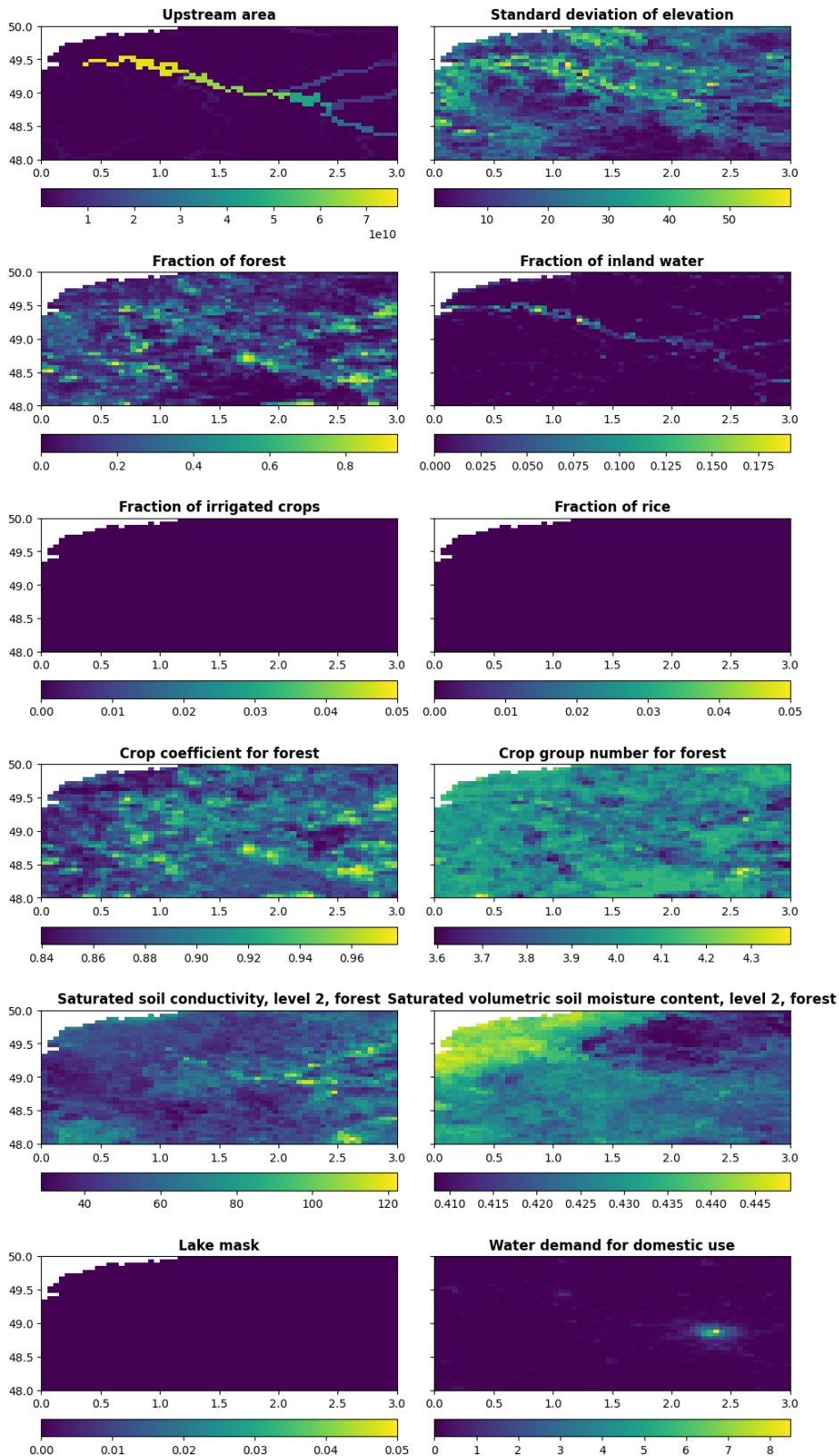
Figure A7. Same as Figure A2, but at 3 ~~are min~~arcminute (~5.6 km at the equator) resolution for Seine River area in France.
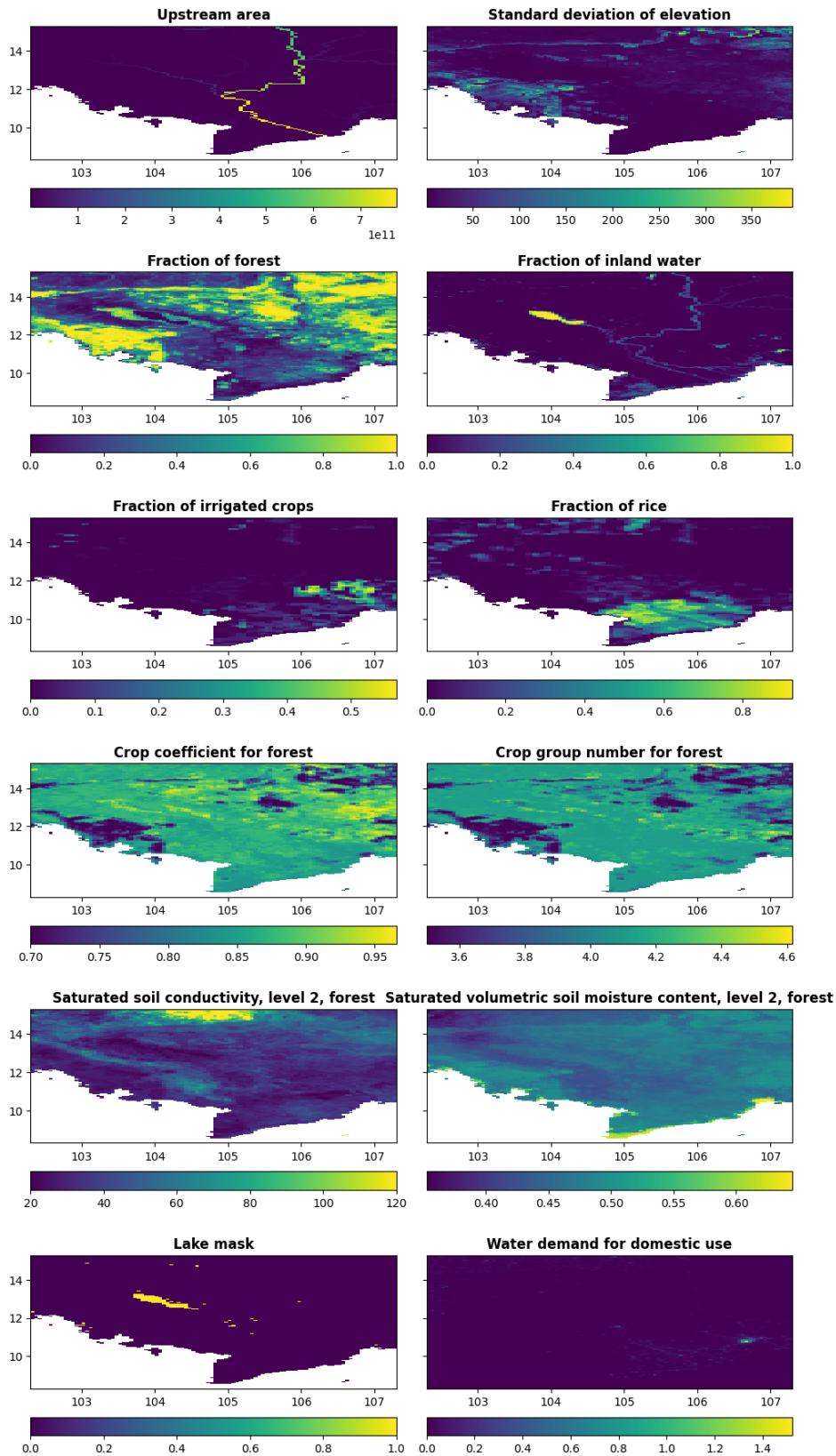
Figure A8. Same as Figure A2, but at 3 ~~are min~~arcminute **(~5.6 km at the equator) resolution for Seine Mekong area in Cambodia.**